

DEPARTMENT OF PHYSICS AND ASTRONOMY

HEIDELBERG UNIVERSITY

Master's Thesis in Physics
submitted by

DION HÄFNER

born in Worms (Germany)

2016

Dion Häfner: *Frictional Control of Cross-Equatorial Flow*

This Master's Thesis has been carried out at

NIELS BOHR INSTITUTE, COPENHAGEN

under the supervision of

PROF. DR. KURT ROTH

(Institute of Environmental Physics, Heidelberg)

and

PROF. DR. MARKUS JOCHUM

(Niels Bohr Institute, Copenhagen)



“ If I have seen further, it is by standing on the shoulders of giants. ”

—Isaac Newton

ACKNOWLEDGMENTS

I strongly believe that we can only succeed through collaboration, be it in science, or in life. Thus, I am deeply grateful to anyone who has helped me on my path so far. This includes anyone who has proofread this document, offered advice, inspired, or instructed me.

I thank *Kurt Roth* for his courage to supervise me abroad, without expecting anything in return. Likewise, I thank *Markus Jochum* for welcoming me as a Master’s student without ever having met me before (and without me knowing much about Physical Oceanography). I thank the free software movement (and, really, anyone who puts their code on GitHub) for providing scientists, artists, students, or just hobbyists with powerful tools without expecting any compensation. I even thank anyone who answers random strangers’ questions on the Internet. Because knowledge, like happiness, is only real when shared.

Likewise, if you have questions regarding this document, the codes I used, or just want to chat — I’m happy to share: mail@dionhaefner.de.

ABSTRACT — ENGLISH

1. Henceforth referred to as “viscosity”.
- The purpose of this study is to examine the dependence of cross-equatorial flow in the ocean on lateral diffusivity¹ in low-resolution climate simulations, with a particular focus on the Meridional Overturning Circulation (MOC). Since frictional effects are critical for the transformation of potential vorticity to enable cross-equatorial flow, a dependence of the overturning on the chosen parameterization of lateral friction seems natural. In low-resolution climate models, viscosity is mostly meant to model unresolved turbulent motion, i. e., it is dominated by an effective eddy diffusivity that is hard to quantify. Furthermore, viscosities are often chosen to be unphysically high in order to achieve a smoother solution. Thus, this thesis investigates to what extent the particular (and quite arbitrary) choice of viscosity influences the meridional overturning, which is decisive for the World Climate².
2. And e. g. the reason for the comparably mild European winters.

This is done by evaluating a number of experiments using the Community Earth System Model (CESM) with varying viscosity and horizontal grid resolutions between 1° and 3° . It is found that even extreme viscosity reductions by several orders of magnitude in an equatorial band reduce the overturning by only $\lesssim 10\%$, or $1.5 \times 10^6 \text{ m}^3 \text{ s}^{-1}$. Localized evaluations are done for the equatorial regions in the Atlantic and western Pacific oceans. In the Atlantic, zonal jets appear on both sides of the equator, creating intense re-circulation regions, while in the Pacific, the amount of viscosity critically determines the composition of the Indonesian Throughflow (ITF) — for very low viscosities, about half of the total ITF transport originates in the southern hemisphere, as opposed to a mostly northern source for the default viscosity. This behavior sheds a critical light on the “Island Rule”, which is often used to calculate the ITF transport based on wind stress alone, and which is independent of viscosity.

A theoretical study using a custom shallow-water model reveals that viscosity does *not* influence cross-equatorial flow to a leading order, contrary to intuition. In contrast, when western boundary layers are under-resolved, an *increased* overturning is found. Further work needs to be done in order to model the observed higher-order response of the ocean to viscosity changes.

ABSTRACT — DEUTSCH

Die vorliegende Arbeit untersucht den Einfluss der Parametrisierung von lateraler Diffusivität³ in niedrig aufgelösten Klimasimulationen auf Meeresströmungen über den Äquator. Ein besonderer Fokus liegt dabei auf der globalen thermohalinen Zirkulation. Da dissipative Effekte unbedingt erforderlich sind um überschüssige potentielle Vortizität zu entfernen und somit Fluss über den Äquator zu ermöglichen, scheint ein Einfluss der gewählten Reibungsparametrisierung auf die globale Zirkulation naheliegend. Die Hauptaufgabe von Viskosität in niedrig aufgelösten Klimamodellen ist die Modellierung von nicht explizit aufgelöster Turbulenz, wodurch sie schwierig zu quantifizieren ist. Darüber hinaus werden Viskositäten oft unrealistisch hoch gewählt, um eine zusätzliche Glättung der numerischen Lösung zu erreichen. Vor diesem Hintergrund untersucht diese Arbeit, zu welchem Grad die eher willkürliche Wahl der Viskosität die globale Zirkulation beeinflusst, die einen kritischen Einfluss auf das Weltklima hat.

Zu diesem Zweck werden einige Community Earth System Model (CESM) Experimente mit variierender Viskosität und Gitterauflösungen zwischen 1° und 3° ausgewertet. Es ergibt sich, dass selbst extreme Reduktionen der äquatorialen Viskosität um mehrere Größenordnungen nur zu einem um etwa 10 % oder $1.5 \times 10^6 \text{ m}^3 \text{ s}^{-1}$ verminderten Fluss über den Äquator führen. Lokale Untersuchungen der äquatorialen Regionen im Atlantik und Westpazifik ergeben, dass sich im Atlantik zonale Jets (und damit eine deutliche Rezirkulation) auf beiden Seiten des Äquators bilden, während im Pazifik Viskositätsänderungen einen starken Effekt auf die Zusammensetzung des Indonesischen Durchflusses (ITF) zeigen⁴. Dies wirft ein kritisches Licht auf die “Island Rule”, die häufig benutzt wird um den ITF Transport zu berechnen, und die unabhängig von Viskosität ist.

Eine theoretische Studie mit einem selbsterstellten “Shallow Water”-Modell zeigt, dass Fluss über den Äquator in führender Ordnung *unabhängig* von Viskosität ist, im Gegensatz zur ursprünglichen Intuition. Wenn westliche Grenzschichten im Modell nicht aufgelöst werden, ergibt sich entgegen der Erwartung ein *erhöhter* äquatorialer Fluss. Weiterführende Studien sind von Nötien, um die beobachtete Abhängigkeit höherer Ordnung der simulierten Zirkulation von der äquatorialen Viskosität korrekt zu modellieren.

3. Fortan als “Viskosität” bezeichnet.

4. Für sehr niedrige Viskositäten wird etwa die Hälfte des totalen Durchflusses von Fluss aus der südlichen Hemisphäre gespeist, im Gegensatz zu einem hauptsächlich von Norden stammenden Fluss in Experimenten mit unveränderter Viskosität.

CONTENTS

SETTING THE STAGE

- Prologue 2
- 1 Geophysical Concepts 5
 - 1.1 Fundamental Models 6
 - 1.2 Notable Solutions 17
 - 1.3 Friction and Viscosity 22
 - 1.4 Global Ocean Currents 27
- 2 The Community Earth System Model 33
 - 2.1 Model Grids 33
 - 2.2 Initial Conditions & Forcing 34
 - 2.3 Lateral Friction in CESM 35

FRICTIONAL CONTROL OF CROSS-EQUATORIAL FLOW

- 3 CESM Experiments 41
 - 3.1 Experimental Setup 42
 - 3.2 Analysis 44
 - 3.3 Discussion: Godfrey's Island Rule 58
- 4 Theoretical Analysis 61
 - 4.1 Theory of Cross-Equatorial Flow 61
 - 4.2 An Equatorial Shallow-Water Model 65
- 5 Wrap-up 75
 - 5.1 What Have We Learned? 75
 - 5.2 Open Questions 77

APPENDICES

- A Additional Plots 80
- B An Equatorial Shallow-Water Model (cont.) 82

Bibliography 87

LIST OF FIGURES

- 0.1 Smoke above Indonesia during the 2016 wildfires. 3
- 1.1 Comparison between Sverdrup and barotropic stream functions. 19
- 1.2 Location, scale and magnitude of the Kuroshio. 19
- 1.3 Different boundary conditions may lead to large changes in the circulation. 21
- 1.4 Turbulence in the ocean. 23
- 1.5 The generation of numerical noise in a shallow-water model without lateral friction. 27
- 1.6 The MOC. From Kuhlbrodt et al., 2007, after Rahmstorf, 2002. 28
- 1.7 One of the first illustrations of the MOC. 28
- 1.8 Vertical stream function of the Atlantic Meridional Overturning Circulation (AMOC) in the CESM x3 default run. 29
- 1.9 Currents in the ITF-region. 30
- 2.1 The CESM model grid in comparison to a regular latitude / longitude grid. 33
- 2.2 Bathymetry in the x1 grid. 34
- 2.3 Viscosity parameters A and B in x3_default. 35
- 3.1 Scaling factor of the boundary layer viscosity in the cosine-banded runs. 42
- 3.2 The generation of numerical noise at the equator in low viscosity CESM experiments. 45
- 3.3 Grid-scale Reynolds numbers in the low-viscosity runs. 45
- 3.4 Global barotropic stream functions (BSFs) for the x1 runs. 46
- 3.5 Global BSFs for the x3-runs. 47
- 3.6 Viscosity of x3_hivisc, relative to x3_default. 48
- 3.7 Equator-crossing contours of the vertical AMOC stream function. 49
- 3.8 The zonally smoothed velocity field along two isopycnals in the Atlantic. 50
- 3.9 Depth of two isopycnals in the AMOC. 50
- 3.10 The BSF in the ITF region for some x3-runs. 53
- 3.11 Meridional velocity profile in the ITF for x3_default and x1_default. 54
- 3.13 Geometry of the ITF in CESM. 54
- 3.12 The velocity field along two isopycnals in the ITF. 55
- 3.14 Salinity at 100 m depth in the ITF. 56
- 3.15 Salinity profile in the ITF. 56

| | | |
|------|---|----|
| 3.16 | BSF in the ITF region for the x_1 experiments. | 57 |
| 3.17 | The integration path as used in the Island Rule for New Zealand. | 58 |
| 4.1 | Steady-state solutions of one-dimensional equatorial geostrophic adjustment. | 64 |
| 4.2 | Equatorial regions of the first set of shallow-water simulations. | 68 |
| 4.4 | Hemispheric mass balance for set 1 of the shallow water experiments. | 68 |
| 4.3 | Steady-state solution of the shallow-water model for high resolution and low forcing. | 69 |
| 4.5 | Equatorial regions of the second set of shallow-water simulations. | 70 |
| 4.6 | Hemispheric mass balance for set 2 of the shallow water experiments. | 70 |
| 4.7 | Height field of a low-viscosity shallow-water experiment. | 71 |
| 4.8 | Equatorial flow for shallow water experiment set 3. | 71 |
| 4.9 | Hemispheric mass balance for set 3 of the shallow water experiments. | 72 |
| 5.1 | The ITF model presented in Nof, 1996. | 78 |
| A.1 | Perpendicular viscosity parameter B for all x_3 runs. | 80 |
| A.2 | Perpendicular viscosity parameter B for all x_1 runs. | 81 |
| B.1 | Comparison between a geostrophic adjustment solution from Killworth, 1991, and one created with my own shallow-water model. | 86 |
| B.2 | Comparison between a steady-state solution from Greatbatch and Lu, 2003, and one created with my own shallow-water model. | 86 |

LIST OF TABLES

- 2.1 Viscosity parameters in the parameterization used in CESM and their default values. 37
- 3.1 CESM run overview. 43
- 3.2 Change of Atlantic cross-equatorial transport (in Sverdrup) in CESM experiments compared to their respective default. 48
- 3.3 Cross-equatorial transport in the AMOC. 52
- 3.4 Change of ITF transport in CESM experiments compared to their respective default. 53
- 3.5 Change of ITF transport originating in the northern hemisphere. 53
- 3.6 Meridional ITF transport for each experiment, divided in upper and lower layer. 54
- 3.7 Mean temperature in the ITF, split into upper and lower layer. 56
- B.1 Parameters used in the first verification run. 85

LIST OF CODE LISTINGS

- B.1 Equation setup for the shallow-water model in FiPy. 84

ACRONYMS

| | |
|-------|---|
| PV | Potential Vorticity |
| CESM | Community Earth System Model |
| POP2 | Parallel Ocean Program 2 |
| GCM | General Circulation Model |
| MOC | Meridional Overturning Circulation |
| AMOC | Atlantic Meridional Overturning Circulation |
| ITF | Indonesian Throughflow |
| ENSO | El Niño–Southern Oscillation |
| NADW | North Atlantic Deep Water |
| ACC | Antarctic Circumpolar Current |
| MC | Mindanao Current |
| NECC | North-Equatorial Countercurrent |
| NEC | North-Equatorial Current |
| SEC | South-Equatorial Current |
| NGCUC | New Guinea Coastal Undercurrent |
| BSF | Barotropic Stream Function |
| ODE | Ordinary Differential Equation |
| PDE | Partial Differential Equation |

MATHEMATICAL NOTATION

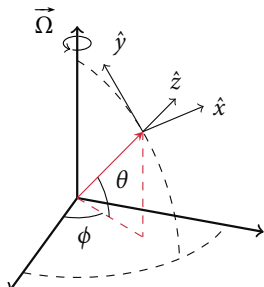
Throughout this document, the following conventions regarding mathematical notation are being assumed, unless stated otherwise:

General

- ▶ Vectorial quantities are marked with an arrow (\vec{u}).
- ▶ A dot \cdot between vectors denotes a scalar product, and a cross \times the vector product.
- ▶ Unit vectors carry a caret (\hat{x}).

Coordinate Systems

- ▶ In Cartesian coordinates, the directions are denoted as



$$\hat{x} = \begin{pmatrix} 1 \\ 0 \\ 0 \end{pmatrix}, \quad \hat{y} = \begin{pmatrix} 0 \\ 1 \\ 0 \end{pmatrix}, \quad \hat{z} = \begin{pmatrix} 0 \\ 0 \\ 1 \end{pmatrix}.$$

Following the convention in Geophysics, x points in zonal direction, y in meridional direction, and z into the vertical direction (skyward). Components of the velocity \vec{u} in x , y , and z -direction are denoted as u , v , and w , respectively.

- ▶ In spherical surface coordinates, the zonal coordinate is denoted as ϕ (longitude), and the meridional coordinate as θ (latitude).

Differentiation

- ▶ The partial derivative of a quantity h is written as

$$\frac{\partial h}{\partial \phi} \equiv h_\phi.$$

- ▶ It is often necessary to calculate the derivative of a quantity *along a streamline*.

This *material derivative* is denoted as

$$\frac{D}{dt} q = \underbrace{q_t}_{\text{partial derivative}} + \overbrace{\vec{u} \cdot \nabla q}^{\text{advection}}.$$

- The Nabla operator ∇ , as usual in vector calculus, is defined as

$$\nabla = \begin{pmatrix} \partial/(\partial x) \\ \partial/(\partial y) \\ \partial/(\partial z) \end{pmatrix}.$$

Hence, ∇f denotes the gradient of the scalar field f , and $\nabla \cdot \vec{u}$ and $\nabla \times \vec{u}$ the divergence and curl of a vector field \vec{u} , respectively.

- The horizontal equivalent of ∇ is denoted as ∇_H and only operates on the x and y -directions of a vector field. The horizontal divergence and curl thus read

$$\begin{aligned} \text{div}_H(\vec{u}) &= \nabla_H \cdot \vec{u} = u_x + v_y \\ \text{curl}_H(\vec{u}) &= \nabla_H \times \vec{u} = v_x - u_y. \end{aligned}$$

- The Jacobian determinant⁵ $J(a, b)$ of two scalar fields a, b is defined as

$$J(a, b) := a_x b_y - a_y b_x.$$

5. For the sake of brevity just referred to as “Jacobian”.

Scale Analysis

- The operator $\mathcal{O}(x)$ is used several times during scale analyses, and simply means “order of” — it maps a physical quantity x to a corresponding typical scale⁶.

Other

- The temporal mean value of a quantity u is denoted as $\langle u \rangle$.

6. These scales are chosen in a heuristic manner, providing motivations rather than formal derivations. While their exact value can be argued, their order of magnitude usually cannot, allowing the comparison of terms that vary by several orders of magnitude.

Part I

SETTING THE STAGE

O

PROLOGUE

“ *The sea, washing the equator and the poles, offers its perilous aid, and the power and empire that follow it [...]. “Beware of me”, it says, “but if you can hold me, I am the key to all the lands”.* ”

—Ralph Waldo Emerson

Cross-equatorial flow has a major influence on the World’s climate. It effectively couples both the northern and southern hemisphere in latitude, but also the Atlantic, Pacific and Indian Oceans in longitude, exchanging heat and matter between regions that lie thousands of kilometers apart. Equatorial processes like the El Niño–Southern Oscillation (ENSO) influence countless human lives, e. g. through the extreme weather events observed during *El Niño* (Fig. 0.1). Another example is the Atlantic Meridional Overturning Circulation (AMOC) and the resulting Gulf Stream, which is the reason for the mild European climate compared to that of e. g. the East Coast of North America.

However, despite its crucial role in understanding our climate, cross-equatorial flow is still not very well researched. The absence of a Coriolis parameter at 0° latitude makes it impossible to apply geostrophic balance or other leading-order approximations, so the dynamics in the equatorial region are determined by processes that are hard to quantify like nonlinearity and friction (Pedlosky, 1996; Edwards and Pedlosky, 1998).

While many studies focus on either the driving processes of the Meridional Overturning Circulation (MOC) and thus the forcing of cross-equatorial flow (Kuhlbrodt et al., 2007; Marshall and Speer, 2012), or the mechanics of cross-equatorial flow with a fixed inter-hemispheric forcing (such as Edwards and Pedlosky, 1998; Kawase, 1987), the kinematic processes involved in *enabling* cross-equatorial flow are less well studied. Due to the success of simple models such as the Stommel box model (Stommel, 1961) or the Stommel-Arons model (Stommel and Arons, 1960), a cross-hemispheric pressure gradient is often implicitly assumed to result in a cross-equatorial flow, without paying attention to the actual dynamics at the equator.

1. For more information on the Killworth model refer to § 4.1.2.

An interesting study is found in Killworth, 1991, which examines cross-equatorial geostrophic adjustment, i. e., an unforced spin-up after a mass imbalance between the hemispheres has been released¹. Using his equatorial shallow-water model, Killworth proceeds to show that in an inviscid, one-dimensional ocean, water may at most penetrate about two Rossby radii of deformation into the opposite hemisphere. After extending his model to a two-dimensional basin and introducing lateral friction, Killworth found that transport to high latitudes of the opposite hemisphere is now possible, enabled by friction that acts to dissipate excessive *potential vorticity* (PV) (§ 1.1.1). At the same time,

Killworth found a lower interior transport across the equator when lowering the lateral diffusivity (here referred to as viscosity).

Since the Earth's ecosystem offers a sheer infinite level of complexity, there is only so much insight one may gain from observations and analytical solutions. One immensely valuable tool in understanding our climate are General Circulation Models (GCMs), which are becoming more powerful each day as research in modeling and computational sciences progresses. However, despite their usefulness, error margins are often large due to uncertainties in initial conditions (from observations), parameters, parameterizations, or even the physical processes itself.

Some of these uncertainties are caused by the parameterization of friction in climate models, which is usually not based on first principles but, on the contrary, treated rather heuristically². Often, unrealistically high viscosities are assumed in order to suppress numerical noise (§ 1.3.4), since diffusive friction leads to smoother numerical solutions. However, lowering viscosity and accepting some noise in the solution may in fact lead to physically more relevant solutions, as shown in e. g. Jochum et al., 2008.

2. Cf. § 1.3.

That being said, the question I set out to answer in this thesis can be formulated as:

How sensitive is the meridional overturning in low-resolution simulations towards changes in lateral diffusivity, and thus the magnitude of friction that is acting at the equator?

In particular, since it is known that friction is crucial in enabling cross-equatorial flow through the transformation of potential vorticity (§ 4.1), to what extent is it possible to control the magnitude of the overturning through viscosity modifications in Community Earth System Model (CESM), a state-of-the-art climate model, and what is suggested by theory?



Figure 0.1: Smoke above Indonesia, released during the 2016 wildfires, which are amplified by El Niño. Satellite image by NASA.

CONTENTS

| | | |
|-------|--|----|
| 1 | Geophysical Concepts | 5 |
| 1.1 | Fundamental Models | 6 |
| 1.1.1 | General Circulations | 6 |
| 1.1.2 | Leading-Order Equations | 10 |
| 1.1.3 | Layered Model | 14 |
| 1.2 | Notable Solutions | 17 |
| 1.2.1 | Sverdrup Theory | 17 |
| 1.2.2 | Western Boundary Currents | 19 |
| 1.3 | Friction and Viscosity | 22 |
| 1.3.1 | Turbulent Diffusion | 22 |
| 1.3.2 | Bottom Friction | 24 |
| 1.3.3 | Stability Conditions | 25 |
| 1.3.4 | Numerical Noise | 26 |
| 1.4 | Global Ocean Currents | 27 |
| 1.4.1 | The Meridional Overturning Circulation (MOC) | 28 |
| 1.4.2 | Local Features | 29 |

GEOPHYSICAL CONCEPTS

1

This chapter summarizes some of the physical concepts and mechanisms required to understand the later chapters of my thesis. It touches upon basic geophysical fluid dynamics and describes some of the relevant ocean currents, and is meant as an introduction to Physical Oceanography in general.

In § 1.1, a set of fundamental equations describing the large-scale flow in the ocean is derived (momentum, continuity, and vorticity equations). Following up, these equations are simplified by making some common assumptions about the dominant processes in the ocean, in order to gain an intuition about the most important mechanisms controlling the ocean circulation, and to establish a solid foundation for later chapters.

§ 1.2 presents the Sverdrup and Munk solutions to the equations derived before, to showcase how even simple assumptions may lead to powerful descriptions of the ocean, with a wide range of applicability.

§ 1.3 summarizes the role and parameterization of friction in ocean models, introducing the two most common formulations of friction in modeling (diffusive and bottom friction), and reviewing some numerical aspects of a diffusive term (stability and numerical noise).

§ 1.4 contains an introduction to some relevant currents and circulation systems in the real ocean (the global overturning, the Atlantic Meridional Overturning Circulation, and the Indonesian Throughflow).

Most considerations in this chapter follow two great textbooks by J. Pedlosky: *Ocean Circulation Theory* (Pedlosky, 1996) and *Geophysical Fluid Dynamics* (Pedlosky, 1992).

1.1 FUNDAMENTAL MODELS



Sir George Stokes (1819–1903). Public Domain.

Many different ocean models exist, from highly idealized, qualitative ones, to General Circulation Models (GCMs) or even coupled Earth System Models with nearly arbitrary complexity. It is neither possible nor feasible to consider every existing dynamics of the ocean during this study. The following sections present three different, common views of the ocean of varying complexity: A general model in three dimensions (§ 1.1.1), a model retaining only leading-order processes (§ 1.1.2), and a simple layered model (§ 1.1.3).

Each of these models is represented by a characteristic set of equations (continuity, momentum, and vorticity equations), and each of these models is useful to gain an intuition of certain sub-processes in the ocean, which will prove to be helpful in later chapters.

1.1.1 General Circulations

This section presents a model that describes a “general” large-scale circulation, making as few assumptions as necessary (and I am trying to avoid making implicit assumptions in the process).

Momentum Equations

1. This has in fact been deemed a “Millennium Problem” by the *Clay Mathematics Institute*, worth a \$1 000 000 cash prize.

2. See front matter for information on mathematical notation.

NAVIER-STOKES EQUATIONS

$$\underbrace{\frac{\partial}{\partial t} \vec{u}}_{\text{material derivative}} + \underbrace{(\vec{u} \cdot \nabla) \vec{u}}_{\text{advection}} - \underbrace{\vec{\mathcal{F}}}_{\text{dissipation}} = \underbrace{-\frac{1}{\rho} \nabla p}_{\text{internal forces}} + \underbrace{\vec{g}}_{\text{external forces}} \quad (1.1)$$

with

- ▶ fluid density ρ ;
- ▶ velocity components \vec{u} ;
- ▶ frictional forces $\vec{\mathcal{F}}$, often modeled as $\mu \nabla^2 \vec{u}$ (lateral friction) or $-\kappa \vec{u}$ (bottom friction)³;

3. More on dissipative terms in § 1.3.

- ▶ pressure p ; and
- ▶ body accelerations \vec{g} .

However, this form of the Navier-Stokes equations is too general to be of practical use in Oceanography. \vec{g} is actually well-known, since the only relevant body forces in the ocean are gravity and the Coriolis force, hence:

$$\vec{g} = -2\vec{\Omega} \times \vec{u} - g\hat{z} = \begin{pmatrix} -2\omega(v \sin \theta - w \cos \theta) \\ 2\omega u \sin \theta \\ -2\omega u \cos \theta - g \end{pmatrix} \quad (1.2)$$

with

$$\begin{aligned} \vec{\Omega} &= \omega(\cos \theta \hat{y} + \sin \theta \hat{z}) && \text{(Earth's angular velocity)} \\ \omega &= \frac{2\pi}{24 \text{ h}} = 7.27 \times 10^{-5} \text{ s}^{-1} && \text{(Earth's rate of rotation)} \\ f &= 2\omega \sin \theta && \text{(Coriolis parameter)} \\ g &= 9.81 \text{ m/s}^2 && \text{(Gravitational acceleration)} \end{aligned}$$

Plugging (1.2) into (1.1) then yields:

$$\vec{u}_t + (\vec{u} \cdot \nabla) \vec{u} + 2\vec{\Omega} \times \vec{u} + g\hat{z} = -\frac{1}{\rho} \nabla p + \vec{F} \quad (1.3)$$

MOMENTUM EQUATIONS
in vector form

Continuity Equation

The most fundamental constraint in fluid dynamics that needs to be fulfilled unconditionally by all successful models is mass conservation. It is usually expressed through a continuity equation, describing the evolution of the fluid density ρ in the flow field:

$$\underbrace{\rho_t}_{\text{transient}} + \underbrace{\nabla \cdot (\rho \vec{u})}_{\text{convection}} = \underbrace{\rho_t + \vec{u} \cdot \nabla \rho}_{\text{advection}} + \underbrace{\rho \nabla \cdot \vec{u}}_{\text{divergence}} + \underbrace{S(\vec{x}, t)}_{\text{sources}} \quad (1.4)$$

CONTINUITY EQUATION
in general form

In large parts of the ocean, the components adding up to the velocity divergence (i.e., u_x, v_y, w_z) will be much larger than any explicit source or the advection of density. In this case, (1.4) can be decomposed, and each contribution can be

4. See *Atmospheric and Oceanic Fluid Dynamics* (Vallis, 2006) for a discussion on the validity of this assumption.

required to hold separately:⁴

$$\nabla \cdot \vec{u} = u_x + v_y + w_z = 0 \quad (1.5)$$

and

$$\frac{D}{dt}\rho = S(\vec{x}, t)$$

5. See *Waves in the Ocean and Atmosphere* (Pedlosky, 2013), where Pedlosky derives that gravity waves are divergence-free for phase speeds that are small compared to the speed of sound.

The first statement is often cited as a condition for an *incompressible fluid*, and holds to a very high degree in the ocean⁵. The second condition describes the evolution of density due to explicit sources, i. e., diapycnal (“cross-isopycnal”) mixing. In an adiabatic ocean,

$$\frac{D}{dt}\rho = S \equiv 0, \quad (1.6)$$

which is a good approximation in the deep ocean.

Vorticity Equation

Although vorticity is a critical quantity for the large-scale movement of the oceans, it is hard to deal with intuitively, since rotating flows usually do not occur in everyday life. Thus, the most important concepts regarding vorticity (and its conservation) shall be introduced here.

6. And is thus a measure for the shear of the flow, and an indicator for its rate of rotation.

The *relative vorticity* $\vec{\omega}$ is generally defined as the curl of the velocity field:⁶

$$\vec{\omega} = \nabla \times \vec{u}$$

The evolution of vorticity in a system is described by the *vorticity equation*. It can be derived from the 3-dimensional momentum equations in vectorial form, (1.3). Replacing the advection term $(\vec{u} \cdot \nabla) \vec{u}$ in (1.3) by⁷

$$(\vec{u} \cdot \nabla) \vec{u} = \vec{\omega} \times \vec{u} + \nabla \left(\frac{|\vec{u}|^2}{2} \right)$$

yields

$$\vec{u}_t + \frac{1}{2} \nabla(|\vec{u}|^2) + (\vec{\omega} + 2\vec{\Omega}) \times \vec{u} + g\hat{z} = -\frac{1}{\rho} \nabla p + \vec{\mathcal{F}}. \quad (1.7)$$

Applying the curl operator to (1.7), and using that $\nabla \times \nabla \phi = 0$ for any scalar field ϕ , leads to

$$\vec{\omega}_t + \nabla \times (\vec{\omega}_a \times \vec{u}) = \frac{\nabla \rho \times \nabla p}{\rho^2} + \nabla \times \vec{\mathcal{F}}$$

with $\vec{\omega}_a = \vec{\omega} + 2\vec{\Omega}$, a quantity called *absolute vorticity*.

This first formulation of the vorticity equation can be simplified further by applying the vector identity

$$\nabla \times (\vec{\omega}_a \times \vec{u}) = \vec{\omega}_a \nabla \cdot \vec{u} + (\vec{u} \cdot \nabla) \vec{\omega}_a - \underbrace{\vec{u} \nabla \cdot \vec{\omega}_a}_{=0} - (\vec{\omega}_a \cdot \nabla) \vec{u}$$

yielding

$$\underbrace{\frac{D}{Dt} \vec{\omega}_a}_{(i)} = \underbrace{(\vec{\omega}_a \cdot \nabla) \vec{u}}_{(ii)} - \underbrace{\vec{\omega}_a \nabla \cdot \vec{u}}_{(iii)} + \underbrace{\frac{\nabla \rho \times \nabla p}{\rho^2}}_{(iv)} + \underbrace{\nabla \times \vec{F}}_{(v)}. \quad (1.8)$$

VORTICITY EQUATION
in general form

The absolute vorticity $\vec{\omega}_a$ of the flow is thus altered through:

- i) advection along a streamline;
- ii) twisting / tilting due to velocity shear;
- iii) convergence / divergence of the flow (sources / sinks);
- iv) baroclinic flow; and
- v) curl of frictional forces.

Potential Vorticity

The vorticity equation had not been as central as it is in Oceanography without one very important property: the conservation of potential vorticity (PV). In order to re-formulate (1.8) as a conservation law, the continuity equation (1.4) in the form⁸

$$\nabla \cdot \vec{u} = -\frac{1}{\rho} \frac{D\rho}{Dt}$$

8. Assuming the absence of explicit sources, but not necessarily incompressibility.

is used to eliminate the divergence of the flow from the vorticity equation:

$$\frac{D}{Dt} \left(\frac{\vec{\omega}_a}{\rho} \right) = \left(\frac{\vec{\omega}_a}{\rho} \cdot \nabla \right) \vec{u} + \frac{\nabla \rho \times \nabla p}{\rho^3} + \frac{1}{\rho} \nabla \times \vec{F} \quad (1.9)$$

Multiplying (1.9) with a scalar fluid property λ that fulfills the condition

$$\frac{D\lambda}{Dt} = \Lambda$$

9. See *Geophysical Fluid Dynamics* (Pedlosky, 1992).

with some unspecified source Λ , ultimately leads to⁹

$$\frac{D}{dt} \Pi = \underbrace{\frac{\vec{\omega}_a \cdot \nabla \Lambda}{\rho}}_{\text{sources (i)}} + \underbrace{\nabla \lambda \cdot \left(\frac{\nabla p \times \nabla \rho}{\rho^3} \right)}_{\text{baroclinity (ii)}} + \underbrace{\frac{\nabla \lambda}{\rho} \cdot (\nabla \times \vec{\mathcal{F}})}_{\text{friction (iii)}} \quad (1.10)$$

where Π is called *potential vorticity*:

POTENTIAL VORTICITY
in general form

$$\Pi = \frac{\vec{\omega}_a \cdot \nabla \lambda}{\rho}$$

Equation 1.10 thus implies that potential vorticity is a *conserved quantity* if the following conditions are fulfilled:

- i) λ is conserved along streamlines, i. e., $\Lambda = 0$;
- ii) frictional forcing is negligible ($\vec{\mathcal{F}} \approx 0$); and
- iii) the flow is purely barotropic, i. e., $\nabla p \times \nabla \rho = 0$; or $\lambda \equiv \lambda(p, \rho)$, i. e., λ is a function of pressure and density alone.¹⁰

10. $\nabla \lambda(p, \rho) = \lambda_p \nabla p + \lambda_\rho \nabla \rho$,
 $\rightarrow \nabla \lambda \cdot (\nabla p \times \nabla \rho) = 0$, a fundamental property of the box product.

One possible, natural choice for λ in the ocean is density, i. e., $\lambda \equiv \rho$. The first condition is then valid for purely adiabatic flow by definition (1.6), and the third condition is fulfilled unconditionally (since λ then trivially depends on ρ only). Hence, $\Pi_{\lambda=\rho} = \vec{\omega}_a / \rho \cdot \nabla \rho$ is conserved in the absence of friction and diapycnal mixing.



The conservation of potential vorticity is one of the most powerful constraints in all of Oceanography. Since frictional forces and diabatic processes are typically negligible in the interior ocean, a solution for the large-scale interior circulation can directly be inferred from the vorticity equation (the Sverdrup solution, cf. § 1.2.1).

1.1.2 Leading-Order Equations

While § 1.1.1 introduces a set of equations that describe nearly every possible ocean dynamics, it is often useful to approximate the general equations using some reasonable assumptions in order to reduce the complexity of the system. This is in fact one of the most common approaches in Oceanography: Since, on one hand, the general equations of motion (momentum equations plus continuity equation) are mathematically very difficult to treat¹¹, and, on the

11. Four three-dimensional, non-linear, coupled partial differential equations, thus allowing for chaotic behavior in the form of turbulence.

other hand, the observed behavior of the ocean is pretty simple in most regions (mostly linear, two-dimensional flow), there is an inherent need for finding sensible approximations.

In this section, some approximations that are suitable in a large portion of the ocean are applied to retain a simpler set of equations — namely:

- ▶ the small aspect ratio of the ocean, suppressing vertical terms;
- ▶ the Boussinesq Approximation;
- ▶ hydrostatic balance; and
- ▶ geostrophic balance as leading-order dynamics.

Momentum & Continuity Equations

For large-scale circulations in the open ocean, horizontal length scales L are typically much larger than the vertical length scale D . Reasonable scales for the Atlantic Ocean would be $L = 5000$ km and $D = 5$ km, giving an aspect ratio δ of about $\delta = \frac{D}{L} \approx 10^{-3} \ll 1$. This leads to the assumption that

$$\mathcal{O}(w) = \frac{D}{T} \ll \mathcal{O}(u) = \frac{L}{T}$$

with a typical time scale T . An approximate form of the body forcing \vec{g} in the Navier-Stokes equations (1.1) is thus¹²:

$$\vec{g} = \begin{pmatrix} -f(v - w \cot \theta) \\ fu \\ -fu \cot \theta - g \end{pmatrix} \approx \begin{pmatrix} -fv \\ fu \\ -g \end{pmatrix} \quad (1.11)$$

Plugging (1.11) into (1.1) then yields

$$\begin{aligned} u_t + uu_x + vu_y + wu_z - fv &= -\frac{p_x}{\rho} + \hat{x} \cdot \vec{\mathcal{F}} \\ v_t + uv_x + vv_y + wv_z + fu &= -\frac{p_y}{\rho} + \hat{y} \cdot \vec{\mathcal{F}} \\ w_t + uw_x + vw_y + ww_z + g &= -\frac{p_z}{\rho} + \hat{z} \cdot \vec{\mathcal{F}}. \end{aligned}$$

A sensible decomposition of p and ρ into a static background value and one influenced by the flow field ($\rho_0(z)$ and $\rho'(x, y, z)$, respectively) leads to the insight that the leading-order balance in the horizontal momentum equations

¹². Also assuming that $\mathcal{O}(2\omega u \cos \theta) = 1.5 \times 10^{-4} \text{ s}^{-1} u \ll g$.

¹³. This is shown e. g. in *Geophysical Fluid Dynamics* (Pedlosky, 1992).

must be¹³

$$\begin{aligned} fv &= \frac{1}{\rho_0} p'_x \\ fu &= -\frac{1}{\rho_0} p'_y \end{aligned} \quad (1.12)$$

which is called *geostrophic balance* (whereas replacing ρ with ρ_0 is called the *Boussinesq Approximation*). Using the same argument, the w -equation becomes to a good approximation

$$p_z = -\rho g, \quad (1.13)$$

which is the *hydrostatic balance*.

Plugging (1.12) into the continuity equation for incompressible flow (1.5) yields

$$\begin{aligned} 0 &= \nabla \cdot \vec{u} = -\left(\frac{p'_y}{f\rho_0}\right)_x + \left(\frac{p'_x}{f\rho_0}\right)_y + w_z = \\ &= -\frac{p'_{xy}}{f\rho_0} + \frac{p'_{xy}}{f\rho_0} - \frac{p'_x f_y}{f^2 \rho_0} + w_z. \end{aligned}$$

Since

$$\mathcal{O}\left(\frac{p'_{xy}}{f\rho_0}\right) = \frac{U}{L} \quad \text{and} \quad \mathcal{O}\left(\frac{p'_x f_y}{f^2 \rho_0}\right) = \frac{U}{R_E},$$

¹⁴. A similar result can be obtained from the vorticity equation by assuming linear, inviscid, purely barotropic flow — this is known as the Taylor-Proudman Theorem.

the dominant balance in the continuity equation for flow of a scale L for which $L/R_E < 1$ is between the geostrophic terms, which cancel each other. Thus, for flow of scale L , $w_z \approx 0$ to a leading order. As w must vanish at flat boundary surfaces, this implies that¹⁴

$$w \approx 0 \quad (1.14)$$

for geostrophic flow. Hence, the leading-order momentum equations become in this case

$$\begin{aligned} u_t + uu_x + vu_y - fv &= -\frac{p_x}{\rho_0} + \hat{x} \cdot \vec{\mathcal{F}} \\ v_t + uv_x + vv_y + fu &= -\frac{p_y}{\rho_0} + \hat{y} \cdot \vec{\mathcal{F}} \\ -\rho g &= p_z. \end{aligned} \quad (1.15)$$

Stream functions

According to the fundamental theorem of vector calculus, every (mathematically sane) vector field can be decomposed into two parts, one irrotational (curl-free) and one solenoidal (divergence-free). In three dimensions, the Helmholtz decomposition of the (vector) flow field \vec{u} is given by

$$\vec{u} = -\nabla\Phi + \nabla \times \vec{\Psi}$$

with a scalar potential Φ and a vector potential $\vec{\Psi}$. In the two-dimensional case (Helmholtz-Hodge decomposition¹⁵), both of these parts are expressed through a scalar function: the velocity potential Φ (irrotational) and the stream function Ψ (solenoidal), such that

$$\begin{pmatrix} u \\ v \end{pmatrix} = \nabla\Phi + J\nabla\Psi$$

with

$$J = \begin{pmatrix} 0 & -1 \\ 1 & 0 \end{pmatrix},$$

an operator rotating a 2-dimensional vector counterclockwise by $\pi/2$. Since the leading-order flow is purely horizontal and divergence-free (cf. (1.14)), implying $\Phi \approx 0$, it can be described by a stream function Ψ only, with

$$Hu = -\Psi_y, \quad Hv = \Psi_x.$$

Here, H denotes the total height of the water column, which was added to make sure that Ψ carries the dimension of a volume transport ($\text{m}^3 \text{s}^{-1}$, usually measured in Sverdrup: $1 \text{ Sv} = 10^6 \text{ m}^3 \text{s}^{-1}$).

A useful property of the stream function stems from the fundamental theorem of calculus for line integrals, which reads

$$\Psi(\vec{q}) - \Psi(\vec{p}) = \int_{\gamma} \nabla\Psi(\vec{r}) \cdot d\vec{r} \simeq \int_{\gamma} (V dx - U dy)$$

with γ denoting an arbitrary path between the points \vec{q} and \vec{p} . This essentially implies that the difference of the stream function at two different locations gives the net volume flux through any path connecting them.

Vorticity Equation

With the approximations made so far, the general vorticity equation (1.8) can be simplified substantially. First of all, only the vertical component of $\vec{\omega}_a$ is of

¹⁵ For a review of the Helmholtz-Hodge decomposition see e.g. Bhatia et al., 2013.

RELATIVE VORTICITY
for horizontal flow

16. This eliminates the baroclinic and tilting terms.

$$\zeta := \nabla_H \times \vec{u} = v_x - u_y.$$

The vertical component of the vorticity equation (1.8), as obtained from the leading-order momentum equations as in (1.15)¹⁶, thus reads

$$\frac{D}{dt}(\zeta + f) + (f + \zeta) \nabla_H \cdot \vec{u} = \nabla_H \times \vec{\mathcal{F}}. \quad (1.16)$$

Replacing the divergence term $\nabla_H \cdot \vec{u}$ via the continuity equation for incompressible flow, (1.5), (1.16) can be written as

$$\frac{D}{dt}(\zeta + f) = (\zeta + f) w_z + \nabla_H \times \vec{\mathcal{F}}. \quad (1.17)$$

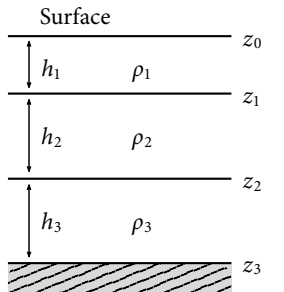
VORTICITY EQUATION
for horizontal flow

In this case, the horizontal flow is *not* non-divergent, but instead introduces the term w_z into the vorticity equation. This is justified when realizing that the term $(\zeta + f) \nabla_H \cdot \vec{u}$ involves velocities of a higher order than the ones in geostrophic balance — the vorticity equation for *purely* geostrophic flow would simply read $D/dt(\zeta + f) = 0$, which could hardly lead to any interesting dynamics.

1.1.3 Layered Model

17. In the sense that no diapycnal mixing occurs, i. e., surfaces of constant density stay strictly separated with no flow between them.

Consider an adiabatic¹⁷ ocean model with n layers, each of height $h_n = z_{n-1} - z_n$ and constant density ρ_n , in which the vertical length scale is much smaller than the horizontal. These assumptions, and the insights obtained from the leading-order dynamics described in § 1.1.2, lead to a powerful approximation of the real ocean dynamics.



Structure of the layered model

Momentum & Continuity Equations

Starting with hydrostatic balance (1.13), i. e.,

$$p_z = -\rho g,$$

an expression for the pressure p_n in the n -th layer can be obtained:

$$p_n = -\rho_n g(z - z_n) - \sum_{i=1}^{n-1} \rho_i g h_i. \quad (1.18)$$

This can be rewritten using a dynamic pressure π , which only depends on the current stratification:

$$p_n = -\rho_n g z + \rho_0 \pi(x, y, t)$$

with the average (background) density ρ_0 . This expression for p_n implies that the terms p_x and p_y appearing in the horizontal momentum equations cannot depend on z inside a particular layer. Hence, it makes sense that the horizontal velocities themselves are independent of z , i. e., $u_z = v_z \approx 0$, leading to the same structure of the horizontal momentum equations already found in § 1.1.2 (applied to each layer):

$$\begin{aligned} u_t + uu_x + vu_y - fv &= -\frac{(p_n)_x}{\rho_0} + \hat{x} \cdot \vec{\mathcal{F}} \\ v_t + uv_x + vv_y + fu &= -\frac{(p_n)_y}{\rho_0} + \hat{y} \cdot \vec{\mathcal{F}}. \end{aligned}$$

In the special case of a two-layer ocean, (1.18) implies

$$\begin{aligned} p_1(z) &= -\rho_1 g(z - z_0) \\ p_2(z) &= -\rho_2 g(z - z_1) - \rho_1 g h_1. \end{aligned}$$

For the lower layer, this means that the pressure terms in the momentum equation (1.3) take on the form

$$-\frac{(p_2)_x}{\rho_0} = \frac{g}{\rho_0}(\rho_1(h_1)_x + \rho_2(z_1)_x) \approx \frac{g(\rho_2 - \rho_1)}{\rho_0}(h_1)_x =: \gamma(h_1)_x,$$

using the assumption that displacements of the surface z_0 are small compared to the interfacial displacement¹⁸ z_1 , and hence $(h_1)_x \approx -(z_1)_x$. The so-defined parameter γ is called *reduced gravity* and is of the order 0.01 m s^{-2} , since horizontal density variations in the ocean are usually negligible. This retroactively justifies the assumption that interfacial displacements are much larger than those of the surface, since interfacial displacements only need to overcome a much smaller restoring force (γ instead of g). This is a direct consequence of buoyancy that acts to greatly reduce the effect of gravity on interfacial displacements when density differences are small.

What is remaining is an expression for the evolution of the layer heights h_n . By integrating the continuity equation over a layer we get:¹⁹

$$0 = \int_{z_n}^{z_{n-1}} \nabla \cdot \vec{u} \, dz = h_n u_x + h_n v_y + w(z_{n-1}) - w(z_n). \quad (1.19)$$

¹⁸. This is often referred to as the *rigid lid* condition.

¹⁹. Recall that neither u nor v depends on z .

Since there cannot be any flow across the interface boundaries, a kinematic boundary condition must be fulfilled:

$$w = \frac{D}{dt}z \rightarrow \lim_{z \rightarrow z_n} w \stackrel{!}{=} \frac{D}{dt}z_n.$$

This essentially says that the change of depth of a particle along a stream line close to the interface must be the same as the change of the depth of the interface itself (which is of course not the case for cross-interfacial flow). The boundary terms involving w can thus be rewritten as

$$\begin{aligned} w(z_n) &= (z_n)_t + u(h_n)_x + v(h_n)_y \\ w(z_{n-1}) &= (z_{n-1})_t + u(h_{n-1})_x + v(h_{n-1})_y, \end{aligned}$$

leading to, assuming $u(z) \equiv u$, $v(z) \equiv v$:

$$\begin{aligned} 0 &= h_n(u_x + v_y) + (z_{n-1} - z_n)_t + u(z_{n-1} - z_n)_x + v(z_{n-1} - z_n)_y \\ &= (h_n)_t + h_n \nabla_H \cdot \vec{u} + \vec{u} \cdot \nabla_H h_n \\ &= \frac{D}{dt}h_n + h_n \nabla_H \cdot \vec{u}, \end{aligned} \tag{1.20}$$

CONTINUITY EQUATION for the layered model

which is the desired equation describing the evolution of the layer height.



Note that the surface and bottom terms in (1.19) can be neglected entirely if

$$\frac{\mathcal{O}(w_b)}{\mathcal{O}(hu_x)} = \frac{UE/L}{UH/L} = \frac{E}{H} \ll 1 \tag{1.21}$$

with E denoting a typical scale of the *layer height anomaly* η i. e., the deviation of h from an undisturbed layer height H . To put (1.21) into words: If the fluctuations in layer height are small compared to the mean height of the layer, the boundary terms in the integrated continuity equation (1.19) vanish, and the horizontal flow becomes divergence-free. It can then be expressed through a stream function

$$U = \int_{z_n}^{z_{n-1}} u \, dz = -\Psi_y, \quad V = \int_{z_n}^{z_{n-1}} v \, dz = \Psi_x.$$

Flow fulfilling the condition posed by (1.21) is called *quasi-geostrophic*, which is obviously the case when integrating over the entire depth of the ocean (this even holds if u and v depend on z).

Vorticity Equation & Potential Vorticity

Since the momentum equations for the layered model are of the same form as for the leading-order model described in § 1.1.2, the vorticity equation must also be of a similar form. Replacing $\nabla_H \cdot \vec{u}$ in (1.16) by the corresponding term given in (1.20) gives

$$\frac{D}{dt}(\zeta + f) = -\frac{\zeta + f}{h_n} \frac{Dh_n}{dt} + \nabla_H \times \vec{\mathcal{F}},$$

which is equivalent to

$$\frac{D}{dt} \left(\frac{\zeta + f}{h_n} \right) = \frac{1}{h_n} \nabla_H \times \vec{\mathcal{F}}. \quad (1.22)$$

Hence, the *potential vorticity* Π_s is in this case

$$\Pi_s = \frac{\zeta + f}{h_n}, \quad (1.23)$$

POTENTIAL VORTICITY
in a layered ocean

which differs from the general form of the PV only by a constant factor (ρ). In fact, (1.23) is probably the most frequently used formulation of potential vorticity, at least for mostly horizontal flow. It is extremely useful because its evolution, as given by (1.22), reveals the dominant mechanisms behind the large-scale circulation in a layered ocean: As water flows in meridional direction (i.e., towards a different f), the water column can either adjust by assuming a relative rotation (ζ), by squeezing or stretching of the entire layer (h_n), or by dumping excess vorticity through friction ($\vec{\mathcal{F}}$).

1.2 NOTABLE SOLUTIONS

Under certain assumptions, the model equations presented in the previous sections can be solved analytically, yielding solutions for the ocean circulation that are good approximations in large regions of the ocean. Two such solutions are discussed in this section: The Sverdrup solution for the ocean interior, and the Munk solution for a frictional western boundary current.

1.2.1 Sverdrup Theory

Considering a linear, frictionless, steady, homogeneous ocean forced by wind stress only leads to a powerful theory for the interior ocean circulation, called

20. Leading to a balance between advection of planetary vorticity and curl of frictional forces (in this case wind stress).

Sverdrup Theory, which was introduced in Sverdrup, 1947, and is covered in depth in Pedlosky, 1996. It is a depth-integrated form of the vorticity equation (1.17), using the following key assumptions²⁰:

- ▶ A low Rossby number R_0 , i. e., the condition that nonlinear terms are negligible in comparison to the Coriolis term (and thus the geostrophic balance):

$$R_0 = \mathcal{O}\left(\frac{\vec{u} \cdot \nabla u}{fv}\right) = \frac{U^2/L}{fU} = \frac{U}{fL} \ll 1,$$

with a typical velocity scale U and horizontal length scale L .

- ▶ A low horizontal Ekman number E_H , i. e., the condition that diffusive terms are negligible in comparison to geostrophy:

$$E_H = \mathcal{O}\left(\frac{A_H \nabla^2 u}{fv}\right) = \frac{A_H U / L^2}{fU} = \frac{A_H}{fL^2} \ll 1,$$

with a horizontal turbulent diffusion constant A_H .

Typical values in the interior ocean would be $U \approx 1 \text{ cm s}^{-1}$, $L \approx 1000 \text{ km}$, $f \approx 10^{-4} \text{ s}^{-1}$, and $A_H \approx 10^{-4} \text{ m}^2 \text{ s}^{-1}$ (as found in eddy-resolving models e. g. by Bryan, 1987), leading to both $R_0 \approx 10^{-4}$ and $E_H \approx 10^{-4}$.

With these assumptions, the famous Sverdrup relation connects the horizontal stream function Ψ of the vertically integrated flow to the surface wind stress $\vec{\tau}$ alone:

SVERDRUP RELATION in spherical coordinates

$$\Psi = \frac{-1}{\rho_0 \beta} \int_{\phi}^{\phi_E} \operatorname{curl}(\vec{\tau}) R_E \cos \theta \, d\phi' \quad (1.24)$$

with

- ▶ the Earth's radius $R_E \approx 6371 \text{ km}$;
- ▶ the Coriolis parameter $\beta = \frac{\omega}{R_E} \cos \theta \approx f_y$;
- ▶ the latitude of the nearest eastern boundary ϕ_E ; and
- ▶ the curl of the horizontal wind stress $\vec{\tau}$, in spherical coordinates:

$$\operatorname{curl}(\vec{\tau}) = \frac{1}{R_E \cos \theta} \left(-(\hat{x} \cdot \vec{\tau} \cos \theta)_\theta + (\hat{y} \cdot \vec{\tau})_\phi \right).$$

Validity of the Sverdrup Relation

Even though Sverdrup theory is a drastic simplification of the real ocean, it leads to a realistic interior circulation in the subtropical gyres (Fig. 1.1), which

is why it is of such importance in Physical Oceanography. However, it does not lead to a closed circulation at the western boundary, since the winds have no notable zonal structure (and thus, the value of Ψ depends mostly on the distance to the eastern boundary).

This implies that effects that have been neglected in Sverdrup theory must be dominant near the western boundaries. This is also directly evident from (1.24): Since the equation for Ψ is first order in ϕ , it cannot satisfy a no-normal-flow boundary condition at the eastern and western edges of the basin at the same time.

1.2.2 Western Boundary Currents

The most common approach to tackle this inconsistency of Sverdrup theory is to assume a western boundary layer that is dominated by dynamics that have been neglected in the interior, and smoothly joins the Sverdrup interior solution given by (1.24) for large distances from the western boundary.

Dramatically changed length and velocity scales have to be taken into account when dealing with western boundary currents. One real-world example for such a current is the Kuroshio (Fig. 1.2), which is located in the North Pacific (analogous to the Gulf Stream in the North Atlantic). Liu and Gan, 2012 give a width of the Kuroshio of about 200 km, and an along-stream mean velocity of about 35 cm s^{-1} . Thus, both Rossby and horizontal Ekman numbers can safely be assumed to be several magnitudes larger at the western boundary, and any successful theory must include the terms that have been neglected during the derivation of the Sverdrup relation.

The Munk Boundary Layer

One simple solution for the western boundary was published in Munk, 1950. It assumes a linear ocean (i. e., a low Rossby number), but includes a frictional term of the form

$$\vec{\mathcal{F}} = A_H \nabla^2 \vec{u}$$

with a constant diffusion coefficient A_H . This leads to

$$\operatorname{curl}(\vec{\mathcal{F}}) = A_H \nabla^2(v_x - u_y) = A_H \nabla^2 \zeta = A_H \nabla^4 \Psi,$$

where ∇^4 denotes the biharmonic differential operator such that

$$\nabla^4 \Psi = \Psi_{xxxx} + 2\Psi_{xxyy} + \Psi_{yyyy}.$$

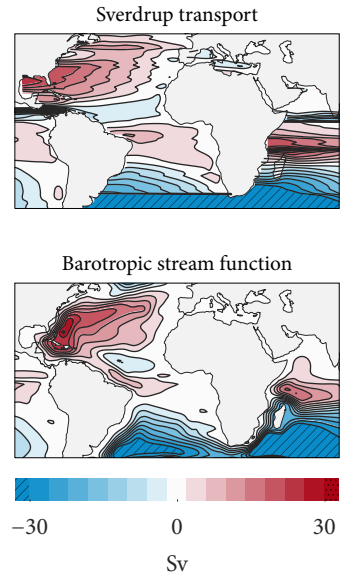


Figure 1.1: Sverdrup theory as a first approximation of the ocean circulation. Shown is the transport in Sverdrups ($1 \text{ Sv} = 10^6 \text{ m}^3 \text{ s}^{-1}$), estimated using (1.24) (top) and the BSF (bottom). Data from CESM model output.

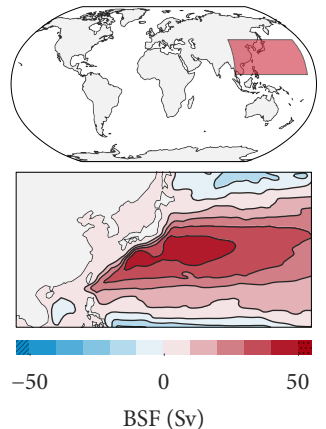


Figure 1.2: Location, scale and magnitude of the Kuroshio in the 1° CESM default run.

21. Assuming a so-called β -plane, i. e., $f \approx f_0 + \beta y \rightarrow f_y \approx \beta$.

As already stated, Munk assumed a linear boundary layer, hence dropping all nonlinear terms. Also, for the sake of simplicity, he assumed a strictly meridional boundary current, with a zonal length scale L_x that is much smaller than the meridional length scale L_y (i. e., , a narrow boundary current connecting North and South), leading to the assumption that $\Psi_x \gg \Psi_y$. A steady-state solution can then be found from the vorticity equation (1.17), retaining only the dominant balance between Coriolis force²¹ and frictional forces:

$$\beta \Psi_x = A_H \Psi_{xxxx}. \quad (1.25)$$

At the boundaries, it is required that $\lim_{x \rightarrow 0} \Psi(x) = 0$ and $\lim_{x \rightarrow \infty} \Psi(x) = \Psi_I(x, y)$, with Ψ_I being the Sverdrup interior solution as in (1.24). The fourth-order ordinary differential equation (ODE) (1.25) is then solved by

MUNK'S SOLUTION

$$\Psi = \Psi_I(x, y) \left[1 - e^{-x/(2\delta_M)} \cos \left(\frac{\sqrt{3}x}{2\delta_M} \right) \right] + C(y) e^{-x/(2\delta_M)} \sin \left(\frac{\sqrt{3}x}{2\delta_M} \right),$$

where

$$\delta_M = \left(\frac{A_H}{\beta} \right)^{1/3} \quad (1.26)$$

denotes a characteristic boundary layer width, and $C(y)$ is to be determined by a boundary condition for v at the western boundary (i. e., , parallel to the boundary). For no-slip boundary conditions, the Munk solution reads (Pedlosky, 1996):

$$\begin{aligned} \Psi &= \Psi_I \left[1 - \exp \left(-\frac{x}{2\delta_M} \right) \left(\cos \frac{\sqrt{3}x}{2\delta_M} + \frac{1}{\sqrt{3}} \sin \frac{\sqrt{3}x}{2\delta_M} \right) \right] \\ v &= \frac{2}{\sqrt{3}} \frac{\Psi_I}{\delta_M} \exp \left(-\frac{x}{2\delta_M} \right) \sin \left(\frac{\sqrt{3}x}{2\delta_M} \right). \end{aligned} \quad (1.27)$$

Boundary Conditions

In computational fluid dynamics, a multitude of different lateral boundary conditions is used, each best suited for a specific range of physical problems. Probably the most popular boundary condition for flow tangential to a boundary is the *no-slip* condition, which is motivated through a micro-scale picture of the flow: On a molecular level, fluid particles located immediately next to a wall tend to stick to it — hence, the velocity shear between wall and fluid is enforced to be zero, i. e.,

**NO-SLIP
Boundary Condition**

$$\vec{u} \cdot \hat{t} = 0 \quad \text{or} \quad \hat{n} \cdot \nabla \Psi = 0$$

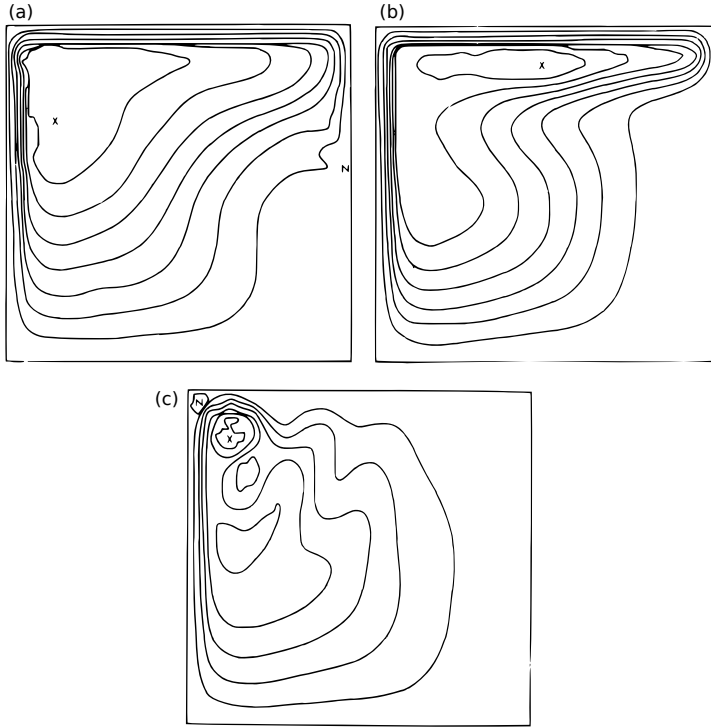


Figure 1.3: Different boundary conditions may lead to large changes in the circulation. Shown are streamlines for (a) bottom friction only, (b) lateral friction with slip, and (c) lateral friction with no-slip boundary conditions. From Blandford, 1971.

with unit vectors \hat{t} , \hat{n} tangential and normal to the boundary, respectively.

However, it is unclear why the argument of molecules sticking to a wall should apply to flow that is resolved at a scale of hundreds of kilometers. Boundary conditions that are frequently used in ocean modeling include the

- ▶ No-slip condition: $\vec{u} \cdot \hat{t} = \hat{n} \cdot \nabla \Psi = 0$;
- ▶ Free-slip condition: $\zeta = \nabla^2 \Psi = 0$;
- ▶ Superslip condition²²: $\hat{n} \cdot \nabla \zeta = 0$; and
- ▶ Hyperslip condition: $\hat{n} \cdot \nabla(\zeta + \beta y) = 0$.

²². When employing superslip or hyperslip conditions, the friction term may actually *add* energy to the flow through the boundary (Pedlosky, 1996).

Each of the described boundary conditions stems from a reasonable physical view of the interaction between wall and fluid (Pedlosky, 1996). It is thus not possible to choose one particular of those boundary conditions *a priori*, since neither is derived from first principles, and the boundary conditions in the real ocean are still unknown. The chosen boundary condition may impact the resulting circulation strongly (Fig. 1.3), and many numerical studies include simulations with several choices of boundary conditions (e. g. Killworth, 1991).



Although the “correct” boundary condition is unknown, and although the transformation of vorticity in a boundary current *is* sensitive to the chosen

boundary condition (see *Geophysical Fluid Dynamics* (Pedlosky, 1992), Chapter 5), I will focus on the no-slip boundary condition in this thesis, since it is the only one that is deployed in CESM.

1.3 FRICTION AND VISCOSITY

During the derivation of the ocean models described so far, frictional forces were intentionally left as general as possible (described through the unspecified term $\vec{\mathcal{F}}$). This was done because there simply is no unique answer to the question *how this term should look like*. The two most popular formulations, a turbulent diffusion term and a bottom friction term, shall be introduced in the following sections (§ 1.3.1 and § 1.3.2, respectively). Both of these terms are inherently over-simplifying the real processes, but often lead to a realistic picture of the ocean while allowing for analytical solutions of some simple special cases, which explains why they have become so popular.

After introducing these two formulations of friction, § 1.3.3 and § 1.3.4 discuss some of the numerical aspects involved when solving diffusive partial differential equations (PDEs) (concerning numerical stability and noise, respectively).

1.3.1 Turbulent Diffusion

“
*Big whirls have little whirls,
 That feed on their velocity;
 And little whirls have lesser
 whirls,
 And so on to viscosity.*
 ”
 —Lewis Fry Richardson

The reason why a diffusive friction term $\vec{\mathcal{F}} \sim A \nabla^2 \vec{u}$ is often chosen as a parameterization for lateral friction is *not* because molecular diffusion is a particularly important process in the ocean — in fact, it is in most cases negligible to a very high degree. The kinematic viscosity ν of water is of the order of magnitude $10^{-6} \text{ m}^2 \text{ s}^{-1}$, which, if ν were the only contribution to the diffusivity A , would imply that diffusive friction were utterly unimportant compared to other terms. However, it can be shown that unresolved turbulent motion can be modeled as a diffusive process: Turbulence creates mesoscale eddies with a typical size of $\lesssim 100 \text{ km}$. Those eddies, superimposed on the mean flow, induce a velocity shear that acts to distribute momentum just like molecular diffusion, but several orders of magnitude stronger. A typical value for the *turbulent diffusivity* A_H is $10^5 \text{ m}^2 \text{ s}^{-1} \gg \nu$. The derivation of the turbulent diffusion term is laid out in *Geophysical Fluid Dynamics* (Pedlosky, 1992), Chapter 4 — here, we shall only sketch the most important ideas and assumptions going into it.

The starting point for the derivation of the turbulent diffusion term is the Reynolds decomposition: The flow field \vec{u} is decomposed into a mean flow, $\langle \vec{u} \rangle$, and a (turbulent) small-scale flow, \vec{u}' , such that²³

$$\vec{u} = \langle \vec{u} \rangle + \vec{u}' \quad (1.28)$$

²³ It is already unclear whether this decomposition makes sense, i. e., whether there exists an averaging time scale that is sufficiently short compared to the natural time scale of $\langle \vec{u}' \rangle$.

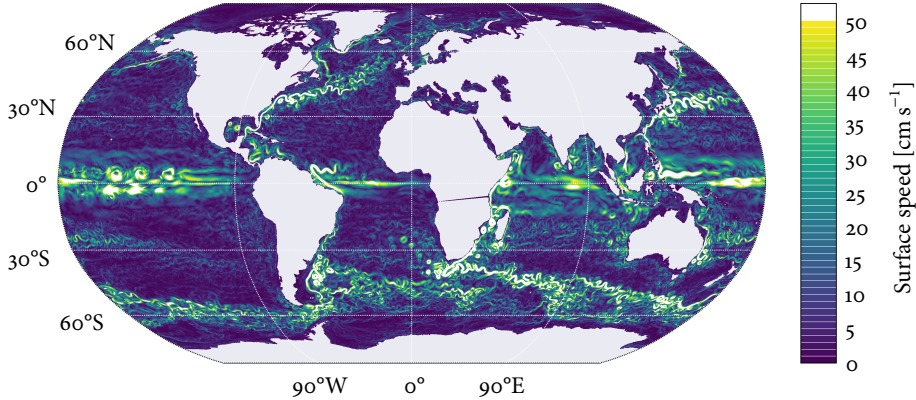


Figure 1.4: Turbulence in the ocean. Snapshot of the ocean surface speed in an eddy-resolving model (effective resolution 0.1°). Modeled with CESM in a quasi-equilibrated control simulation. Note the widening effect of eddies on western boundary currents (e.g. Gulf Stream and Kuroshio). Part of Mads Poulsen's PhD project.

which implies

$$\langle \vec{u} \rangle = \langle \langle \vec{u} \rangle \rangle + \langle \vec{u}' \rangle \rightarrow \langle \vec{u}' \rangle = 0.$$

Inserting (1.28) into the momentum equations, and identifying terms of the form $\langle u'v' \rangle$ with the components of a stress tensor²⁴ τ , such that e. g.

$$\langle u'v' \rangle = -\frac{\tau^{xy}}{\rho},$$

leads to momentum equations of the form:²⁵

$$u_t + (\vec{u} \cdot \nabla)u - fv = -\frac{1}{\rho}p_x + \frac{1}{\rho}(\tau_{x}^{xx} + \tau_y^{xy} + \tau_z^{xz}) + v\nabla^2u. \quad (1.29)$$

This formulation of the momentum equations still contains the unknown stresses (in terms of the mean flow) τ^{ij} . Finding a formulation for τ that depends on the mean flow \vec{u} only is called the *closure problem*, and is highly non-trivial (Pedlosky, 1992). A simple (but crude) closure is obtained by assuming that the stress acting on the fluid depends linearly on the shear of the velocity field, such that

$$\tau^{ij} = \rho(A^i(\hat{j} \cdot \vec{u})_i + A^j(\hat{i} \cdot \vec{u})_j).$$

Then, the stress terms in the momentum equation for u (1.29) become

$$\frac{1}{\rho}(\tau_x^{xx} + \tau_y^{xy} + \tau_z^{xz}) = (A^x u_x)_x + (A^y u_y)_y + (A^z u_z)_z,$$

and analogous formulations are found for the other components of the momentum equation. In the special case of constant diffusion coefficients $A^x(x, y, z) \equiv$

²⁴ These stresses are consequently dubbed Reynolds-stresses.

²⁵ Ddropping the averaging operators, i. e., $u \equiv \langle u \rangle$

$A^y(x, y, z) \equiv A_H$ and $A^z \equiv 0$, this reduces to the well-known form of lateral diffusive friction:

$$\vec{\mathcal{F}} = A_H \nabla_H^2 \vec{u}.$$

Another important reason why this simple solution of the closure problem is widely used in Oceanography is a practical one: A friction term depending on the curvature of the flow field (i. e., $\nabla^2 \vec{u}$) acts to reduce numerical errors present in most implementations: many discretizations of the momentum PDEs introduce noise on a scale of one grid spacing Δx . This small-scale noise inherently leads to a large curvature of the flow, which is effectively dissipated by diffusive friction. It is thus usually desirable to include a diffusive term into the model equations (cf. § 1.3.4).

Because A_H is determined by unresolved small-scale motion, this formulation depends on the model resolution at hand. In eddy-resolving models (that, on a global scale, can only be run at the World's largest super computers), A_H can be chosen extremely small, as the effects of turbulence on the mean flow are modeled directly through the nonlinear terms of the small-scale flow (such as e. g. $u'v'$). Those high-resolution models with a spatial scale of $\lesssim 20$ km reveal the true turbulent nature of the ocean (Fig. 1.4).

1.3.2 Bottom Friction

In his ground-breaking paper, Henry Stommel was the first to tie the observed westward intensification of the ocean circulation to the Earth's planetary vorticity gradient (Stommel, 1948), just like Walter H. Munk did several years later (Munk, 1950). The western boundary current solution Stommel presented is different from the Munk solution in that it uses different friction term: Instead of including a diffusive lateral friction model, Stommel introduced a mathematically much simpler Rayleigh friction term acting to dissipate momentum directly:

$$\vec{\mathcal{F}} = -\kappa \vec{u}. \quad (1.30)$$

Though seemingly highly artificial, this term can be motivated in the framework of boundary layer theory. Considering a frictional boundary layer (Ekman layer) at the bottom of the ocean, it can be derived that the frictional drag acting on the interior flow creates a vertical motion, which in turn leads to a Rayleigh dissipation term like (1.30) to leading order, as laid out in *Geophysical Fluid Dynamics* (Pedlosky, 1992).

Many authors decide to introduce friction into their model via a bottom friction term alone (e. g. Kawase, 1987), and the question whether bottom or lateral friction is dominant in the ocean is still unanswered. Bottom friction is present

in Parallel Ocean Program 2 (POP2) and thus CESM, but is playing a minor role compared to lateral friction.

1.3.3 Stability Conditions

When solving a system of non-stationary advection-diffusion equations (such as the nonlinear and friction terms in the momentum equations (1.3)), i. e.,

$$\overrightarrow{u}_t + \underbrace{(\overrightarrow{u} \cdot \nabla) \overrightarrow{u}}_{\mathcal{L}\overrightarrow{u}} - A \nabla^2 \overrightarrow{u} = 0$$

Considerations in this section follow Chapters 4, 5 & 6 of *Principles of Computational Fluid Dynamics* by Pieter Wesseling (Wesseling, 2009).

it is usually transformed into a system of ODEs by discretizing the spatial part of the PDE (in form of the spatial operator \mathcal{L}) into a discrete operator \mathcal{L}_h :

$$(\overrightarrow{u}_h)_t = -\mathcal{L}_h(\overrightarrow{u}_h) \overrightarrow{u}_h. \quad (1.31)$$

where \overrightarrow{u}_h just denotes a discrete version of the continuous velocity \overrightarrow{u} . In (1.31), \mathcal{L}_h depends on \overrightarrow{u}_h due to the advection term $(\overrightarrow{u} \cdot \nabla) \overrightarrow{u}$. However, although unproven in the general case, it is usually conjectured that a discretization of the nonlinear term is stable if and only if the method is stable for an operator that only depends on a “frozen” value of u (see e. g. Chorin, 1968), i. e., if $\overrightarrow{u}_h = -\mathcal{L}_h(\overrightarrow{u}_h^*) \overrightarrow{u}_h$ is stable. The stability analysis is thus carried out for a convection-diffusion problem, and assumed to hold for the advection-diffusion equations as well. Using an explicit *finite difference scheme*²⁶, \mathcal{L}_h becomes:

$$\Delta t \mathcal{L}_h = \sum_i \left[\underbrace{\frac{|\hat{i} \cdot \overrightarrow{u}_h^*| \Delta t}{\Delta x_i}}_{c_i} \Gamma_i(\overrightarrow{u}_h) + \underbrace{\frac{2A \Delta t}{(\Delta x_i)^2}}_{d_i} \Lambda_i(\overrightarrow{u}_h) \right]$$

with

- ▶ A sum over all coordinates i (in this case, i corresponds to x, y, z);
- ▶ Time step size Δt ;
- ▶ Mesh sizes Δx_i ;
- ▶ Discretizations for the convection and diffusion terms, Γ and Λ , respectively. Simple (but bad) formulations for these terms would be²⁷

$$\begin{aligned} \Gamma_i \overrightarrow{u}_h &= u_i^{j+1} - u_i^j \\ &\text{and} \\ \Lambda_i \overrightarrow{u}_h &= \frac{1}{2} u_i^{j-1} - u_i^j + \frac{1}{2} u_i^{j+1} \end{aligned}$$

26. Implicit schemes are also possible, and usually lead to a much larger stability region, but they come with an additional computational cost for solving a linear system in every time step.

27. More sophisticated discretizations such as upwinding or κ -schemes are given in Wesseling, 2009.

with $u_i \equiv \hat{i} \cdot \vec{u}_h$ and assuming $u_i > 0$.

The dimensionless parameters c_i are called *CFL numbers*, and were first introduced in Courant, Friedrichs, and Lewy, 1928. d_i are sometimes called diffusion numbers, or diffusive CFL numbers.

A stability condition for the resulting ODE can then be obtained using e.g. von Neumann analysis, and depends on the chosen discretization of the time derivative, $(u_h)_t$. Wesseling, (2009) derives stability criteria for several popular time discretization schemes, which all relate c_i and d_i to constant values. For a second order central difference scheme in space and explicit Euler in time, one obtains the following necessary and sufficient conditions for stability:

CFL CONDITION

$$\sum_i \frac{c_i^2}{d_i} \leq 1$$

and

VISCOUS CFL CONDITION

$$\sum_i d_i \leq 1. \quad (1.32)$$

²⁸ As given in the POP2 manual, Smith et al., 2010.

Since in CESM both Δx_i and Δt are fixed, (1.32) leads to a condition for the viscosity A :²⁸

$$A \leq A_{\text{cfl}} = \frac{\Delta x^2 + \Delta y^2}{4 \Delta t}$$

This limits the values of viscosity that can be used during the model runs in Chapter 3.

1.3.4 Numerical Noise

There are several processes that may introduce artificial dispersive noise into the numerical solution of a differential equation. The most straightforward way to see how this happens is by considering central finite differences, such as

$$\left. \frac{\partial f}{\partial x} \right|_{x_i} \approx \frac{f(x_{i+1}) - f(x_{i-1})}{x_{i+1} - x_{i-1}}$$

as an approximation of the gradient of a function f in x -direction. This scheme connects the value of f at a point x_i with the values at x_{i+1} and x_{i-1} alone. This means that grid points at even and odd i may decouple in the steady state, creating an alternating pattern in the solution (sometimes referred to as

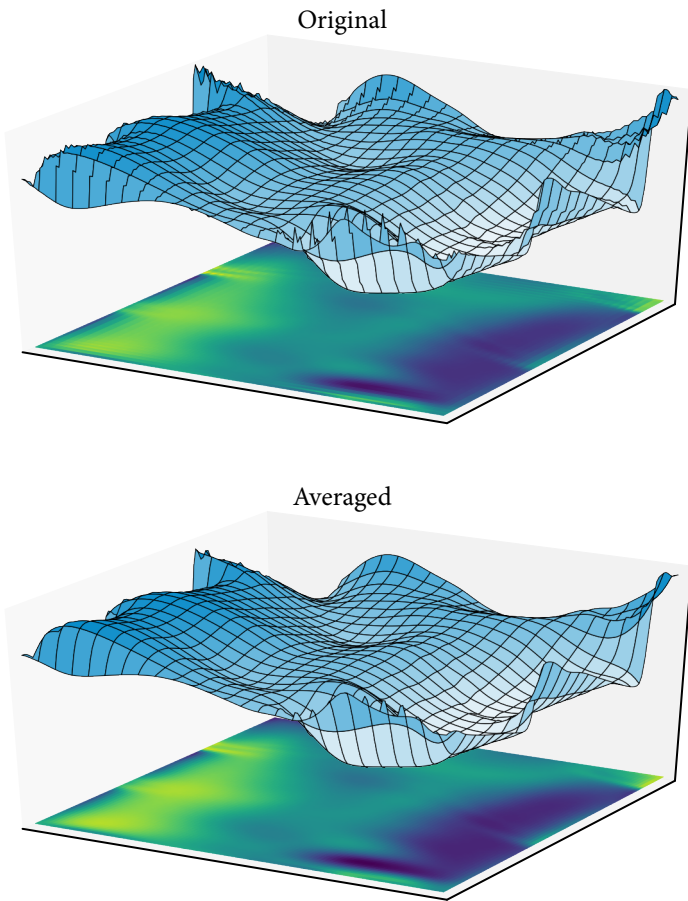


Figure 1.5: The generation of numerical noise in a shallow-water model without lateral friction. Note the jagged edges along the boundaries. Bottom figure shows the reduction of noise in the same data averaged with a boxcar filter.

checkerboard effect). Since the pressure and nonlinear terms in the momentum equations both involve a first derivative in space, this effect can also be observed in many ocean simulations when these terms become dominant.

One important feature of this type of noise is that it occurs on *grid scale*. This allows us to quantify and filter dispersive noise, e. g. by averaging over adjacent grid cells (Fig. 1.5), as in Jochum et al., 2008.

1.4 GLOBAL OCEAN CURRENTS

This section presents some of the features of the *observed* ocean circulation (in contrast and comparison to the theoretical findings described in § 1.2). Since the focus of my thesis lies on the global-scale ocean circulation (the Meridional Overturning Circulation (MOC)), a description of the gyre circulations, which are mostly in Sverdrup balance (§ 1.2.1), is being omitted.

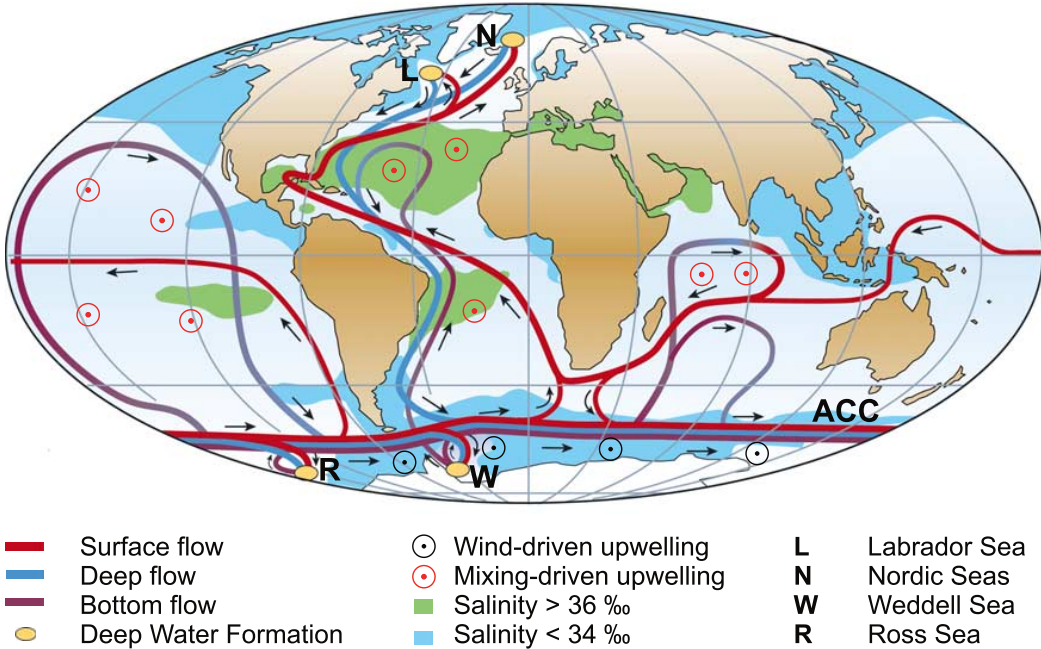


Figure 1.6: The MOC. From Kuhlbrodt et al., 2007, after Rahmstorf, 2002.

First up, the global features of the MOC as a whole are presented, followed by a more detailed examination of some local regions of interest like the Atlantic Meridional Overturning Circulation (AMOC) and the Indonesian Throughflow (ITF).

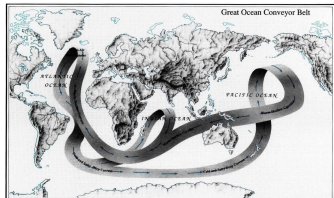


Figure 1.7: One of the first illustrations of the MOC. Broecker, 1991.

29. Note that only the density-driven thermohaline circulation is shown in these illustrations — flow in Sverdrup balance such as the gyre circulations are omitted.

1.4.1 The Meridional Overturning Circulation (MOC)

The idea of the MOC as a great global “conveyor belt” that connects water masses all around the world has inspired many generations of oceanographers: Parts of the MOC were described as early as the first half of the 20th century, e.g. in Wüst, 1935. The pathway of this conveyor belt has often been illustrated — one early, though quite simplified, depiction was done by Broecker for the *Natural History* magazine (Fig. 1.7), which in turn became a logo for the *Global Change Research Initiative* (see Broecker, 1991).

A more modern, and more accurate depiction of the MOC is found in Kuhlbrodt et al., 2007 (Fig. 1.6). This illustration correctly emphasizes the role of the Southern Ocean in distributing water masses between the world’s oceans²⁹. The crucial role of the Southern Ocean is also stressed in Marshall and Speer, 2012.

In the MOC, deep water created in the North Atlantic flows all the way south and joins the Antarctic Circumpolar Current (ACC). In this region, strong wind-driven upwelling eventually causes this water to emerge. Then, it flows

northward along one of the boundaries in the ocean (along the shore of Africa, South America, or Australia). Flow in the Atlantic then joins the AMOC (see below), while there is no similar deeply penetrating overturning circulation in the Pacific. In the Pacific, large parts of the flow from the Southern Ocean end up in zonal jets like the North-Equatorial Current (NEC), which returns water to the southern hemisphere mainly via the ITF.

The exact driving forces of the MOC and their relative importances are still largely unclear. Kuhlbrodt et al. suggest that, at least in the AMOC, both wind-driven and mixing-driven upwelling are crucial driving processes of the overturning.

1.4.2 Local Features

The Atlantic Meridional Overturning Circulation (AMOC)

The branch of the MOC that distributes water in the Atlantic all the way between the Southern Ocean and the Arctic is known as the AMOC. A great overview of the AMOC and the processes that control it is given in Kuhlbrodt et al., 2007. In their introduction, they state:

“The deep Atlantic meridional overturning circulation (AMOC) consists of four main branches: upwelling processes that transport volume from depth to near the ocean surface, surface currents that transport relatively light water toward high latitudes, deep-water formation regions where waters become denser and sink, and deep currents closing the loop. These four branches span the entire Atlantic on both hemispheres, forming a circulation system that consists of two overturning cells, a deep one with North Atlantic Deep Water (NADW) and an abyssal one with Antarctic Bottom Water (AABW).”

These features of the AMOC are also present in the numerical CESM simulations (Fig. 1.8). Roughly 12 Sv of water entering the Atlantic between the surface and a depth of about 1200 m is flowing northward, some of it upwelling at the equator, until high latitudes are reached. There, it is converted to North Atlantic Deep Water (NADW), sinking to a depth of about 1.4 to 3.0 km. This deep branch of the AMOC proceeds southward, all the way to the Southern Ocean, where the circulation is closed (not shown).

The second, abyssal overturning cell is located at depths of $\gtrsim 3$ km, but carries only a weak transport compared to the upper cell (2 Sv in the CESM 3° default run), and is not examined in this thesis.

Indonesian Throughflow

The Indonesian Throughflow (ITF) is the main pathway for water originating in the Southern Ocean from the Northern Pacific to the Indian Ocean, and thus

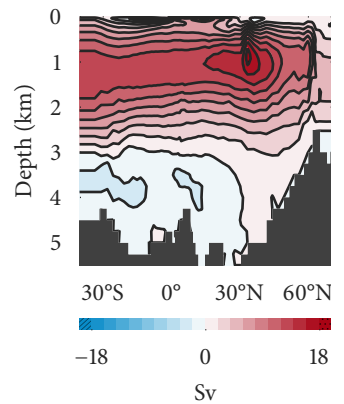


Figure 1.8: Vertical stream function of the AMOC in the CESM x3 default run.

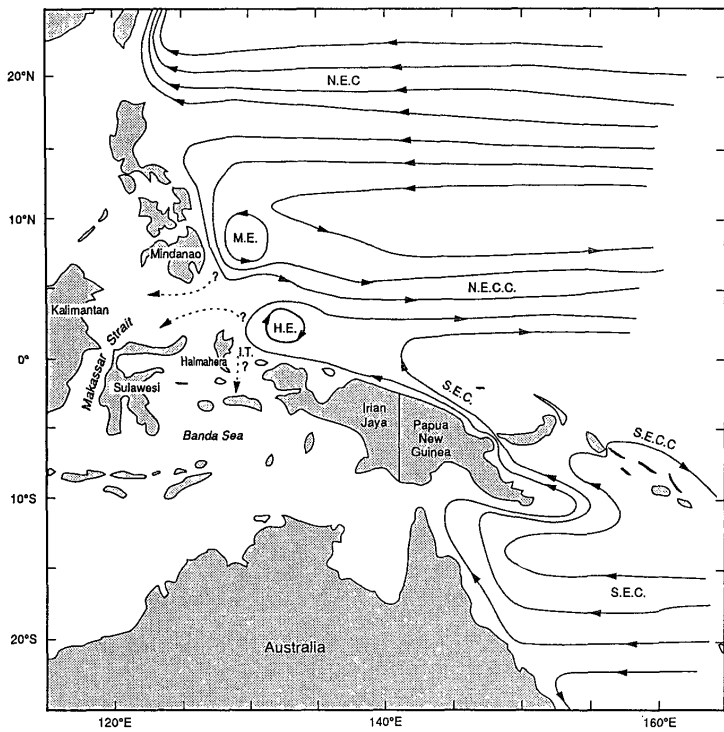


Figure 1.9: Currents in the ITF-region. After Godfrey, Wilkin, and Hirst, 1993. Note that Irian Jaya is officially called (West) Papua since 2002.

back to the southern hemisphere, closing the overturning in the Pacific (mean transport of about 15 Sv, Sprintall et al., 2009). Due to its complex pathway between the Indonesian islands, the ITF is sensitive to changes in geometry (Jochum et al., 2009), and thus might also be influenced by changes in viscosity.

³⁰ The Mindanao Current (MC) from the north and the New Guinea Coastal Undercurrent (NGCUC) from the south, which carries water from the South-Equatorial Current (SEC).

The ITF is located right at the point where two boundary currents³⁰ turn eastward between the islands of Mindanao, Halmahera, and Papua, feeding the North-Equatorial Countercurrent (NECC) (Fig. 1.9). In the retroflection regions, semi-permanent eddies form, the Mindanao and Halmahera eddies. From the Pacific Ocean, the ITF leads through either the Makassar Strait between Kalimantan and Sulawesi, or the Lifamatola Passage east of that.

CONTENTS

- 2 The Community Earth System Model 33**
 - 2.1 Model Grids 33**
 - 2.2 Initial Conditions & Forcing 34**
 - 2.3 Lateral Friction in CESM 35**

THE COMMUNITY EARTH SYSTEM MODEL

2

This chapter gives a brief introduction to CESM, the climate model I have used for my simulations, and Parallel Ocean Program 2 (POP2), the ocean model that is implemented in recent CESM versions. CESM is developed at the National Center of Atmospheric Research (NCAR), and the first version of its predecessor CCSM was released in 1983. CESM is widely used by research groups around the world, and simulations were e. g. included in several IPCC reports. In my experiments, I have used the current version of CESM, CESM 1.2.2, which was released during June 2014.

The following sections describe the structure of the dipole grids the solution is calculated on (§ 2.1), the initial state and forcing in the CESM ocean model (§ 2.2), and the anisotropic lateral friction parameterization that is used by default (§ 2.3).

2.1 MODEL GRIDS

Since POP2 (and thus CESM) operates only on grids that can be mapped onto a two-dimensional surface, every model grid necessarily contains two singularities, located at the poles in a naïve spherical coordinate mapping (i. e., $x = r \cos \theta \cos \phi$, $y = r \cos \theta \sin \phi$ with radius r , longitude ϕ , and latitude θ). Since singularities may cause numerical problems during solution or post-processing, the model grid is constructed in such a way that both singularities are located above land masses (Greenland and Antarctica, cf. Fig. 2.1), leading to a smooth ocean grid.

These so-called *dipole grids* were introduced by Madec and Imbard, (1996) and Smith, Kortas, and Meltz, (1995), and are created through an iterative process where the North Pole is displaced gradually, while the latitude circles are enforced to join a standard Mercator grid at the equator. In the northern hemisphere of a dipole grid, vectors like the velocities u and v are generally *not* strictly east-west / north-south aligned; however, for latitudes south of about 60°N, this effect is small.

In the following numerical experiments with CESM, two different grids are used:

- x1: 384 × 320 grid cells in the horizontal, 60 in the vertical. Zonal resolution of 1.125° (5 km at the poles vs. 125 km at the equator), meridional between

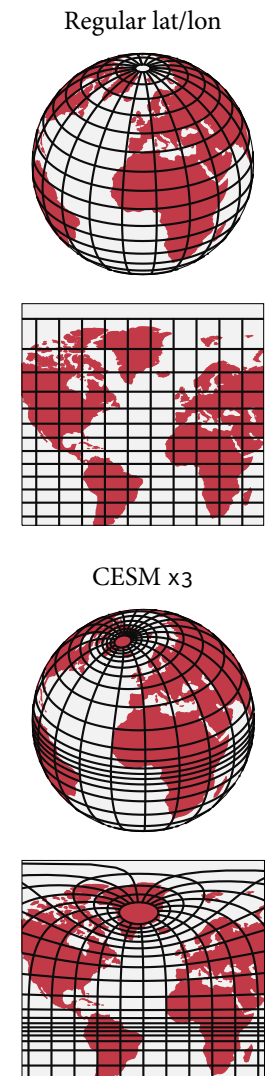


Figure 2.1: The CESM model grid in comparison to a regular latitude / longitude grid.

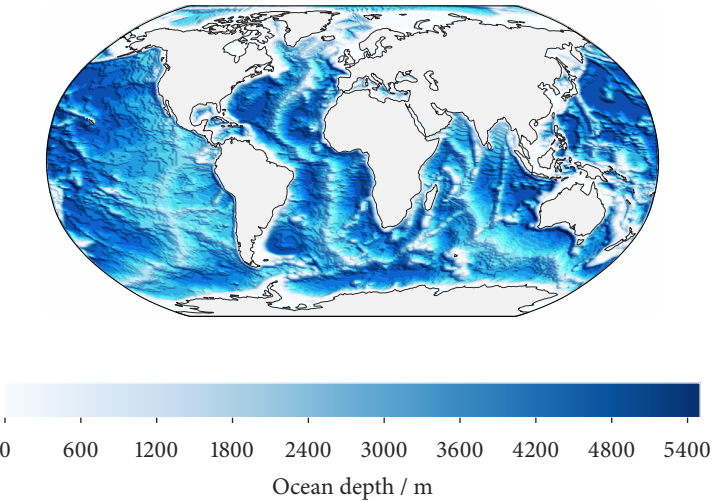


Figure 2.2: Bathymetry in the x_1 grid.

0.27° (28 km) and 0.5° (72 km), leading to an effective resolution of about 1° . Vertical layer height between 10 and 250 m.

x_3 : 116×100 horizontal grid cells. Zonal resolution 3.6° (17 km at the poles vs. 400 km at the equator), meridional between 0.6° (40 km) and 2.8° (380 km), effective resolution of about 3° . Vertical layering as in x_1 (see Fig. 2.2 for bathymetry).

Apart from the varying cell spacing, both grids are structurally identical.

Since the computational cost of the x_1 -grid is one order of magnitude higher than that of the x_3 grid, the 3° model is still widely used. Most of my numerical experiments have been carried out on the x_3 -grid (cf. Table 3.1); only three reference runs have been made with the x_1 version. A comparison of this low-resolution model to the intermediate and high-resolution CESM models can be found in Shields et al., 2012.

2.2 INITIAL CONDITIONS & FORCING

The initial conditions used in the ocean component of CESM are described in Danabasoglu et al., 2012. Tracer fields like temperature and salinity are initialized with a dataset created by blending data from Levitus et al., 1998 and Steele, Morley, and Ermold, 2001, representing mean conditions in January. The ocean is spun-up from rest, i. e., all velocities are initially zero.

Although CESM is perfectly capable of running fully coupled climate simulations, I have only used the ocean model with a static atmosphere for the

experiments in this thesis, since it requires much less computational resources and makes it easier to examine the response of the ocean without worrying about feedback with the atmosphere¹. The static atmospheric forcing that is applied is described in Large and Yeager, 2004 and combines many different data sets from observations. In order to obtain a solution that is as close to the observed present-day values as possible, some parameters such as wind speed and relative humidity have been fine-tuned in certain regions.

2.3 LATERAL FRICTION IN CESM

The actual lateral friction parameterization used in CESM was initially developed by Large et al., (2001) and refined by Smith and Gent, (2004) and Jochum et al., (2008). It uses a set of seven different parameters (Table 2.1), here denoted as ν_A , ν_B , ν_M , and ν_1 through ν_4 . Apart from regions where u is not aligned in east-west direction, i. e., away from the North pole, the lateral friction term is calculated as (Smith et al., 2010):

$$\vec{\mathcal{F}}_H = \begin{pmatrix} Au_{xx} + Bu_{yy} \\ Bv_{xx} + Av_{yy} \end{pmatrix} \quad (2.1)$$

with two spatially varying parameters A and B . From the form of (2.1), it becomes clear that A acts on curvature *parallel* to the flow, while B acts on curvature *perpendicular* to it. Note that while A and B are not strictly viscosities but rather a representation of diffusion through unresolved turbulence (cf. § 1.3.1), they are called viscosity parameters throughout CESM / POP2, so I will refer to these quantities as parallel (A) and perpendicular (B) viscosity parameters for the remainder of this study. This anisotropic formulation of the friction term has been chosen to allow for sharp features in the ocean circulation, while minimizing numerical noise (cf. § 1.3.4).

The viscosity parameters A and B are calculated in two steps (Jochum et al., 2008); first:

$$\begin{aligned} A' &= \max(A_{\text{SGS}}, A_{\text{Munk}}) \\ B' &= \max(B_{\text{SGS}}, B_{\text{Munk}}), \end{aligned}$$

and finally:

$$\begin{aligned} A &= \min(A', A_{\text{cfl}}) \\ B &= \min(B', B_{\text{cfl}}). \end{aligned}$$

The parameters A_{SGS} , B_{SGS} , A_{Munk} , B_{Munk} , A_{cfl} , B_{cfl} are calculated as follows:

1. Since I am mostly looking at kinematic processes, the findings in this study should be equally valid in a coupled simulation.

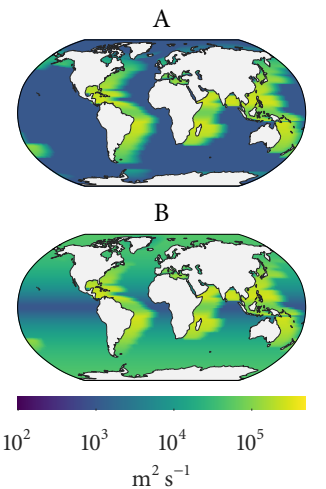


Figure 2.3: Viscosity parameters A and B in `x3_default`. Note the wide Munk layer with viscosities of the order $10^5 \text{ m}^2 \text{ s}^{-1}$ and the comparably low background values $\sim 10^3 \text{ m}^2 \text{ s}^{-1}$.

2. Formulation as in version 1.2.2 of the CESM source code.

- A_{cfl} and B_{cfl} are the upper bounds imposed by a diffusive stability criterion (cf. § 1.3.3), and read:²

$$A_{\text{cfl}} = B_{\text{cfl}} = \frac{1}{8 \Delta t} (\Delta x^{-2} + \Delta y^{-2})^{-1}$$

with time step size Δt and grid spacings $\Delta x, \Delta y$.

- A_{Munk} and B_{Munk} impose a lower bound on viscosity depending on the distance to a western boundary. The reasoning for introducing this term is that the characteristic boundary layer length scale in the Munk model is given by (1.26), i. e., $(A_H/\beta)^{1/3}$. Thus, if the chosen viscosity becomes too small, the western boundary layer will not be resolved by the model, which may lead to unphysical behavior. The parameters are defined as

$$A_{\text{Munk}}(\vec{x}) = B_{\text{Munk}}(\vec{x}) = \begin{cases} v_M \beta \Delta x^3 & \text{if } \delta(\vec{x}) \leq v_3 \Delta x \\ v_M \beta \Delta x^3 \exp(-v_2(\delta(\vec{x}) - v_3 \Delta x)) & \text{else} \end{cases}$$

with δ denoting the zonal distance to the nearest western boundary at a position \vec{x} .

- A_{SGS} and B_{SGS} are intended to represent all unresolved sub-grid scale physics. These parameters are chosen as:

$$\begin{aligned} A_{\text{SGS}} &= v_A \\ B_{\text{SGS}} &= v_B (1 + v_1(1 - \cos(2\theta'))), \end{aligned}$$

with

$$\theta' = 90^\circ \frac{\min(|\theta|, v_4)}{v_4},$$

such that $B_{\text{SGS}} = v_B$ at the equator, increasing polewards until hitting the latitude v_4 , where $B_{\text{SGS}} = (1 + 2v_1)v_B$.

Note that A_{cfl} and A_{Munk} , and thus A and B , are dependent on the grid spacings $\Delta x, \Delta y$. Hence, all parameters are fine-tuned in a heuristic manner to the resolution at hand. For an overview of the viscosity parameters v_A, v_B, v_M , and v_1 through v_4 refer to Table 2.1. The viscosity structure of the x3 default run is shown in Fig. 2.3, and that of all runs in § A.1.

| Here | Jochum et al. | CESM | Default value | |
|---------|-------------------|----------|------------------------------------|-------------------------------------|
| | | | CESM x1 | CESM x3 |
| ν_A | A_{eddy} | vconst_1 | 600 m ² s ⁻¹ | 1000 m ² s ⁻¹ |
| ν_1 | C_2 | vconst_2 | 0.5 | 24.5 |
| ν_M | unnamed | vconst_3 | 0.16 | 0.2 |
| ν_2 | unnamed | vconst_4 | 2×10^{-3} km | 10^{-3} km |
| ν_3 | unnamed | vconst_5 | 3 | 3 |
| ν_B | B_{eddy} | vconst_6 | 600 m ² s ⁻¹ | 1000 m ² s ⁻¹ |
| ν_4 | Φ_I | vconst_7 | 45° | 90° |

Table 2.1: Viscosity parameters in the parameterization used in CESM and their default values.

Part II

FRICTIONAL CONTROL OF
CROSS-EQUATORIAL FLOW

CONTENTS

| | | |
|-------|-----------------------------------|----|
| 3 | CESM Experiments | 41 |
| 3.1 | Experimental Setup | 42 |
| 3.2 | Analysis | 44 |
| 3.2.1 | Numerical Noise | 44 |
| 3.2.2 | Overall Circulation | 46 |
| 3.2.3 | AMOC | 48 |
| 3.2.4 | Indonesian Throughflow | 53 |
| 3.3 | Discussion: Godfrey's Island Rule | 58 |

CESM EXPERIMENTS

3

In order to examine the sensitivity of cross-equatorial flow on the strength of lateral friction, I have conducted a multitude of different numerical experiments using the Community Earth System Model (CESM). This chapter describes how their parameters have been modified (§ 3.1), and then summarizes the observations I have made during post-processing (§ 3.2).

It is found that while lowering viscosity may introduce a considerable amount of numerical noise (§ 3.2.1), the overall structure of the global circulation stays mostly intact, with the only difference that equatorial circulations now extend further to the East (§ 3.2.2). Lower equatorial viscosities indeed lead to a weaker overturning in the Atlantic¹ (§ 3.2.3). For extreme viscosity modifications, the structure in the equatorial layer is changed drastically, featuring strong re-circulation cells and zonal jets. These re-circulations cause a considerable fraction of water to cross the equator in the eastern part of the basin (up to half of the total transport). The Indonesian Throughflow (ITF) shows a similar signal (§ 3.2.4): Overall transports vary by about 10 %, while the structure of the flow is strongly altered. Extreme viscosity modifications cause flow in the New Guinea Coastal Undercurrent (NGCUC) to feed the ITF instead of retroflecting into the North-Equatorial Countercurrent (NECC), causing an increase of salinity in the throughflow region².

After observing that the ITF transport and especially its composition seem to depend critically on viscosity, § 3.3 reviews some implications on the applicability of the “Island Rule”. The Island Rule was introduced in Godfrey, 1989, and predicts the flow around an island based on the wind stress to its east, which is often applied to estimate the ITF. Since the Island Rule does not account for friction, the observed fluctuations of the ITF cast some doubt whether it is valid close to the equator. An extension of the Island Rule including frictional effects by Wajsowicz, (1993b) predicts a *lower* ITF transport for *higher* viscosities, in contrast to the observed behavior.

1. By $\lesssim 1.5$ Sv or about 10 %.

2. This is only the case in x_3 , while the path of the NGCUC is largely unaltered in x_1 due to a different geometry of the ITF region in this grid.

3.1 EXPERIMENTAL SETUP

Each simulation is integrated forward for 100 years until the spin-up process is largely complete and a steady circulation has been achieved. Unless specified otherwise, all further analysis is carried out on a 20-year average of the CESM output (years 80–99). All parameters not related to horizontal friction are left at their default value, apart from the fresh water restoring parameter `sfwf_weak_restore` that is set to a value of 0.55, which leads to a more realistic magnitude of the Atlantic Meridional Overturning Circulation (AMOC).

3. With friction parameterization and viscosity parameters as described in § 2.3.

The viscosity structure of the various CESM experiments³ has been altered in three different ways:

- 1) *Global scaling of the parameters;*
- 2) *Regional scaling of the parameters (i. e., only in the boundary layer, or only in the interior); and*
- 3) *Latitude-dependent scaling of the boundary layer viscosity v_M , modulated with a cosine-shape:*

$$v_M \rightarrow \begin{cases} v_M \left(1 - \cos^2\left(\frac{\pi}{2} \frac{\theta}{\theta_L}\right)\right) & \text{if } |\theta| \leq \theta_L \\ v_M & \text{else} \end{cases}$$

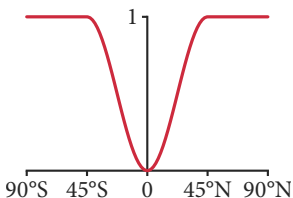


Figure 3.1: Scaling factor of the boundary layer viscosity in the cosine-banded runs.

with a parameter θ_L denoting the latitude where the Munk layer viscosity approaches its unmodified value (Fig. 3.1). The boundary layer viscosity is thus reduced to the background value at the equator in these runs.

Table 3.1 gives an overview of the CESM simulations that I have conducted. The resulting viscosity of all runs as output by CESM is shown in Appendix A.1.

Note that not all experiments are equally “interesting” — some runs, like `x3_x1visc` or `x3_lowvisc_interior` are merely included as control runs, and are omitted from parts of the evaluation to follow if they did not show any interesting dynamics. Likewise, the experiments that merely form a ramp of the parameter θ_L (i. e., `x3_lowvisc20` – `x3_lowvisc60`, and eventually `x3_nomunk`) often just show a gradual shift towards some behavior. In this case, not all of these experiments are mentioned explicitly during evaluation.

| | VISCOSITY STRUCTURE | PARAMETER | IDENTIFIER |
|----|---------------------------------------|--|--|
| x3 | default | — | x3_default |
| | cosine banded ν_M | $\begin{cases} \pm 20^\circ \text{ lat.} \\ \pm 30^\circ \text{ lat.} \\ \pm 45^\circ \text{ lat.} \\ \pm 60^\circ \text{ lat.} \end{cases}$ | x3_lowvisc20 x3_lowvisc30 x3_lowvisc45 x3_lowvisc60 |
| | no Munk layer ($\nu_M = 0$) | — | x3_nomunk |
| | linearly scaled ν_A, ν_B, ν_M | $\begin{cases} 0.1 \\ 4 (\nu_A, \nu_B), 2 (\nu_M) \end{cases}$ | x3_lowvisc_global x3_hivisc |
| | linearly scaled ν_A, ν_B | 0.1 | x3_lowvisc_interior |
| | all as in x1_default | — | x3_x1visc |
| x1 | default | — | x1_default |
| | linearly scaled ν_M | $\begin{cases} 0.5 \\ 0.1 \end{cases}$ | x1_halfmunk x1_tenthmunk |

Table 3.1: CESM run overview. Runs are grouped by resolution, structure of viscosity modification, and extent of modification (“parameter”).

3.2 ANALYSIS

3.2.1 Numerical Noise

4. This is the case for:

```
x3_lowvisc20
x3_lowvisc30
x3_lowvisc45
x3_lowvisc60
x3_nomunk
x3_lowvisc_global
x3_x1visc
x1_halfmunk
x1_tenthmunk
```

By lowering the Munk layer viscosity parameter ν_M in most runs⁴, small-scale noise is introduced into the solution that may become dominant in some simulations (Fig. 3.2). Since this noise is effectively removed by applying a simple boxcar filter in zonal direction, I conclude that it is indeed acting on grid scale, and thus identify it with numerical (dispersive) noise (see also § 1.3.4).

The generation of excessive numerical noise in the equatorial band is understandable when looking at the grid Reynolds numbers in this region. Bryan, Manabe, and Pacanowski, (1975) give a condition of

$$\text{Re} \lesssim 2, \quad (3.1)$$

“so that noise advected into a grid cell is effectively diffused” (Jochum et al., 2008). A general formulation of the Reynolds number reads

$$\text{Re} = \frac{UL}{A_H},$$

with typical velocity and length scales U and L , and viscosity A_H . Since numerical noise is created at grid scale, I approximate the Reynolds number for this noise as

$$\text{Re}_n = \frac{\max(u \Delta x, v \Delta y)}{B}.$$

Calculating Re_n shows that (3.1) is generally fulfilled in the western boundary regions in `x3_default`, but not in, e.g., `x3_lowvisc60` (Fig. 3.3). Instabilities that are created in the eastern parts of the equatorial regions, which are then advected westwards by Rossby waves, can thus not be diffused effectively, and the observed oscillatory patterns emerge as shown in Fig. 3.2.

5. Recall that $\vec{\mathcal{F}} \sim A_H \nabla^2 \vec{u}$, hence large oscillations as seen in Fig. 3.2 may cause $\nabla^2 u$ to negate the effect of a smaller viscosity A_H , and lead to a locally larger friction term.

Since grid-scale noise may not only lead to an inaccurate solution, but also cause *more* effective friction for *lower* viscosities⁵, results for particularly noisy runs should generally be interpreted with care. However, after comparing the smoothed velocity field of a low-viscosity run to `x3_default` (Fig. 3.2), it seems that the smoothed solution is still a reasonable representation of the real dynamics.

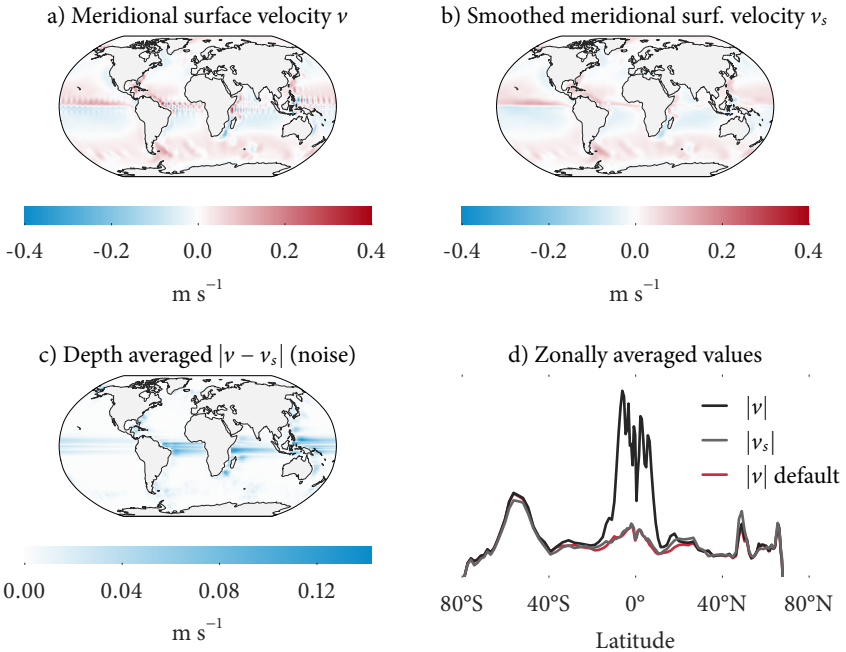


Figure 3.2: By lowering equatorial viscosities, the solution becomes dominated by numerical noise. Shown here: data from `x3_lowvisc60`. The oscillating pattern in (a) can effectively be removed by smoothing with a triangular filter in zonal direction (b). The difference between the original and grid-level smooth fields is then identified as noise (c). Noise is preferably created in zonal direction, since $\Delta x > \Delta y$ at the equator. Although noise actually dominates the solution in the equatorial band in `x3_lowvisc60`, the smoothed field is still a decent representation of the real dynamics (d).

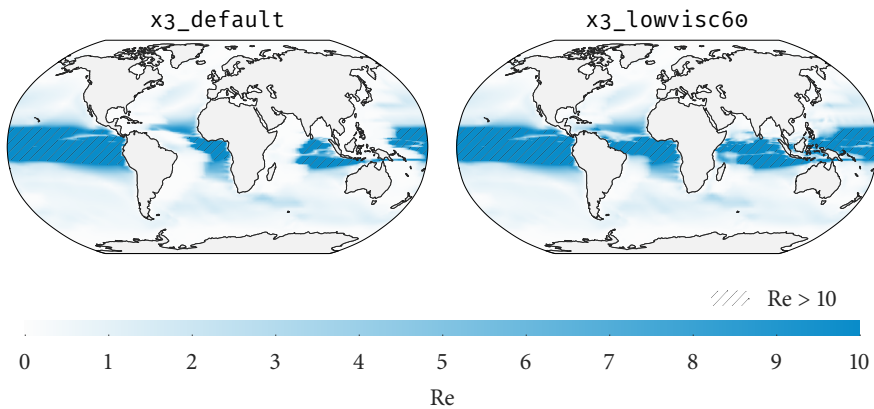


Figure 3.3: Lowering the Munk layer viscosity parameter leads to infeasibly high grid-scale Reynolds numbers in the equatorial boundary layers.

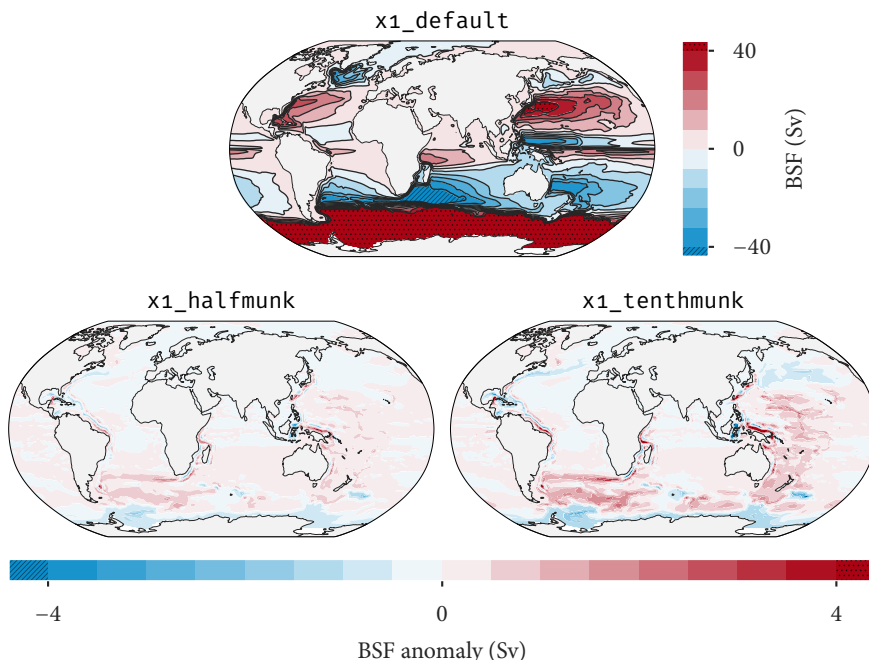
3.2.2 Overall Circulation

The large-scale, vertically integrated circulation as given by the barotropic stream function (BSF) seems largely unaffected by viscosity modifications. However, in the equatorial regions, it shows some interesting features (Fig. 3.5). The NECC gets considerably stronger in all oceans, and reaches much further east in the Atlantic and Indian oceans, to the point that an eastern boundary current begins to form. In the Indopacific region, the total magnitude of the South-Equatorial Current (SEC) and North-Equatorial Current (NEC) transports increase by at least 6 Sv each. An increase in total transport is also observed in the North Atlantic circulation.

Thus, it seems that local viscosity changes in the equatorial region indeed have mostly local effects. The regions affected most are the equatorial Atlantic and Indopacific. Hence, these two regions are examined in detail during the following sections.

In contrast to the behavior observed in the x_3 runs, viscosity modifications on the x_1 grid barely seem to have any effect on the global circulation patterns (Fig. 3.4). The largest changes are found around Indonesia, and along boundary currents (such as the Kuroshio, the Gulf Stream, and the Agulhas Current). A more localized analysis is required in order to detect subtle changes in the circulation.

Figure 3.4: Using the x_1 -grid, the global circulation patterns seem mostly unaffected by viscosity modification. Top: BSF in x_1 _default. Bottom: BSF difference compared to x_1 _default. Note the very different color scales.



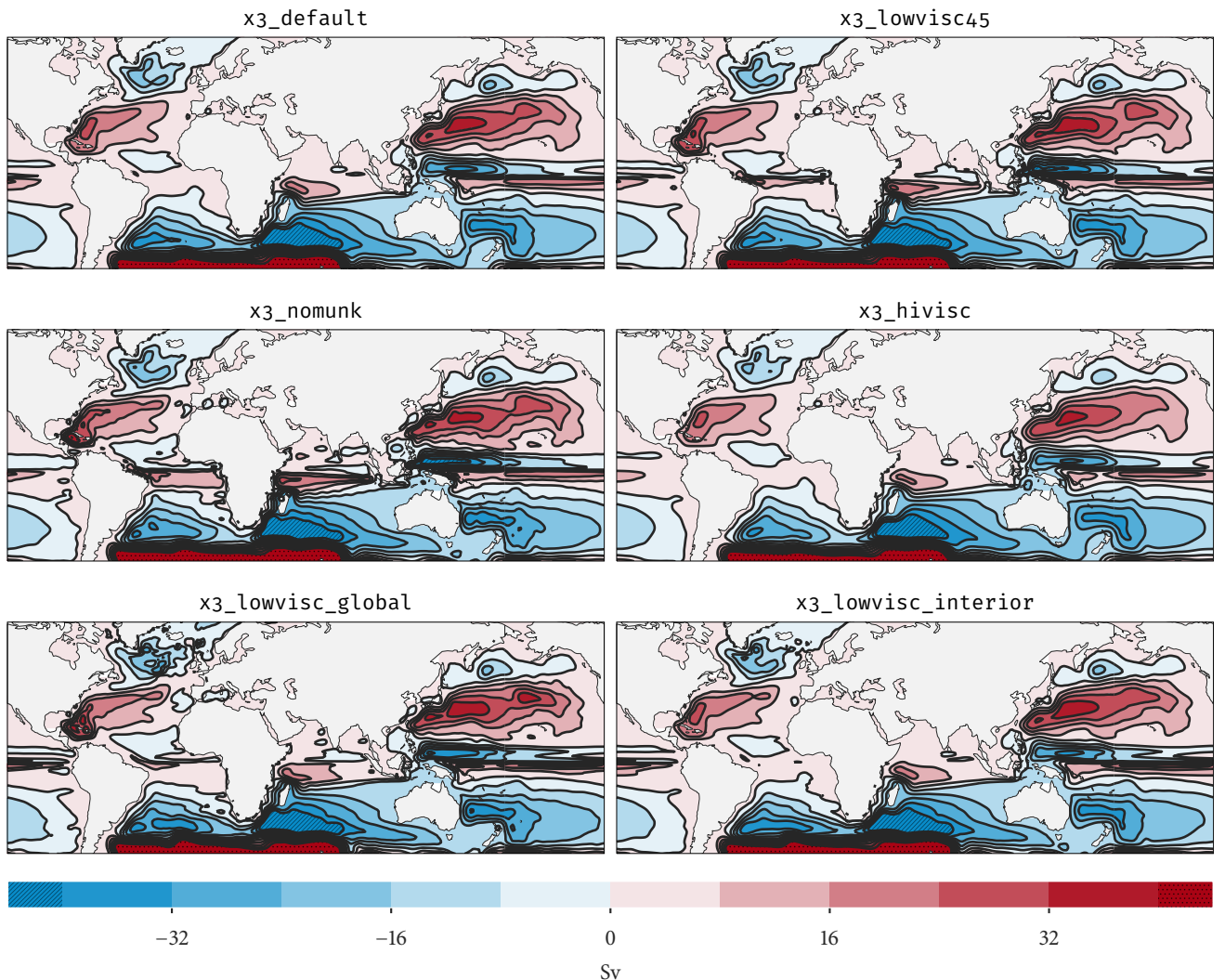


Figure 3.5: By reducing the equatorial Munk layer viscosity, the equatorial circulation extends all the way to the eastern boundary. Shown are contours of the BSF and the associated transport in Sv .

3.2.3 AMOC

| | |
|---------------------|------|
| x3_lowvisc20 | 0.0 |
| x3_lowvisc30 | 0.0 |
| x3_lowvisc45 | -0.5 |
| x3_lowvisc60 | -1.0 |
| x3_nomunk | -1.5 |
| x3_lowvisc_global | -1.0 |
| x3_lowvisc_interior | 0.0 |
| x3_x1visc | -0.5 |
| x3_hivisc | 0.5 |
| x1_halfmunk | -0.5 |
| x1_tenthmunk | -0.5 |

Table 3.2: Change of Atlantic cross-equatorial transport (in Sverdrup) in CESM experiments compared to their respective default. Rough estimates from deeply penetrating streamlines in the vertical stream function (Fig. 3.5). Uncertainties are of the order ± 0.5 Sv.

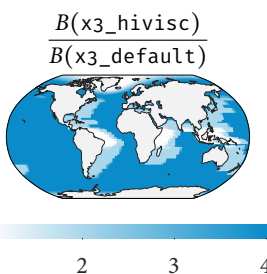


Figure 3.6: Viscosity of $x3_hivisc$, relative to $x3_default$.

Conveniently, the vertical stream function of the AMOC Ψ_A is written by CESM in every time step as a diagnostic. This variable gives the meridional overturning transport in a depth-latitude slice (such that $(\Psi_A)_z = -V$, $(\Psi_A)_y = W$ with zonally integrated velocities V , W). For a circulation like the AMOC where poleward and equator-ward flow are clearly separated in depth through the formation of North Atlantic Deep Water (NADW), this is a very useful diagnostic, since it allows us to quantify the total cross-equatorial transport in the Atlantic at a glance.

The vertical stream function reveals a weakening of the cross-equatorial transport in the runs with extreme viscosity reductions by about 1.5 Sv, and changes of about ± 0.5 Sv in the runs with moderate viscosity modifications (Table 3.2, Fig. 3.7).

As it turns out, quite drastic viscosity changes are necessary for influencing the observed cross-equatorial transport in the Atlantic. Neither $x3_lowvisc20$, $x3_lowvisc30$, nor $x3_lowvisc_interior$ show a clear signal of at least ± 0.5 Sv. Another simulation of particular interest is $x3_hivisc$, whose viscosity is unaltered in the equatorial Munk layer due to the CFL constraint (cf. § 1.3.3), but doubled at higher latitudes, and quadrupled in the interior (Fig. 3.6). Even though the equatorial boundary layer viscosity is unchanged, an increase of cross-equatorial transport is observed, which is of a similar magnitude as the observed decrease in e.g. $x3_lowvisc45$. Thus, it seems that changing the Munk layer viscosity right at the equator is not the only way to influence cross-equatorial transport.

While cross-equatorial transport anomalies are quite small ($\lesssim 10\%$) compared to the extreme viscosity modifications (several orders of magnitude), there clearly is a distinct correlation between viscosity and cross-equatorial transport, since lower viscosities always lead to lower measured transports and vice versa. This implies three possible explanations for the observed behavior:

- 1) *Viscosity modifications leave the Munk layer transport largely unchanged, but influence the cross-equatorial flow in the interior (as found in Killworth, 1991);*
- 2) *Some higher-order effect (caused e.g. by topography or nonlinearity) that depends on viscosity alters the efficiency of vorticity transformation in the western boundary layer; or*
- 3) *Modifications at higher latitudes (as e.g. in $x3_lowvisc45$, $x3_lowvisc60$, $x3_nomunk$, $x3_lowvisc_global$, $x3_hivisc$, and the $x1$ experiments) influence the actual forcing of the AMOC, e.g. the creation of NADW or upwelling in the Atlantic.*

In order to test the plausibility of each of these explanations, I had a closer look at some additional diagnostics. One interesting variable is the actual flow field

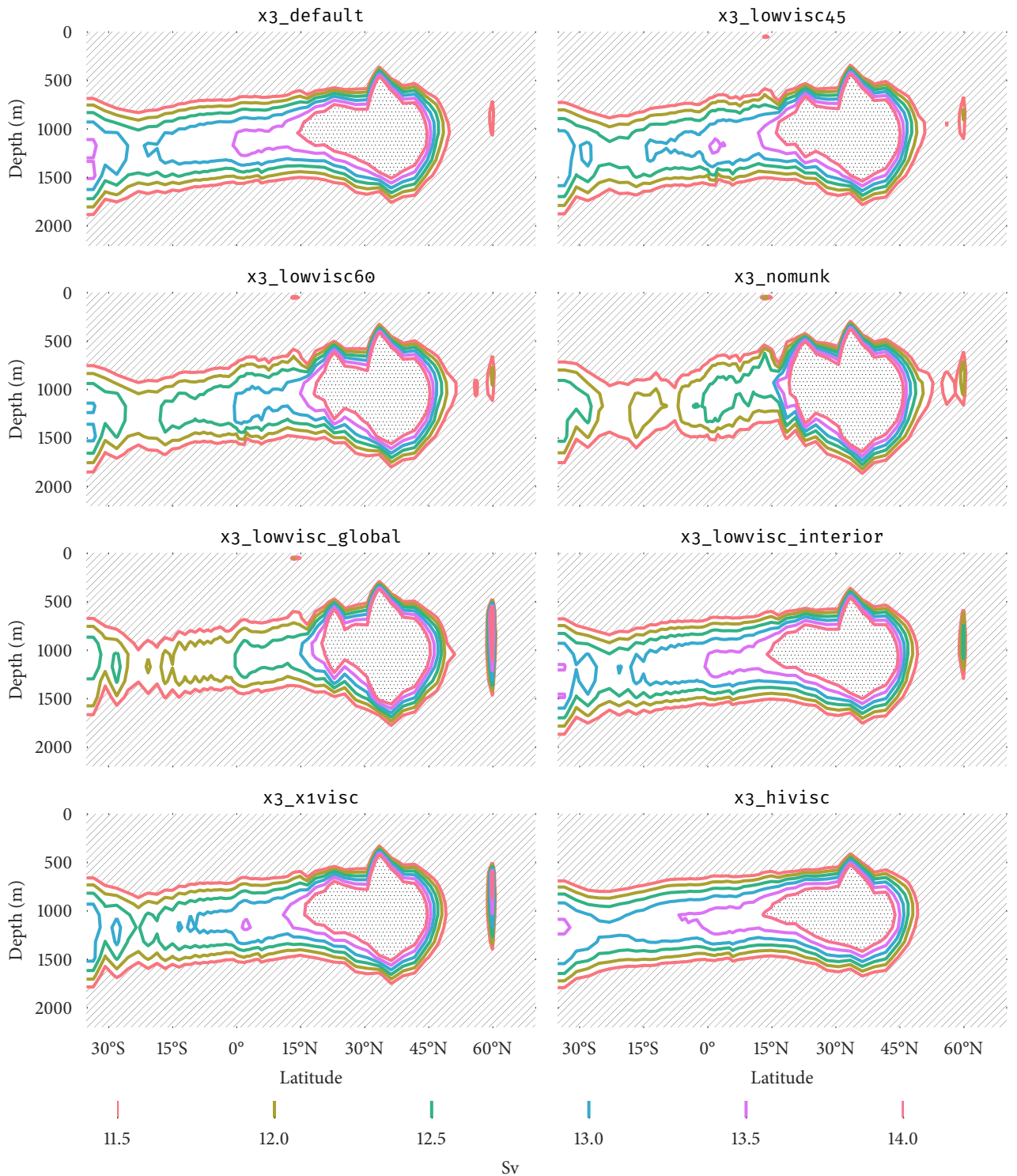


Figure 3.7: Changing the viscosity structure may change the AMOC by up to 1.5 Sv (~ 10 %). Shown are equator-crossing contours of the vertical AMOC stream function. Stream lines below 11.5 Sv (hatched) and above 14 Sv (dotted) are omitted.

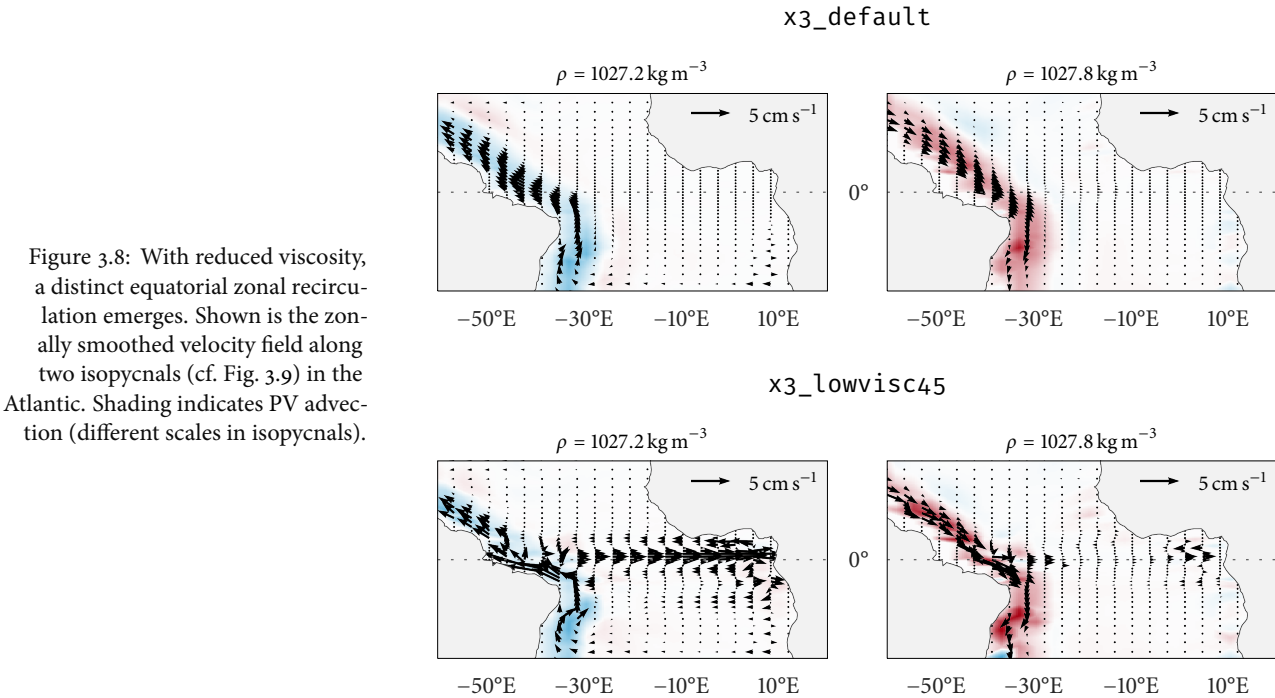


Figure 3.8: With reduced viscosity, a distinct equatorial zonal recirculation emerges. Shown is the zonally smoothed velocity field along two isopycnals (cf. Fig. 3.9) in the Atlantic. Shading indicates PV advection (different scales in isopycnals).

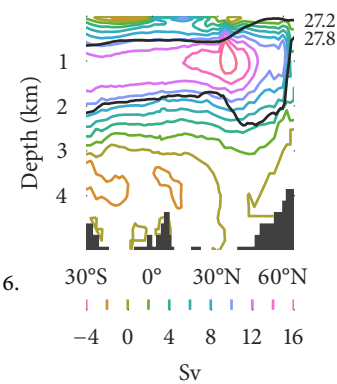


Figure 3.9: Zonally averaged depth of one isopycnal in the upper ($\sigma_{27.2}$) and one in the lower ($\sigma_{27.8}$) branch of the AMOC.

inside equator-crossing isopycnals. Since, in an approximately adiabatic ocean, deep flow is confined to isopycnals, this is a convenient way to visualize the flow field in two dimensions. Also, if the adiabatic assumption holds, PV can only be modified by friction along stream lines. Thus, the advection of PV, $\vec{u} \cdot \nabla \Pi$, may give valuable insights on the regions of high PV transformation through friction. By choosing two specific isopycnals, one located in the upper branch and one in the lower branch of the AMOC (Fig. 3.9), the structure of the flow and the PV transformation in each branch can be examined (Fig. 3.8). As it turns out, lowering the equatorial Munk layer viscosity creates large zonal circulations in an equatorial band that extend all the way to the eastern boundary⁶, as already seen in the global BSF (§ 3.2.2). In the interior, those circulations conserve PV, but some modification takes place at the eastern boundary, especially in the upper isopycnal.

Since it is still unclear where exactly water crosses the equator and where the largest modification takes place, I have integrated the meridional transport at the equator in the Atlantic in some slices (western boundary and interior, for each upper and lower isopycnal) for all experiments (Table 3.3). This data shows several interesting signals:

- ▶ The total cross-equatorial transport across all experiments varies between -0.7 Sv and -1.3 Sv, i. e., a non-constant net transport from the northern to the southern hemisphere. Since the atmospheric forcing is static in all

experiments, this anomaly might indicate that the simulations are still not entirely spun-up after the 100 y integration period⁷.

- ▶ The violent re-circulations cause a significant increase of both boundary layer and interior transports in the upper layer in low-viscosity runs (water that crosses the equator in the boundary layer and immediately re-enters the southern hemisphere through the interior), which does not necessarily cause an increase in total transport (see e.g. `x3_lowvisc20`).
- ▶ In the lower layer, the re-circulation is far less pronounced, so the kinematic effect of a lower viscosity can be observed directly. Western boundary layer transports decrease greatly with lower viscosities (-15 Sv in the control vs. -6.7 Sv in `x3_nomunk`), which is only partly compensated by a higher flow in the interior.
- ▶ In the `x1` runs, the total transport is stable at -0.7 Sv. Changes in both upper layer and lower layer transports are pretty much entirely contained in the western boundary layer.
- ▶ The change in total transport compared to the control gives the same trend, but is generally smaller than that estimated from the vertical stream function (as in Table 3.2)⁸.

⁷ This might however also be caused by numerical inaccuracies when integrating over the basin.

⁸ However, this is well contained within the margin of error that is introduced when simply counting equator-crossing streamlines.



I thus conclude that a lower viscosity indeed heavily modifies the PV transformation in the western boundary layer, up to the point that equal amounts of water cross the equator in the western and eastern parts of the basin (`x3_nomunk`), while other possible effects only seem to play a minor role.

| Run | Total | Upper layer (Sv) | | | Lower layer (Sv) | | |
|---------------------|----------|------------------|------|-------|------------------|-------|------|
| | Σ | Σ | W | I | Σ | W | I |
| x3_default | -1.0 | 12.6 | 17.8 | -5.2 | -13.6 | -15.0 | 1.4 |
| x3_lowvisc20 | -1.0 | 12.6 | 25.6 | -13.0 | -13.6 | -10.4 | -3.2 |
| x3_lowvisc30 | -1.0 | 12.5 | 28.7 | -16.2 | -13.6 | -8.8 | -4.8 |
| x3_lowvisc45 | -1.1 | 12.3 | 31.6 | -19.3 | -13.3 | -8.0 | -5.3 |
| x3_lowvisc60 | -1.1 | 12.0 | 32.6 | -20.7 | -13.1 | -7.6 | -5.4 |
| x3_nomunk | -1.1 | 11.4 | 31.8 | -20.3 | -12.6 | -6.7 | -5.8 |
| x3_lowvisc_global | -1.3 | 11.3 | 21.6 | -10.3 | -12.5 | -13.9 | 1.4 |
| x3_lowvisc_interior | -1.1 | 12.5 | 17.7 | -5.2 | -13.6 | -14.8 | 1.2 |
| x3_x1visc | -1.2 | 12.2 | 15.4 | -3.3 | -13.3 | -14.2 | 0.8 |
| x3_hivisc | -0.8 | 12.8 | 17.9 | -5.2 | -13.6 | -16.3 | 2.7 |
| x1_default | -0.7 | 12.1 | 17.7 | -5.6 | -12.9 | -13.5 | 0.6 |
| x1_halfmunk | -0.7 | 11.9 | 17.4 | -5.5 | -12.7 | -13.2 | 0.6 |
| x1_tenthmunk | -0.7 | 11.9 | 17.4 | -5.5 | -12.6 | -13.2 | 0.6 |

Table 3.3: Cross-equatorial transport in the AMOC. Σ , W, I denote transport in the whole layer, in the western boundary, and the interior, respectively. Dividing line between upper and lower layer at 1200 m depth, and between east and west at -25°E .

3.2.4 Indonesian Throughflow

The influence of a modified equatorial viscosity on the ITF is remarkably different from that on the AMOC.

The total transport from the Northern Pacific into the Indian Ocean shows a similar pattern under viscosity modification as the AMOC (Table 3.4). Jochum et al., (2009) found that, under an increase of boundary layer viscosity by a factor of 10 in a General Circulation Model (GCM), “Makassar Strait transport increases from 6.4 to 7.2 Sv and the Torres Strait transport decreases from 1.6 to 1.2 Sv”, i. e., a response of similar magnitude as in e. g. `x1_tenthmunk`.

However, the origin of the water in the ITF varies greatly between `x3` runs (Fig. 3.10). For viscosities lower than the default, instead of turning eastward and feeding the NECC, more and more streamlines originating from the SEC, i. e., the South Pacific (approaching the equator in the NGCUC), curve back into the ITF and thus remain in the southern hemisphere, closely following the topography of West Papua. Accounting only for flow in the ITF whose stream function contours originate in the northern hemisphere (i. e., in the Mindanao Current), drastic changes with viscosity become apparent (Table 3.5).

Since the BSF is merely a depth-integrated stream function, important features of the ITF, such as different currents crossing each others paths in depth, might be hidden in this diagnostic. In order to get an idea of the structure of the ITF in depth, we can use the fact that the ocean pathways between Borneo in the west and New Guinea in the east are very narrow in CESM, especially so in the `x3` grid (one active grid point; see Fig. 3.13). The whole ITF can thus be analyzed just by considering a slice of the ocean at approximately 1.5°S latitude and between 115°E and 135°E longitude (solid line in Fig. 3.13). The meridional velocity v in this slice shows that most of the transport in the ITF occurs in near-surface flow $\lesssim 200$ m, with a minimum at about 400 m, and a slightly increasing transport towards the bottom of the ocean (Fig. 3.11). With modified viscosity, most of the changes in total transport are carried by the upper part of the domain (Table 3.6).

| | |
|----------------------------------|------|
| <code>x3_lowvisc20</code> | -0.5 |
| <code>x3_lowvisc30</code> | -0.5 |
| <code>x3_lowvisc45</code> | -0.5 |
| <code>x3_lowvisc60</code> | -1.0 |
| <code>x3_nomunk</code> | -1.5 |
| <code>x3_lowvisc_global</code> | -1.0 |
| <code>x3_lowvisc_interior</code> | -0.5 |
| <code>x3_x1visc</code> | -1.0 |
| <code>x3_hivisc</code> | 1.5 |
| <code>x1_halfmunk</code> | -0.3 |
| <code>x1_tenthmunk</code> | -0.5 |

Table 3.4: Change of ITF transport (in Sverdrup) in CESM experiments compared to their respective default.

| | |
|----------------------------------|------|
| <code>x3_lowvisc20</code> | -0.5 |
| <code>x3_lowvisc30</code> | -2.5 |
| <code>x3_lowvisc45</code> | -4.5 |
| <code>x3_lowvisc60</code> | -7.0 |
| <code>x3_nomunk</code> | -7.0 |
| <code>x3_lowvisc_global</code> | -1.5 |
| <code>x3_lowvisc_interior</code> | -0.5 |
| <code>x3_x1visc</code> | -1.0 |
| <code>x3_hivisc</code> | 2.0 |
| <code>x1_halfmunk</code> | -0.5 |
| <code>x1_tenthmunk</code> | -0.5 |

Table 3.5: Change of ITF transport originating in the northern hemisphere.

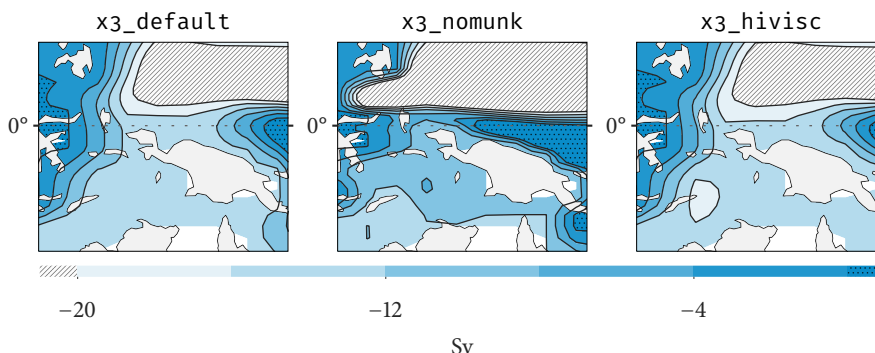


Figure 3.10: Changing the viscosity structure drastically changes the structure of the Indonesian Throughflow. Shown are contours of the horizontal barotropic stream function of the MC, the NGCUC, the SEC, the NECC, and the ITF. The Makassar and Lombok straits are closed in the `x3`-grid.

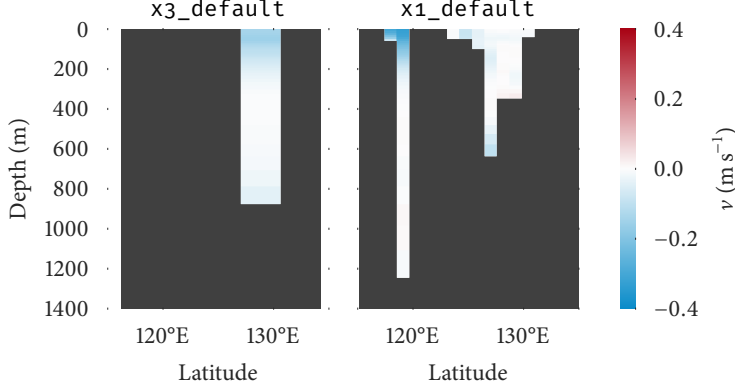


Figure 3.11: Most of the ITF transport is carried by the upper 200 m of the ocean. In the x_1 -grid, where both Makassar strait and Lifamatola passage are open, most of the transport occurs in the Makassar strait, like in the real ocean. Shown is meridional velocity v in the slice marked in Fig. 3.13 for the default runs. Boundary cells marked in gray.

Table 3.6: Transport changes in the ITF occur mainly in the upper layer. Total transports are generally in agreement with the transport suggested by the BSF. Values obtained by directly integrating v over the Makassar and Lifamatola passages at 1.5°S (cf. Fig. 3.13, Fig. 3.11). The dividing line between upper and lower layer was put into the transport minimum at about 400 m depth.

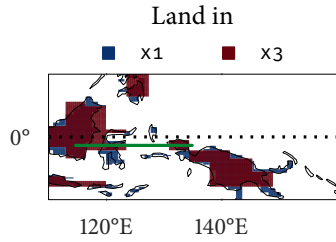


Figure 3.13: Geometry of the ITF in CESM. The ITF consist of only one active velocity grid point in x_3 . In x_1 , both Makassar strait and Lifamatola passage are open. The green line at 1.5°S marks the slice where the ITF transport is analyzed.

| Run | ITF transport (Sv) | | |
|--------------------------|--------------------|-------|-------|
| | total | upper | lower |
| $x_3_default_lowsfwf$ | -13.1 | -9.9 | -3.2 |
| $x_3_lowvisc20$ | -12.4 | -8.5 | -3.9 |
| $x_3_lowvisc30$ | -12.3 | -8.3 | -4.0 |
| $x_3_lowvisc45$ | -11.9 | -8.0 | -3.9 |
| $x_3_lowvisc60$ | -11.5 | -7.8 | -3.7 |
| x_3_nomunk | -10.7 | -7.6 | -3.1 |
| $x_3_lowvisc_global$ | -11.5 | -8.5 | -3.0 |
| $x_3_lowvisc_interior$ | -12.7 | -9.7 | -3.0 |
| $x_3_x1visc_lowsfwf$ | -12.2 | -9.3 | -2.9 |
| x_3_hivisc | -15.0 | -11.2 | -3.8 |
| $x_1_default_lowsfwf$ | -10.6 | -9.2 | -1.4 |
| $x_1_halfmunk$ | -10.3 | -9.0 | -1.4 |
| $x_1_tenthmunk$ | -10.3 | -8.9 | -1.4 |

Looking at the actual flow field along two isopycnals, one representative for the near-surface flow, and one for the deep circulation, reveals that the near-surface flow in the NGCUC definitely retroflects into the NECC in $x_3_default$, while the exact path is somewhat unclear in $x_3_lowvisc45$ (Fig. 3.12). The decreased viscosity leads to the creation of a large number of eddies along the NECC. Of particular interest is the strong eddy right at the retroflexion region of the Mindanao current. A similar feature is also present in the real ocean, called the Halmahera eddy. Due to this eddy, it is not quite evident whether the water coming from the NGCUC actually enters the ITF or gets mostly retroflected into the NECC. Wajsowicz, (1993a) in fact discusses the influence of the Halmahera eddy on the composition of the ITF, and finds that the presence of this eddy causes more water from the southern hemisphere to retroreflect into the NECC, which also seems to be the case here. The deep branch of the NGCUC seems to always feed the ITF, although the velocity field

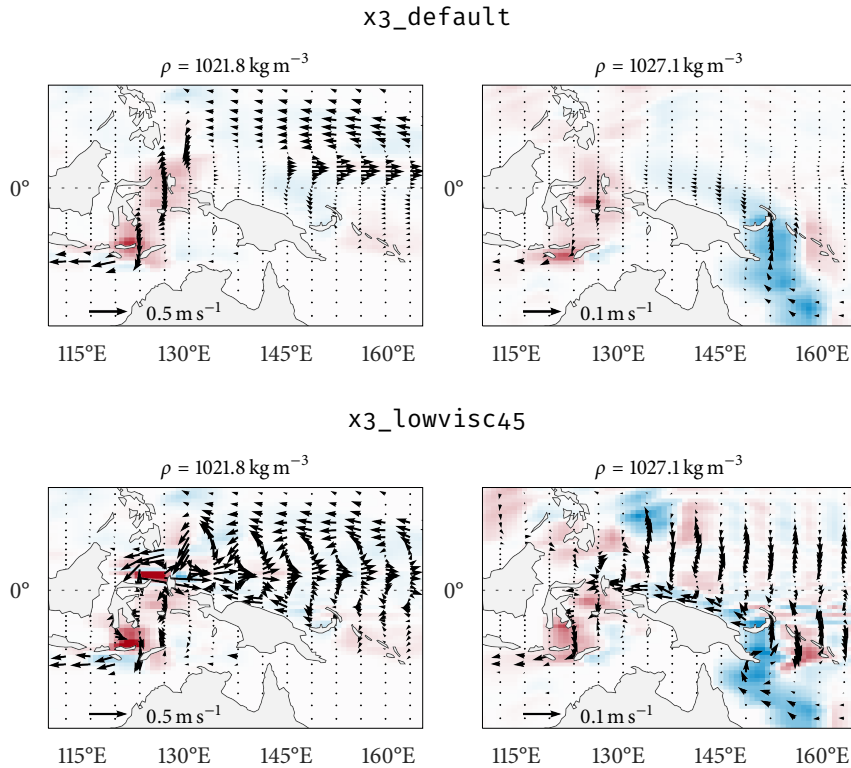


Figure 3.12: The velocity field along two isopycnals corresponding to the maximum flow of the upper and lower branch of the ITF reveals that the deep New Guinea current completely enters the ITF, while only the lighter water from the SEC is retroflected into the NECC. Shading indicates PV advection (different scales in isopycnals).

becomes quite noisy at this depth. This noise might also be the cause of the observed fluctuations of the deep layer transport (Table 3.6).

In order to get a clearer picture which hemisphere the water in the ITF originates in, I had a closer look at the salinity and temperature profiles of the ITF. Since water coming from the SEC in the southern hemisphere is significantly saltier than water in the MC, the ITF is expected to become saltier as southern water enters it via the NGCUC (Fig. 3.14). Indeed, the stronger the viscosity reduction, the saltier (Fig. 3.15) and warmer (Table 3.7) the ITF becomes. I thus conclude that, for low viscosities, water from the NGCUC indeed fails to cross the equator into the northern hemisphere, and instead curves back through the ITF into the southern hemisphere. Salinity and temperature changes occur both in the upper and lower branch of the ITF, so even though there is no significant change in net transport in deeper layers, the composition of the deeper water is definitely affected by viscosity modifications.

We may thus conclude that, considering that the total transport in the ITF is about 13 Sv, altering nothing but viscosity may cause the ITF to either be fed entirely by the Mindanao current (x3_hivisc), or by Mindanao and New Guinea currents at roughly equal parts (x3_nomunk). *Hence, in this region, PV transformation through friction seems to play a crucial role, and the solution is definitely somewhat sensitive to the chosen viscosity when a realistic overturning is desired.*

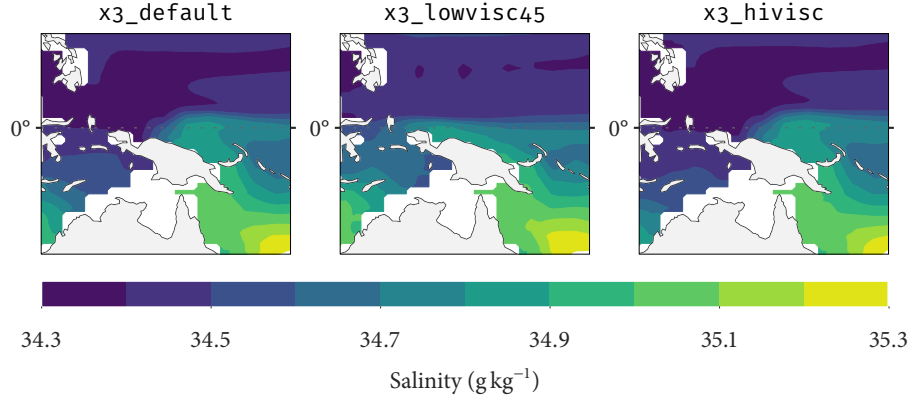


Figure 3.14: Lowering viscosity allows saline waters to reach further westward. Shown is salinity at 100 m depth in the ITF.

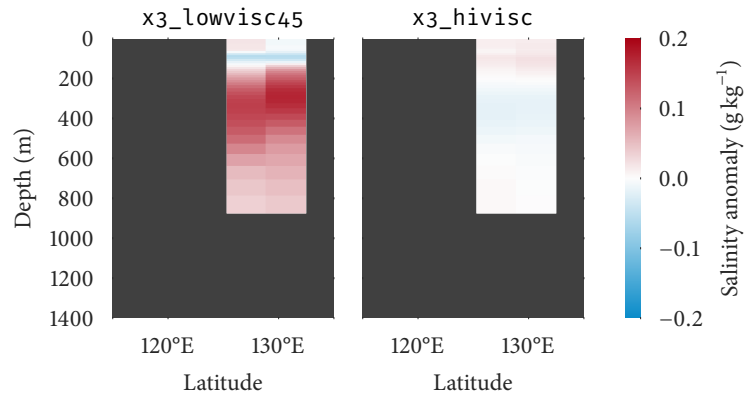


Figure 3.15: Lowering viscosity leads to a measurably saltier ITF.

Shown is salinity anomaly in the ITF relative to $x3_default$.

| Run | Mean temperature ($^{\circ}\text{C}$) | | |
|-------------------------|---|-------|-------|
| | whole | upper | lower |
| $x3_default_lowsfwf$ | 12.0 | 17.9 | 6.7 |
| $x3_lowvisc20$ | 12.1 | 17.9 | 6.9 |
| $x3_lowvisc30$ | 12.2 | 18.0 | 7.0 |
| $x3_lowvisc45$ | 12.3 | 18.1 | 7.1 |
| $x3_lowvisc60$ | 12.4 | 18.1 | 7.2 |
| $x3_nomunk$ | 12.6 | 18.2 | 7.5 |
| $x3_lowvisc_global$ | 12.1 | 17.9 | 6.9 |
| $x3_lowvisc_interior$ | 12.0 | 17.9 | 6.7 |
| $x3_x1visc_lowsfwf$ | 12.0 | 17.9 | 6.7 |
| $x3_hivisc$ | 11.8 | 17.7 | 6.5 |
| $x1_default_lowsfwf$ | 15.4 | 20.3 | 5.4 |
| $x1_halfmunk$ | 15.5 | 20.3 | 5.4 |
| $x1_tenthmunk$ | 15.5 | 20.4 | 5.5 |

Table 3.7: Reducing viscosity mostly leads to a warmer lower branch of the ITF. As Table 3.6, but for mean temperature.

On the other hand, this sensitivity of the ITF composition on the viscosity structure is altered in the x_1 runs, where a different response is observed (Fig. 3.16). Because of additional islands that are not present in the x_3 grid (such as North Maluku off the north-western tip of West Papua), and due to the fact that the Torres strait is closed in the x_1 grid (Meehl et al., 2012), water crossing the equator in the New Guinea current would be required to travel farther northward in order to join the ITF. This imposes a stronger constraint on the PV transformation inside the current, which causes nearly all of the New Guinea current to be retroflected into the NECC. Also, a reduced grid spacing and overall lower viscosities, as in x_1 , allow for increased eddy formation, i. e., a stronger Halmahera eddy and thus a more pronounced ITF originating in the North Pacific (Wajsowicz, 1993b).



Observations suggest a total southward transport of the ITF of 15 Sv (uncertainty: 10.7 to 18.7 Sv, Sprintall et al., 2009). Aken, Brodjonegoro, and Jaya, 2009 give a mean southward transport of 2.5 Sv through the Lifamatola passage below 1250 m, and a northward transport of 0.9 to 1.3 Sv above that. However, these figures are impossible to compare to the x_3 model throughflow, since the geometry of the ITF region is completely different from the real geometry (recall that the Makassar strait is closed in x_3 , and that the Lifamatola passage is much shallower). The total ITF transport is modeled quite well in x_3 , where higher viscosities lead to a transport that is closer to the observed mean. Also, several studies such as Gordon, 1986 and Lukas, Yamagata, and McCreary, 1996 imply that the origin of the ITF lies indeed in the northern hemisphere in the real ocean. Thus, lower viscosities *do not lead to a more realistic ITF* in x_3 .

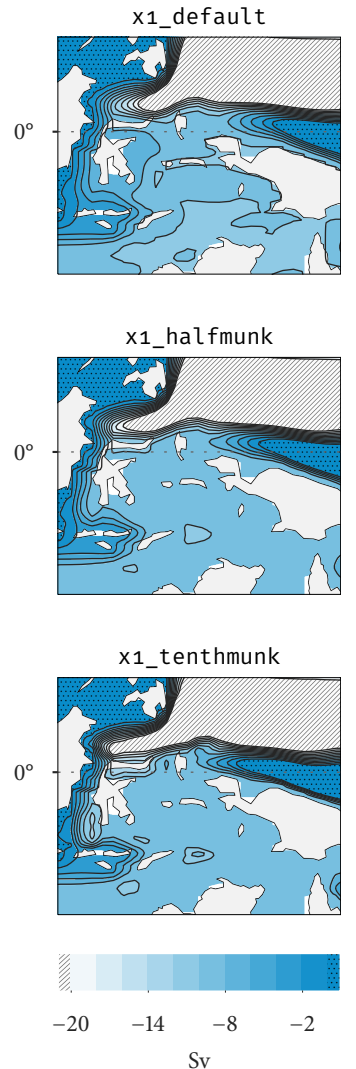


Figure 3.16: Changing the viscosity structure drastically changes the structure of the Indonesian Throughflow. Shown are BSF contours in the ITF region.

3.3 DISCUSSION: GODFREY'S ISLAND RULE

In 1989, JS Godfrey proposed a very powerful, semi-heuristic rule, the “Island Rule” (Godfrey, 1989). It is used to calculate the total transport T_0 around an island such as e. g. New Zealand, and reads:

THE ISLAND RULE

$$T_0 = (\rho_0 (f(Q) - f(T)))^{-1} \oint_{\overline{\text{TSRQ}}} \tau \, dl \quad (3.2)$$

9. This of course stems from the assumption that the interior ocean is in a pure Sverdrup balance, which promotes wind stress as the only decisive parameter for the ensuing circulation.

10. Consisting of Australia, New Zealand, New Guinea, and some neighboring, minor islands.

where τ denotes the surface wind stress, ρ_0 the water density (assumed constant), and $f(l)$ the Coriolis frequency at a location l . The integration path $\overline{\text{TSRQ}}$ starts at the southern tip of the island and follows the western shore to its northern tip, then turns eastward all the way to the nearest continental boundary, from where it returns to the southern tip to the island (Fig. 3.17). The circulation around an island can thus be calculated from wind forcing alone⁹, which is a powerful result, since wind stress data is widely available.

Treating Australasia¹⁰ as a single island, the Island Rule can even be used to compute an estimate of the ITF. — doing so yields a very realistic magnitude of (16 ± 4) Sv (after Godfrey, 1989).

However, the Island Rule implies that the ITF is fed entirely by *southern* water, which contradicts observations (cf. § 3.2.4). Godfrey addresses this in Godfrey, Wilkin, and Hirst, 1993, proposing the solution that water from the southern hemisphere retroflects into the NECC (as seen in the CESM experiments), then joins the NEC after some time, and ultimately feeds the ITF via the MC. However, it is still unclear whether this interpretation of the real events holds up.

One further contradiction with the Island Rule is given in Jochum et al., 2009, where it is shown that the total transport in the ITF decreases when the tip of

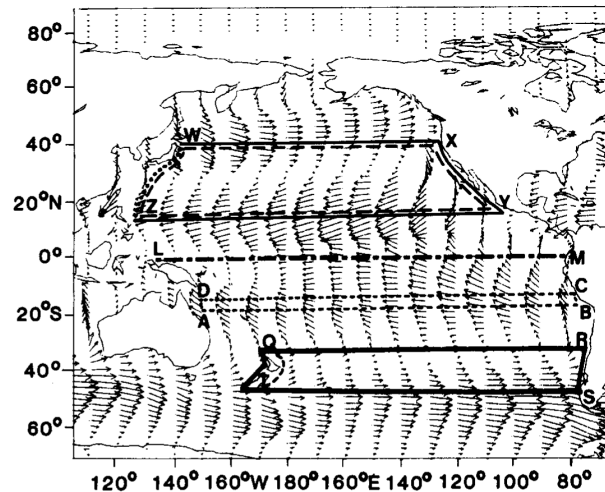


Figure 3.17: The integration path $\overline{\text{TSRQ}}$ as used in the Island Rule (3.2) for New Zealand. From Godfrey, 1989.

New Guinea is removed, even though the Island Rule predicts an *increased* transport due to a changed wind stress at the northern edge of its integration part¹¹.

All of the previously discussed weak points of the Island Rule come from the same apparent contradiction: *How can the ITF only depend on the atmospheric forcing without taking any kinematic effects into account?* If the Island Rule were strictly valid for the ITF, there would be no dependence of the throughflow magnitude on viscosity whatsoever¹² — however, in models, at least a slight dependence is observed (see § 3.2.4 and e. g. Jochum et al., 2009).

Godfrey already stated in his introductory paper on the Island Rule (Godfrey, 1989):

“However, the result does depend critically on the assumption that all vorticity entering the western boundary is immediately dissipated, at the latitude where it is created.”

For no-slip boundary conditions in a western boundary layer with an interior ocean in Sverdrup balance, Pedlosky states in *Ocean Circulation Theory* (Pedlosky, 1996):

“[...] in the steady state the vorticity put into the latitude strip (Y_1, Y_2) by the wind must be locally dissipated in the same latitude band by a horizontal flux of vorticity out of the basin in that same strip.”

However, near the equator, there is no “Sverdrup interior” that matches the boundary solution, and nonlinearities become important, so this assumption does not necessarily hold for the ITF. It is thus indeed questionable whether the Island Rule may be trusted close to the equator.



Wajsowicz, (1993b) proposes an extension of the Island Rule for the ITF that takes friction and topography into account, and finds an ITF transport that is *reduced* by about 2 Sv. Wajsowicz’s model predicts a transport that is generally lower for larger boundary layer widths δ_M (and thus higher viscosities), in contrast to what is found in CESM (higher ITF transport for higher viscosity). The theoretical response described by Wajsowicz is thus not the effect that is responsible for the behavior in CESM.

11. In a way, reducing boundary layer viscosity in CESM may have a similar effect as removing land from the northern coast of New Guinea — due to a reduced boundary layer width, it also causes the flow to stay further south.

12. As long as viscosity does not move the flow path to regions of different wind stress, i. e., as long as $f(Q)$ and $f(T)$ are taken constant in (3.2).

CONTENTS

| | | |
|-------|-----------------------------------|----|
| 4 | Theoretical Analysis | 61 |
| 4.1 | Theory of Cross-Equatorial Flow | 61 |
| 4.1.1 | Equatorial Vorticity Balance | 61 |
| 4.1.2 | The Killworth Model | 64 |
| 4.2 | An Equatorial Shallow-Water Model | 65 |
| 4.2.1 | Model Equations | 65 |
| 4.2.2 | Experimental Setup | 66 |
| 4.2.3 | Analysis | 68 |

THEORETICAL ANALYSIS

4

In literature, flow across the equator is often treated in less detail than mid-latitude circulations, which is probably due to the fact that it is impossible to formulate a leading-order balance as simple as geostrophy. This in turn makes it hard to find simple analytical solutions and gain an intuition of the dominant mechanics in the equatorial regions. In order to understand the findings presented in Chapter 3, it seemed necessary to review the equatorial processes from a more theoretical point of view, which is done in this chapter.

§ 4.1 gives an introduction to the general nature of cross-equatorial flow and ties a first connection between potential vorticity, friction and viscosity, and the overturning. By considering the potential vorticity (PV) balance at the equator, it is found that the presence of friction is indeed crucial to enable cross-equatorial flow. However, the efficiency of the PV transformation is found to be *independent* of the given viscosity to a leading order.

§ 4.2 describes a custom equatorial shallow-water model that is then used to test whether the observed dependency of the overturning on viscosity can be recreated in a highly idealized model. To this end, the response of the equatorial flow and inter-hemispheric mass balance to different viscosities and model resolutions is tested. It is found that neither a simple viscosity reduction, explicitly resolving equatorial eddies, nor an under-resolution of the western boundary layer leads to a similar response as in CESM.

4.1 THEORY OF CROSS-EQUATORIAL FLOW

As a starting point, the following sections present some pictures of cross-equatorial flow, and how exactly it connects to friction and viscosity.

§ 4.1.1 describes how friction in general acts to enable cross-equatorial flow due to potential vorticity constraints. § 4.1.2 then proceeds to analyze cross-equatorial flow quantitatively using a picture brought forward by Killworth, (1991).

4.1.1 Equatorial Vorticity Balance

Currents crossing the equator are strongly suppressed due to potential vorticity conservation constraints. This becomes most evident from the expression for

PV conservation in a layered ocean, (1.22):

$$\frac{D}{dt} \Pi_s = \frac{D}{dt} \left(\frac{\zeta + f}{h} \right) = \frac{1}{h} \nabla_H \times \vec{\mathcal{F}}.$$

As the equator is approached, f becomes smaller and smaller until it vanishes at 0° latitude, and *changes its sign* as the flow penetrates into the opposite hemisphere. Since the layer height h is strictly positive, there are two possibilities how (1.22) can be fulfilled:

1. An exception to this is presented by Nof and Olson, (1993), who show that topography such as the Mid-Atlantic Ridge may allow flow to cross the equator while conserving PV, based on a model from Anderson and Moore, 1979.
- 2) *PV can actually be conserved across the equator by creating excessive relative vorticity ζ (i. e., through nonlinear effects) — however, the resulting velocity shear will usually heavily alter the flow paths and prevent water from deeply penetrating the other hemisphere¹; or*
- 2) *the advection of excess PV along a streamline is balanced by a substantial amount of friction (\mathcal{F}), causing the PV to change sign, until it joins the mid-latitude circulation.*

Another way to recognize the processes that drive flow into the opposite hemisphere stems from a non-dimensional formulation of the vorticity equation given in Bryan, 1963. Bryan assumes a lateral friction term of the form

$$\nabla_H \times \vec{\mathcal{F}} = A_H \nabla^2 \zeta \approx A_H \nabla^2 v_x$$

2. With non-dimensional coordinates x', y' , depth-integrated velocities U, V , and stream function Ψ .

as before, and assumes that the conversion of PV happens predominantly inside western boundary currents. According to Bryan, the steady-state vorticity balance in non-dimensional form can then be approximated as²

$$\underbrace{\varepsilon (U\zeta_x + V\zeta_y)}_{\text{Nonlinearity}} + \underbrace{V}_{\text{Coriolis}} + \underbrace{\sin(\pi y'/2)}_{\text{Wind stress}} = \underbrace{\frac{\varepsilon}{\text{Re}} V^4 \Psi}_{\text{Friction}}$$

3. Recall that the sign of the stream function is in fact tied to the direction of rotation: Ψ is positive for clockwise rotation, and negative otherwise. where ε denotes the horizontal Ekman number, and Re the Reynolds number. From this formulation, it becomes clear that the sign of the lateral friction term $\frac{\varepsilon}{\text{Re}} V^4 \Psi$ is only related to the sign of Ψ close to the boundary. Since we have assumed that the flow crosses in a western boundary current, the friction term $\propto \Psi$ always has the same sign as the V -term³, regardless if the crossing is north-to-south ($V, \Psi < 0$) or south-to-north ($V, \Psi > 0$). For the nonlinear term, no such argument can be made *a priori*.



Both types of cross-equatorial flow (PV conserving flow and flow in frictional balance) are studied in many models and applications throughout literature. In

the upcoming sections, we shall assume that the second mode, which depends on friction, has the most relevance in the real ocean, based on a picture that was put forward in Killworth, 1991 (see next section). However, we need to keep in mind that, in theory, PV conserving modes are possible (Nof and Olson, 1993).

4.1.2 The Killworth Model

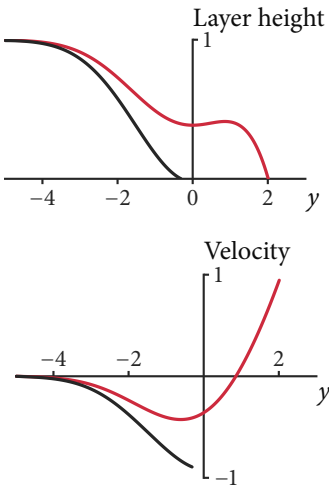


Figure 4.1: Two steady-state solutions (with different starting latitudes) of one-dimensional equatorial geostrophic adjustment. ODE as in Killworth, 1991; solved with a shooting method.

A particularly interesting study of the dynamics of cross-equatorial geostrophic adjustment has been conducted by O. Killworth (Killworth, 1991).

In the first part of his paper, Killworth derives a set of nonlinear ordinary differential equations (ODEs) describing the long-time average solution of a dam-break scenario where water, starting with some height anomaly h from a latitude Y south of the equator, is released in an inviscid, one-dimensional ocean. He finds that the flow is able to penetrate at most two Rossby radii of deformation into the northern hemisphere, depending on the starting latitude Y (Fig. 4.1). In this scenario, PV is conserved by creating excessive amounts of relative vorticity (i. e., through the first mode as described in § 4.1), turning the flow into an eastward jet, until it cannot penetrate any further (layer height approaches zero). This shows that, in the absence of solid boundaries and friction, deeply penetrating cross-equatorial flow is impossible, or — in other words — that one-dimensional nonlinearities alone cannot enable a full-blown overturning.

In the second part of the paper, Killworth extends the model to a two-dimensional basin, and a lateral friction term is added. He proceeds to show that the circulation now spans the whole basin, because a western boundary current that is in frictional balance permits long migration of water parcels into the opposite hemisphere. By lowering the viscosity parameter, he finds a reduction of cross-equatorial flow in the interior, but not in the western boundary layer.

4. This implies $u = 0$ and $v_x \gg v_y$.

This behavior can be understood by assuming that the flow occurs in a thin, strictly meridional western boundary layer in lateral friction balance⁴, i. e., it can be described as a Munk layer (cf. § 1.2.2). The dominant balance in the potential vorticity conservation equation for a layered ocean (1.22) is then

$$\frac{D}{dt} \Pi_s \propto \frac{1}{h} A_H v_{xxx}. \quad (4.1)$$

Since the typical zonal length scale in a Munk layer δ_M is given by (1.26), i. e.,

$$\delta_M = \left(\frac{A_H}{\beta} \right)^{1/3},$$

5. Assuming that the layer height h is approximately constant along stream lines.

the right hand side of (4.1) is of the order⁵ $\mathcal{O}(v) = V$. The left hand side of (4.1) (material derivative of PV) involves a time derivative, and the total time spent in the boundary layer is $\propto V^{-1}$. Thus, the total transformation of potential vorticity in the boundary current is of order 1 to a leading order. *This implies that the magnitude of A_H does not influence the efficiency of PV modification in a Munk layer in a first order approximation, as long as friction is present at all, and the Munk layer is resolved in the model.*

4.2 AN EQUATORIAL SHALLOW-WATER MODEL

After these theoretical considerations, I wanted check whether the same behavior observed in the CESM experiments from Chapter 3 can be reproduced by simply reducing viscosity in a highly idealized model⁶. For this purpose, I ran some additional experiments with a shallow-water model that I have developed, based on the models used in Killworth, 1991 and Kawase, 1987. In particular, I wanted to obtain a similar dependence of total cross-equatorial transport and structure of the equatorial flow field on viscosity as observed in the Atlantic in my Community Earth System Model (CESM) experiments (§ 3.2.3), while only modeling a single active layer of fluid with homogeneous velocities and density (as in § 1.1.3), and without any wind forcing. Instead, the model is forced by buoyancy only (a constant mass source in the north-western corner of the domain).

I have specifically chosen the model equations and parameters to yield a solution that is somewhat similar to a long-term average of the deep branch of the AMOC, while the upper branch is modeled implicitly by assuming that it always closes the meridional overturning. Like the real Atlantic Meridional Overturning Circulation (AMOC), it is forced by a mass imbalance in the North⁷, representing the creation of North Atlantic Deep Water (NADW). However, I did not want to prescribe the magnitude of the cross-equatorial flow as in e. g. Edwards and Pedlosky, 1998. Hence, as a mass sink, I have chosen to implement uniform upwelling⁸ proportional to the layer height anomaly as in Kawase, 1987, so a solution that stays entirely inside the northern hemisphere becomes possible.

The following sections describe the equations that are solved by the model (§ 4.2.1), and the experiments I have conducted, along with the observations I have made during the analysis (§ 4.2.2).

4.2.1 Model Equations

The shallow-water model I have implemented is basically a combination of the shallow-water models used in Killworth, 1991 and Kawase, 1987, with an additional CESM-style anisotropic friction term. Killworth uses a non-dimensional unforced shallow-water model with lateral friction in Cartesian coordinates:

$$\begin{aligned} u_t + uu_x + vu_y - \frac{1}{2}yv + h_x &= A_H(u_{xx} + u_{yy}) \\ v_t + uv_x + vv_y + \frac{1}{2}yu + h_y &= A_H(v_{xx} + v_{yy}) \\ h_t + (uh)_x + (vh)_y &= 0 \end{aligned}$$

6. As shown in the previous section, viscosity has no influence on a pure Munk layer — however, it is not clear *a priori* what happens when this layer is under-resolved, or how nonlinearities change the solution.

7. Which is, however, assumed constant, to only observe the *kinematic* effects of a reduced viscosity — an assumption that is only a first order approximation of the real ocean.

8. By simply removing water from the domain, implicitly assuming that it re-enters the “upper branch” of the basin instead.

KILLWORTH'S MODEL

with (non-dimensional) velocities u, v ; layer height h ; meridional position y ;

KAWASE'S MODEL

9. Or exponential growth for $\eta < 0$,
i. e., a negative displacement relative to the undisturbed layer height.

DION'S SHALLOW-WATER MODEL

10. $h - 1 = \eta$, since the non-dimensional undisturbed layer height $H' \equiv 1$ in the Killworth model.

and turbulent diffusivity A_H . Kawase on the other hand uses a forced shallow-water model with bottom friction in spherical coordinates:

$$\begin{aligned} u_t - 2\Omega \sin \theta v + \frac{g}{R_e \cos \theta} \eta_\phi &= -\kappa u \\ v_t + 2\Omega \sin \theta u + \frac{g}{R_e} \eta_\theta &= -\kappa v \\ \eta_t + \frac{H}{R_e \cos \theta} u_\phi + \frac{H}{R_e \cos \theta} (\cos \theta v)_\theta &= Q - \lambda \eta, \end{aligned}$$

with Coriolis parameter $2\Omega \sin \theta$; Earth's radius R_e ; reduced gravity g ; bottom friction parameter κ ; background layer height H and height anomaly η ; a localized water source Q ; and a water sink parameter λ parameterizing diapycnal mixing. The source in this model is located at the north-western corner of the domain, and the water sink is modeled as an exponential decay term⁹.

Combining these two models, I arrived at a non-dimensional, Cartesian formulation with buoyancy forcing, anisotropic lateral friction as in CESM, and proper treatment of the convection term in the h equation:

$$\begin{aligned} u_t + uu_x + vu_y - \frac{1}{2} yv + h_x &= (Au_x)_x + (Bu_y)_y \\ v_t + uv_x + vv_y + \frac{1}{2} yu + h_y &= (Bv_x)_x + (Av_y)_y \\ h_t + (uh)_x + (vh)_y &= Q - \lambda(h - 1), \end{aligned}$$

with definitions as in the Killworth model, but with an additional sink as in Kawase, 1987¹⁰. Note that this term adds a diapycnal contribution to the PV conservation equation (1.10), so PV is not strictly conserved, even in the absence of friction (however, we assume this term to be small, since all experiments are in the low-damping regime). The buoyancy forcing is modeled as an explicit mass source Q in the north-western corner of the basin.

For a description of the numerical implementation and verification of this model refer to Appendix B.

4.2.2 Experimental Setup

After reproducing some published results with my model to verify that it is working correctly (Appendix B), I ran a total of three sets of simulations to investigate the equatorial dynamics in different scenarios:

- 1) *High resolution, low forcing: In this first set, the model is forced by an explicit source Q in the north-western corner of the basin corresponding to a forcing of 12 Sv. Between experiments, only the Munk layer viscosity v_M is changed ($v_M = 0, 0.2, 2.0$). All other viscosity parameters as in the CESM run x3_- default. The model grid consists of 60×120 equally spaced grid cells.*

- 2) *High resolution, high forcing:* As the first set, but with a stronger forcing of 48 Sv, to allow for more nonlinearities in the solution. All runs are initialized with the final state of the $v_M = 0.2$ experiment from set 1. To make computations more efficient, the grid spacing is reduced around the equator and western boundary, and increased everywhere else (same total number of grid cells).
- 3) *Low resolution, low forcing:* Four low-resolution simulations with Munk layer viscosities 10^3 , 10^4 , 10^5 , and $10^6 \text{ m}^2 \text{ s}^{-1}$. 20 equally spaced grid cells in x -direction, and 80 cells in y -direction, with a four times finer grid at the equator than at the northern and southern boundaries¹¹. Forcing as in set 1.

11. This grid was chosen to achieve a similar spatial resolution as in the x3 CESM runs.

Furthermore, all experiments share the following setup:

- ▶ a rectangular basin that extends 6000 km in zonal (x) and 12 000 km in meridional (y) direction, with the equator in the middle;
- ▶ a dampening time scale λ^{-1} of 1 year, putting the experiments into the weak damping regime as defined in Greatbatch and Lu, 2003; and
- ▶ an undisturbed layer height H of 400 m, a reduced gravity g of 0.02 m s^{-2} , and a Coriolis parameter β of $2 \times 10^{-11} \text{ s}^{-1} \text{ m}^{-1}$.

All of these values were chosen with the deep branch of the AMOC in mind, while still being sufficiently close to the studies in Killworth, 1991 and Greatbatch and Lu, 2003 to allow comparisons.

The model is integrated forward using a finite volume solver for at least 1000 days, i. e., approximately three damping time scales. To ensure stability and accuracy, the model uses adaptive time step control, with a typical time step lying in the order of 15 minutes. In every time step, an absolute solver precision of 10^{-8} in dimensionless units is enforced for both velocities and layer height.

4.2.3 Analysis

Equatorial flow (set 1)

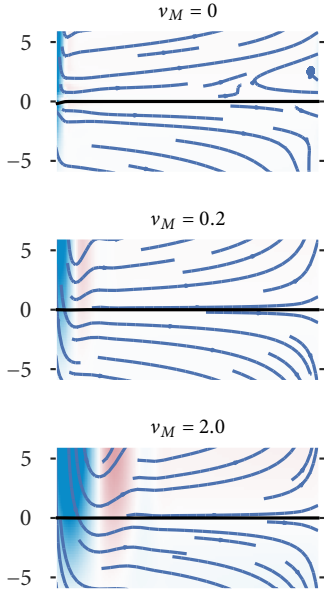


Figure 4.2: Equatorial regions of the first set of shallow-water simulations (with varying Munk layer viscosity). Shown are the streamlines, advection of PV (shading), and contour of zero PV (black line).

Set 1: High resolution, low forcing

In this setup, the relatively weak forcing keeps nonlinearities small. As a consequence, all solutions are very similar, apart from a varying boundary layer width (which is, after all, $\propto A_H^{1/3}$) and different levels of numerical (dispersive) noise. The resulting steady-state solution is symmetric around the equator, similar to the weak-damping solutions in Greatbatch and Lu, 2003 (Fig. 4.3; see also Appendix B), and flow seems to cross the equator in the western boundary layer only. The structure of the steady-state solution seems largely indifferent to viscosity (Fig. 4.2) — higher viscosities only lead to a wider boundary layer, and a more pronounced recirculation as predicted by the Munk solution, i. e., (1.27).

The amount of water H_{south} that manages to penetrate deep into the southern hemisphere can be used as a diagnostic for the “overturning” in the model, by simply evaluating a mass integral over some southern region, i. e.,

$$H_{\text{south}} = \int_{x_w}^{x_e} \int_{y_s}^{y^*} h \, dy \, dx,$$

with the layer height h , x_w , x_e , y_s denoting the position of the western, eastern, and southern boundary, respectively, and some bounding latitude y^* that separates north from south. Since the observed equatorial features tend to extend quite far into both hemispheres (Fig. 4.3), I have chosen $y^* = -10$ (non-dimensional; in multiples of the Rossby radius of deformation). A better estimate for the overturning that is comparable between different scenarios is the mass ratio between northern and southern parts of the domain, i. e., $H_{\text{south}}/H_{\text{north}}$. Calculating this value for every experiment reveals that the steady-state mass balance is indeed quite stable around $(7 \pm 1)\%$ for any Munk layer viscosity (Fig. 4.4), especially for the two runs with a non-vanishing Munk layer. However, it seems that higher viscosities lead to a *weaker* overturning, which is in contradiction with the findings of Chapter 3. It is also observed that higher viscosities lead to a delayed reaction of the southern part of the basin, i. e., longer overall time scales.

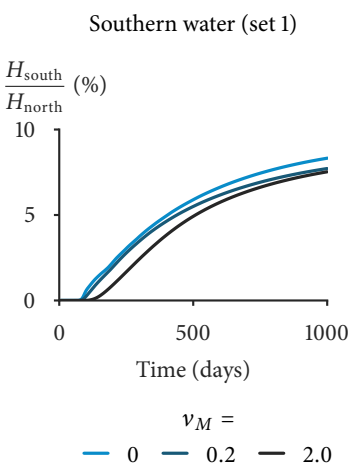


Figure 4.4: The steady-state mass balance between North and South seems to be largely independent of viscosity.

Steady state for $\nu_M = 0.2$

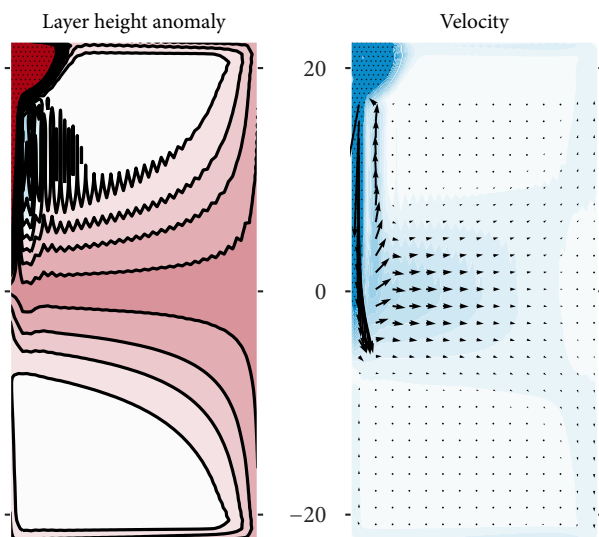


Figure 4.3: The steady-state solution in the high resolution, low forcing case is symmetric around the equator. Contours and quivers in the forcing region / western boundary partly omitted. Shading left: layer height anomaly; right: velocity magnitude. Coordinates in non-dimensional units.

Set 2: High resolution, high forcing

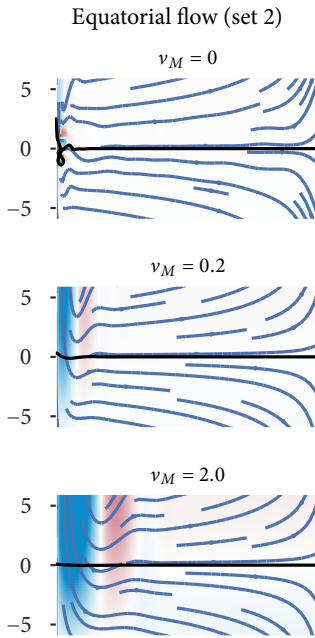


Figure 4.5: Equatorial regions of the second set of shallow-water simulations (with varying Munk layer viscosity). Shown are the streamlines, advection of PV (shading), and contour of zero PV (black line).

In this scenario, the forcing strength has been quadrupled to increase velocity and height anomaly scales, which increases the nonlinearity of the solution. Indeed, while the overall structure of the solution is still the same as in the first scenario, the experiment without a Munk layer now features a number of eddies that constantly emerge in the equatorial region near the western boundary, travel southward, and dissipate. This is also visible in Fig. 4.5, where the line of zero PV is visibly distorted close to the western boundary.

The inter-hemispheric mass balance (Fig. 4.6) reveals that all experiments converge to roughly the same steady-state, with differences of the order of 1‰, which also seems to be roughly the same steady-state that the solution was initialized with (final state of the $v_M = 0.02$ experiment from set 1). Strictly speaking, the experiment with the highest viscosity *does* lead to the largest amount of southern water after 2200 d, but differences are so small that this might as well change once more when integrating for even longer times.

It seems curious that the low-viscosity run from set 1 was clearly set apart from the other experiments (Fig. 4.4), while this is not the case here. However, it is important to recall that I have also introduced a scaled numerical grid before running the experiments of set 2, which becomes finer near the equator and *the western boundary*. My hypothesis to explain the observed behavior is thus that the western boundary layer was not fully resolved in the low-viscosity run of set 1, while it is well-resolved in set 2 due to the finer grid spacing at the western boundary.

Hence, it seems that a fully resolved boundary layer *always leads to an identical hemispheric mass balance in the steady-state*, regardless of nonlinearities (while during spin-up, the system reacts considerably faster with lower viscosities, which might be an important factor in the real ocean / CESM).

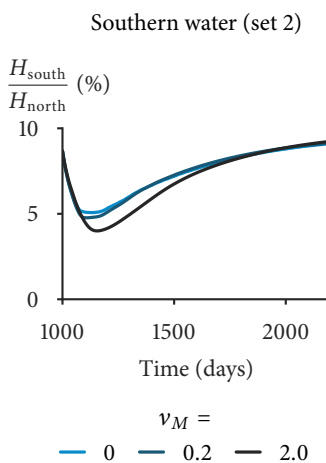


Figure 4.6: Even for nonlinear solutions, the steady-state mass balance between North and South seems to be independent of viscosity.

Set 3: Low resolution, low forcing

This set of simulations was deliberately run with a low spatial resolution to test the effects of under-resolving the western boundary layer. This creates excessive amounts of numerical noise, as also seen in the CESM experiments — thus, all variables have been smoothed with a boxcar filter in both dimensions before post-processing.

Compared to the symmetric solutions obtained in set 1 and 2, the structure of the solution changes considerably in the low-viscosity runs (Fig. 4.7). The symmetry around the equator is broken, and, interestingly, the largest effect is seen in the circulation of the *northern* hemisphere. Part of the flow crosses in the western boundary, but large parts of the flow do not make it across the equator, and are deflected eastward instead. When hitting the eastern boundary, this flow turns southward, and is deflected to the west by the equator. A similar process is observed *after* the flow has crossed the equator, but fails to penetrate deeply into the southern hemisphere. It is deflected eastward until hitting the eastern boundary, where it dumps excess PV, and joins the southern circulation (Fig. 4.8). It seems odd that processes at the *eastern* boundary actually manage to transform PV in the same way as the western boundary, since it is analytically impossible to find a stable solution that balances friction and planetary vorticity at the eastern boundary (Pedlosky, 1996). Possible explanations for the observed behavior could be:

- 1) *The diapycnal term in the PV conservation equation (1.10) becomes important in this region and acts to remove some potential vorticity;*
- 2) *Strong numerical noise may lead to an inaccurate solution; or*

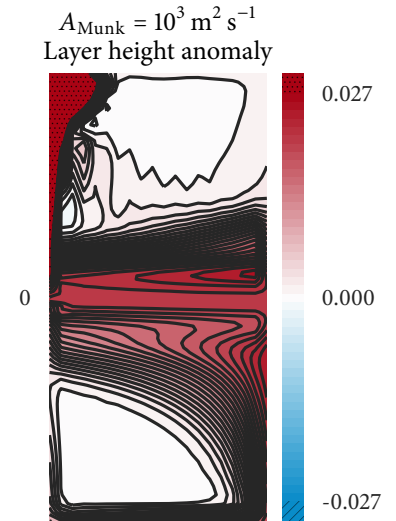


Figure 4.7: Lowering viscosity creates zonal re-circulations in the equatorial band. Shown is the smoothed layer height anomaly.

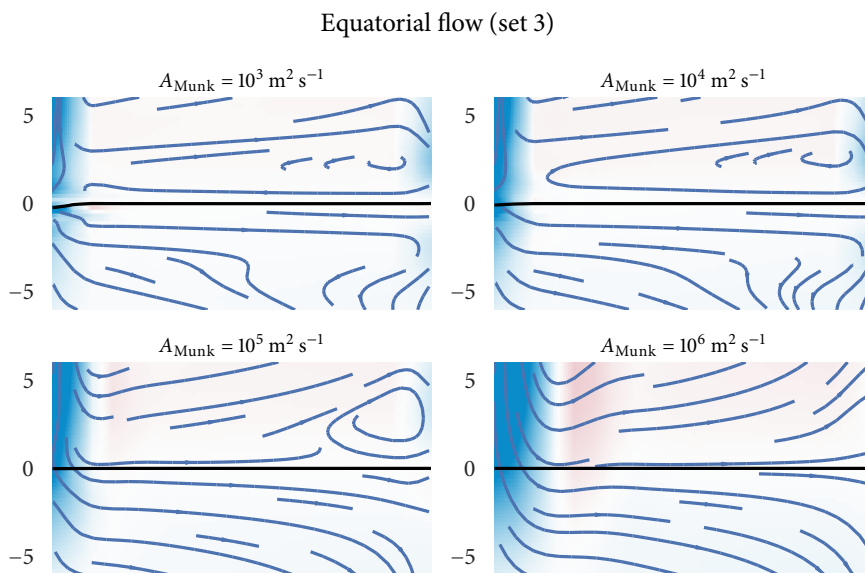


Figure 4.8: The equatorial flow pattern shows a distinct dependency on viscosity. Shading: PV advection (different scale for each solution).

Southern water (set 3)

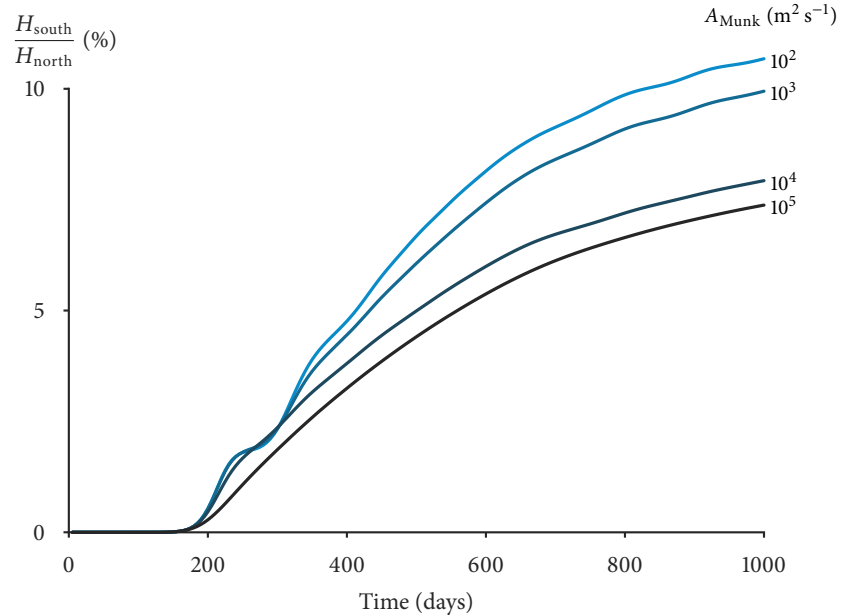


Figure 4.9: The *lower* the viscosity, the *more* water reaches far south in my shallow water model. Division between north and south at 10 deformation radii south of the equator.

- 3) Calculating relative vorticity during post-processing is quite inaccurate for low-resolution grids, and PV could in fact be conserved. In this case, the observed re-circulation would be purely inertial, which is a well-known solution (the Fofonoff mode, see Ocean Circulation Theory (Pedlosky, 1996)).

Thus, even though somewhat similar processes are observed in the Atlantic in my CESM experiments for low viscosities (Fig. 3.8), it is doubtful how realistic the interactions at the eastern boundary are modeled in this set of experiments.



The inter-hemispheric mass balance for this set seems curious, too (Fig. 4.9). Apparently, an under-resolved Munk layer does indeed lead to a *much larger* amount of water that crosses the equator and reaches far south, as already suspected when comparing the results from set 1 and 2. While the high viscosity experiments lead to a mass balance that is similar to that of set 1, the low viscosity runs exceed it significantly. My only explanation for this observation is that, since northern water is effectively trapped in the equatorial region, there is simply more opportunity for a large portion of the flow to actually cross the equator, be it at the western boundary or in the interior, before it is removed from the basin.

Summary

Albeit my buoyancy-forced shallow water model has shown some interesting features, it has eventually failed to reproduce the dependency of the Meridional Overturning Circulation (MOC) on viscosity as seen in the CESM experiments of Chapter 3 (i. e., a slightly reduced transport for reduced viscosities), even when equatorial eddies were explicitly resolved (set 2) or when the equatorial Munk layer was under-resolved (set 3).

I thus conclude that neither of the examined effects effects¹² is responsible for the observed response of CESM. Further possible candidates that may cause the observed dependency are e. g. topography, interactions between multiple layers, atmospheric forcing, or simply the fact that the NADW forcing is not constant (since it depends both explicitly on time through e. g. seasonal forcing and on the actual cross-equatorial flow itself). Hence, further work seems necessary to identify the dominant processes in CESM; some possible modifications are presented in § 5.2.1.

12. I. e.,

- 1) *direct response to changed viscosity,*
- 2) *simple nonlinearities,*
- 3) *under-resolution of the western boundary layer.*

CONTENTS

| | | |
|-------|--|----|
| 5 | Wrap-up | 75 |
| 5.1 | What Have We Learned? | 75 |
| 5.1.1 | Numerical Noise | 75 |
| 5.1.2 | The Atlantic Meridional Overturning Circulation | 76 |
| 5.1.3 | The Indonesian Throughflow | 76 |
| 5.2 | Open Questions | 77 |
| 5.2.1 | How is the overturning modified when changing viscosity? | 77 |
| 5.2.2 | What controls the origin of the Indonesian Throughflow? | 78 |

WRAP-UP

5

This chapter connects the dots that are the many different observations and conclusions made in previous chapters, describing both what has been done and what could still be done and is meant to close the arc between my CESM experiments (Chapter 3) and theoretical studies (Chapter 4).

§ 5.1 gives a summary of the main results of my thesis, while § 5.2 discusses some open questions and how they could be tackled in future work.

5.1 WHAT HAVE WE LEARNED?

The following sections describe the observations I have made when lowering the western boundary layer viscosity at the equator in CESM experiments with low (x_3) and intermediate (x_1) resolution (Chapter 3), along with my “best guess” on how to interpret these results, taking into account the theoretical findings from Chapter 4.

A particular focus lies on the generation of numerical noise (§ 5.1.1), cross-equatorial flow in the Atlantic (§ 5.1.2), and the Indonesian Throughflow (ITF) (§ 5.1.3).

5.1.1 Numerical Noise

The main result of § 3.2.1 is that, while an intact boundary layer with low grid scale Reynolds numbers is critical for numerical noise suppression in the equatorial regions¹, the smoothed velocity field is still a decent representation of the actual dynamics.

Noise is mostly created on grid scale and preferably in zonal direction, which is also observed in my shallow-water model. This is probably due to the fact that 1) meridional grid spacings are smaller than those in zonal direction close to the equator, and that 2) velocity shears are dominantly in zonal direction (due to the sharp western boundary layer).

The total amount of generated noise under viscosity reduction seems to depend critically on the given grid spacing — much less noise is observed in x_1 or the high-resolution shallow-water experiments, even when grid scale Reynolds numbers are high.

1. Which I hypothesized to be the case because information always travels *westward* in the ocean, hence noise created in the interior basin can not be dissipated without a western boundary layer.

5.1.2 The Atlantic Meridional Overturning Circulation

The total transport carried by the Atlantic Meridional Overturning Circulation (AMOC) only depends weakly on viscosity. When only accounting for contours of the vertical AMOC stream function that penetrate far into the opposite hemisphere, the transport changes by a maximum of -1.5 Sv (for x_3_{nomunk} , where the Munk layer viscosity has been globally reduced to the much lower background value), while integrating directly over the velocity at the equator yields a maximum change of about -1.2 Sv (again, for x_3_{nomunk}). This is less than anticipated intuitively, considering that, without friction, the required transformation of potential vorticity (PV) to enable cross-equatorial flow is impossible. However, it is shown that the efficiency of PV transformation inside a Munk boundary layer is independent of viscosity to a leading order (§ 4.1.2).

On the other hand, I *did* observe a clear correlation between viscosity and cross-equatorial transport, where lower viscosities always led to a decreased transport, and vice versa. In order to understand this behavior, I have tried to produce a similar response in an equatorial shallow-water model that is forced by a constant buoyancy forcing and uniform “upwelling” across the domain. After running several simulations in different scenarios (§ 4.2), I was not able to reproduce the observed response in this simple model². I thus conclude that the response of the ocean in Community Earth System Model (CESM) depends on effects that were not included in my model (some possible candidates are discussed in § 5.2.1).

Looking at the flow field around the equator in the Atlantic in CESM, I noticed deep, zonal equatorial jets (similar to those described in Greatbatch et al., 2012) that emerge along the equator and extend all the way to the eastern boundary, where it seems like some boundary layer interactions took place. In CESM experiments with extreme viscosity modifications, a roughly equal amount of water crosses the equator in the eastern and western parts of the basin. *The structure and efficiency of the western boundary thus indeed seems to be affected heavily by strong viscosity modifications.*

5.1.3 The Indonesian Throughflow

The total transport crossing the ITF shows roughly the same dependence on viscosity as the AMOC, with maximum changes of about -2 Sv in x_3 , and -0.5 Sv in x_1 .

On top of these small modifications of the total transport (which are expected to be small considering Munk layer theory as in § 4.1.2), dramatic changes of the composition of the ITF are observed in the x_3 experiments³. The barotropic stream function (BSF) suggests that, for extreme viscosity modifications, about

2. Instead, transports were either independent of viscosity, or increased for smaller viscosities (if the boundary layer was under-resolved).

3. x_1 experiments seem to be largely unaffected because of a very different geometry around the Indonesian islands.

half of the total ITF originates in the southern hemisphere, versus a purely northern source when using default viscosity parameters. This is reinforced by the salinity profile of this region, which shows a considerably saltier ITF for low viscosities, which also hints towards a southern source.

In § 3.3, I have reviewed Godfrey's Island Rule. Since the Island Rule predicts an ITF that only depends on the atmospheric forcing and geometry, the observed dependency of the transport on viscosity seems like a contradiction. An extension of the Island Rule with friction (from Wajsowicz, 1993b) predicts a *weaker* transport for *higher* viscosities, i. e., the opposite of what is observed in CESM. It thus seems like the Island Rule, while it delivers a good first approximation, is indeed not strictly valid at the equator.

After all, the processes that determine the source of the ITF are still unclear. Some additional possibilities are discussed in § 5.2.2.

5.2 OPEN QUESTIONS

The following sections are meant to point out some loose ends in this study, where future work would be necessary to get a clearer understanding, and presents some further ideas that fell out of the scope of this thesis.

In particular, there are two major open questions, one concerning the total strength of the overturning (§ 5.2.1), and one concerning the ITF (§ 5.2.2).

5.2.1 How is the overturning modified when changing viscosity?

Since my shallow-water model could not reproduce CESM's dependence of the overturning on viscosity, it is still unclear *how* the total cross-equatorial transport can be modified by changing viscosity, even though theory predicts that it should be constant to a leading order (§ 4.1.2). Apparently, this response is created by an effect that was not modeled in the shallow-water experiments. Some likely candidates are:

- 1) *boundary topography, which modifies the balance between friction and Coriolis force if the boundary layer is not strictly meridional, and bottom topography (see e. g. Nof and Olson, 1993 and Swaters, 2015);*
- 2) *interactions between multiple layers, as discussed e. g. in Nof, 1990, or the effect of a vanishing layer height (cf. (4.1));*
- 3) *additional forcing by the wind; and*
- 4) *a feedback between the forcing of the model and the amount of equator-crossing flow.*

4. One possibility would be to use a verified GCM such as the MIT General Circulation Model (MITgcm), which supports idealized processes and geometries, instead of a self-developed model.

For starters, an enhanced model could include a realistic geometry of the North Atlantic, and explicitly model both branches of the AMOC (northward, shallow and southward, deep). This model should be much closer to reality, and hopefully give a realistic dependence on viscosity⁴.

Another clue towards the processes in a low-viscosity Atlantic is given by the equatorial jets that are observed in some experiments. These jets are studied and modeled in Kitamura and Ishioka, 2007, and a similar study could reveal their connection to cross-equatorial transport and viscosity.

5.2.2 What controls the origin of the Indonesian Throughflow?

5. E. g. in Nof, 1996; Godfrey, Wilkin, and Hirst, 1993; Lukas, Yamagata, and McCreary, 1996; Gordon, 1986.

The origin of the ITF is in fact highly discussed in literature⁵, and observations suggest a predominantly northern source. However, none of these studies seems to include the dependence of the ITF composition on viscosity. Possible explanations for the observed, sensitive dependence of the ITF on viscosity are:

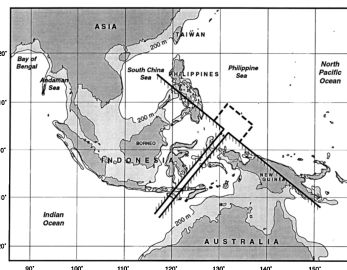


Figure 5.1: The ITF model presented in Nof, 1996.

- ▶ In Nof, 1996, Doron Nof considers a nonlinear, frictionless model of the ITF with an idealized geometry (Fig. 5.1). He shows that the determining factor for the origin of the ITF in this model is (1) the geometry of the basin and (2) the undisturbed layer heights at certain points of the current system in the ITF. While not taking viscosity into account explicitly, these layer heights are certainly influenced by the Munk layer viscosity in this region, which could yield an explanation for the observed behavior.
- ▶ Since the most direct effect of a reduced viscosity is a lower boundary layer width, it is certainly possible that the ensuing geometrical alteration of the flow path has a direct influence on the solution in the ITF region. Even a slightly displaced path may have a large influence eventually, e. g. through a spatially dependent wind stress, or the “collision” with other currents.
- ▶ In fact, since the efficiency of the cross-equatorial transport in a western boundary layer was found to be influenced dramatically by viscosity in the Atlantic, it seems like the same may be the case here — flow that fails to dump excess vorticity follows the coast of New Guinea without crossing the equator further than a few Rossby radii of deformation, and then curves back into the southern hemisphere. The flow does not need to form a jet as in the Atlantic, since it never actually crosses the equator in $x3$ ⁶. However, this interpretation still needs careful testing, e. g. in another idealized model with a geometry that is similar to that of the Indonesian islands and New Guinea.

It seems thus, that frictional control of cross-equatorial flow is indeed possible in low-resolution models, and that the chosen model viscosity does have a decisive influence on the flow in the equatorial regions (though not so much on its total magnitude).

APPENDICES

A ADDITIONAL PLOTS

A.1 VISCOSITIES OF ALL CESM EXPERIMENTS

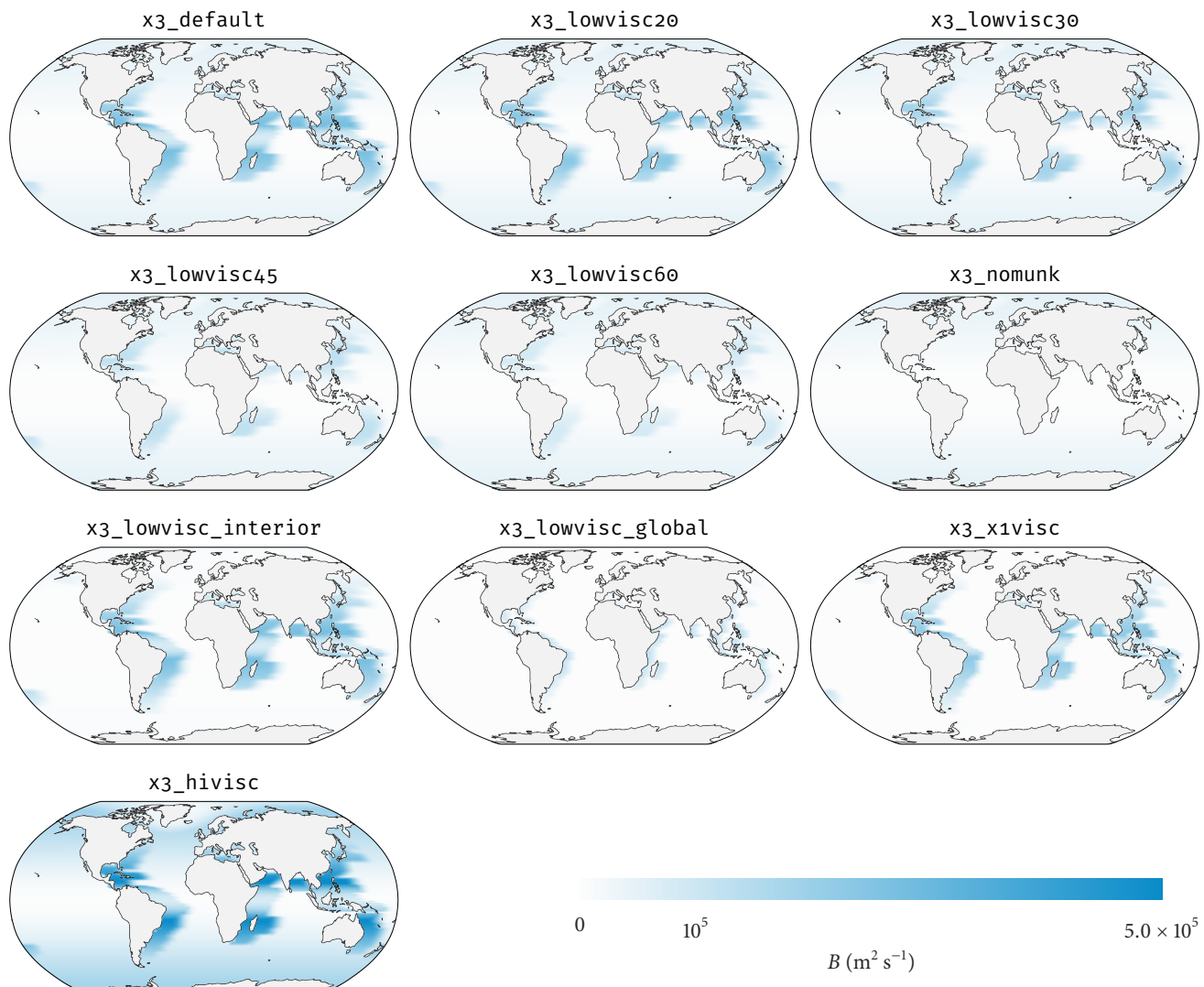


Figure A.1: Perpendicular viscosity parameter B for all $x3$ runs.

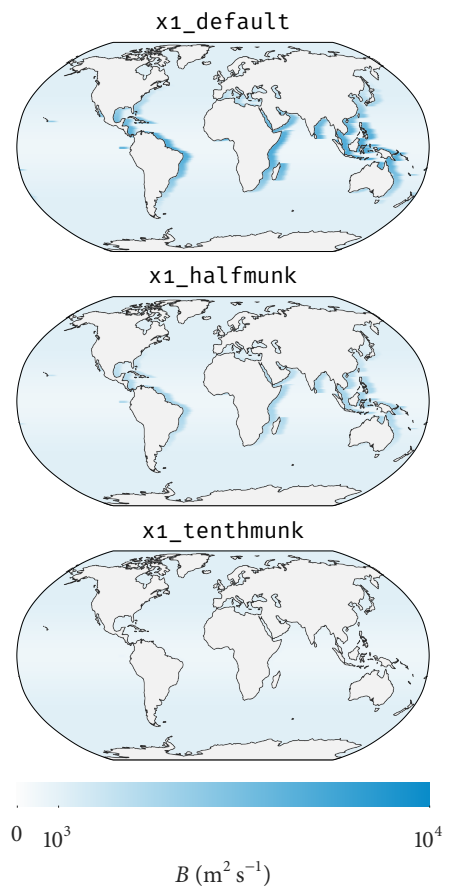


Figure A.2: Perpendicular viscosity parameter B for all $x1$ runs. Note the changed scale from Fig. A.1.

B

AN EQUATORIAL SHALLOW-WATER MODEL (CONT.)

The following sections describe some technical aspects of the shallow water model used in § 4.2. § B.1 gives a summary of the numerical implementation of the model, while § B.2 focuses on the reproduction of some results found in literature (Killworth, 1991 Greatbatch and Lu, 2003), in order to verify the consistency of the model, and to allow for the detection of obvious errors in the implementation. Although no quantitative analysis is made, my shallow water model succeeds in reproducing the structure of each solution.

B.1 NUMERICAL IMPLEMENTATION

When implementing numerical models, oceanographers often apply a low-level approach, by explicitly discretizing the model equations using finite differences (see e. g. Kämpf, 2009). These implementations are usually very efficient, but on the flip side quite static — adding additional terms is cumbersome, since the numerical properties of the chosen scheme have to be preserved, and many methods work on regular meshes only.

Because it was important to me that my model supported an “agile” development style allowing for quick prototyping, I have decided not to implement it from scratch using finite differences, but rather make use of the FiPy software package (Guyer, Wheeler, and Warren, 2009), a finite volume solver framework that is accessed via the Python programming language. FiPy pre-defines finite-volume implementations for the most common terms that appear in partial differential equations (PDEs). On their homepage¹, the FiPy developers summarize the capabilities of FiPy:

“The solution of coupled sets of PDEs is ubiquitous to the numerical simulation of science problems. Numerous PDE solvers exist, using a variety of languages and numerical approaches. Many are proprietary, expensive and difficult to customize. As a result, scientists spend considerable resources repeatedly developing limited tools for specific problems. Our approach, combining the FV method and Python, provides a tool that is extensible, powerful and freely available. A significant advantage to Python is the existing suite of tools for array calculations, sparse matrices and data rendering.

The FiPy framework includes terms for transient diffusion, convection and stan-

1. <http://www.ctcms.nist.gov/fipy/>

dard sources, enabling the solution of arbitrary combinations of coupled elliptic, hyperbolic and parabolic PDEs.”

Using FiPy, the actual formulation of the model equations becomes much easier (Code Listing B.1) and, for the most part, does not depend on the actual numerical implementation of the various terms. This way, I could explore a wide range of problems with different formulations of the model equations and model grids. The FiPy solutions also tended to be quite stable, since most of the terms are solved implicitly². However, this comes of course at a computational cost — by choosing FiPy, I accepted higher run times in exchange for a lower implementation time, which seemed adequate for a project that is as time constrained as a Master’s thesis.

2. Unfortunately, FiPy does not allow to formulate the shallow-water equations in a fully implicit manner (since the face velocities need to appear as explicit sources).

```

1  diffCoeffX = FaceVariable(mesh=mesh, rank=1)
2  diffCoeffX[0] = A.faceValue
3  diffCoeffX[1] = B.faceValue
4  diffCoeffY = FaceVariable(mesh=mesh, rank=1)
5  diffCoeffY[0] = B.faceValue
6  diffCoeffY[1] = A.faceValue
7
8  fDiv = faceVelocity.divergence
9  waterSourceInterior = \
10   (ImplicitSourceTerm(coeff=1., var=height)-1) / \
11   dampening_scale
12
13 xVelocityEq = TransientTerm(var=xVelocity) \
14 + ConvectionTerm(coeff=fVelocity, var=xVelocity) \
15 - ImplicitSourceTerm(coeff=fDiv, var=xVelocity) \
16 - ImplicitSourceTerm(var=yVelocity, coeff=.5*mesh.y) \
17 == \
18 - height.grad.dot((1.,0.)) \
19 + DiffusionTerm(diffCoeffX, var=xVelocity)
20
21 yVelocityEq = TransientTerm(var=yVelocity) \
22 + ConvectionTerm(coeff=fVelocity, var=yVelocity) \
23 - ImplicitSourceTerm(coeff=fDiv, var=yVelocity) \
24 + ImplicitSourceTerm(var=xVelocity, coeff=.5*mesh.y) \
25 == \
26 - height.grad.dot((0.,1.)) \
27 + DiffusionTerm(diffCoeffY, var=yVelocity)
28
29 heightEq = TransientTerm(var=height) \
30 + ConvectionTerm(coeff=fVelocity, var=height) \
31 == \
32 waterSourceBoundary - waterSourceInterior
33
34 # couple equations
35 swEquations = xVelocityEq & yVelocityEq & heightEq

```

Code Listing B.1: Equation setup for the shallow-water model in FiPy. The cell-centered variables of the model are called `height`, `xVelocity`, and `yVelocity`. Some terms use the rank 1 `FaceVariable` `fVelocity`, which is the linearly interpolated velocity at cell faces. `A` and `B` are `CellVariables` holding the parallel and perpendicular viscosities, respectively. `WaterSourceBoundary` represents the forcing of the model (Gaussian in the north-western corner of the domain).

B.2 VERIFICATION

B.2.1 Killworth, 1991

As a first step, I have used my shallow-water model to qualitatively reproduce the figures shown in the second part of Killworth, 1991. For this purpose, I have deactivated all forcing ($\lambda = Q = 0$), and integrated the model forward for 100 d starting with a dam-break scenario, using parameters as in Table B.1³, which are the same as used by Killworth. During the integration, the expected features such as Kelvin waves traveling along the boundaries of the domain are visible.

The final state after 100 d bears a striking resemblance with the corresponding figure from Killworth, 1991 (Fig. B.1). The height field, which coincides with stream lines in high latitudes, shows the same two large circulation cells in the western half of the basin with a comparable magnitude. The velocity field reveals that water predominantly crosses the equator in a western boundary current, from where it either enters the circulation far north, or re-circulates into the southern hemisphere in the interior.

Considering how similar the resulting figures look, given that the two models are implemented using entirely different numerical schemes (finite volume method vs. finite differences on a Arakawa C-grid⁴), and presumably use different resolutions (used resolution not reported in Killworth, 1991), I assume my shallow water model to be working correctly for this application.

B.2.2 Greatbatch and Lu, 2003

Greatbatch and Lu, 2003 contains an interesting study of the Kawase, 1987 model, giving a range of numerical solutions for different damping timescales. Since the implementation and used parameters are well described, this publication is a valuable resource to verify my model with a forced reference. However, since the Kawase model equations differ slightly from the ones I have used in my model⁵, a comparison has to remain qualitative.

Since we are only interested in the low damping regime⁶, I have used a damping time scale of 1 y for my experiments. Comparing the steady state solution of a high viscosity run with the corresponding figure given in Greatbatch and Lu, 2003 (Fig. B.2) reveals another striking similarity. In the steady state, the interior height field is symmetric around the equator, with a narrow western boundary current and a wide interior circulation. During spin-up, the same features as described by Greatbatch and Lu can be observed, such as the formation of a swift eastward jet along the equator, that splits up into two branches as a Kelvin wave is emitted by the eastern boundary that arrests the flow at the equator (not shown).

- 3. An animation of the adjustment process may be found at <https://vimeo.com/145881146>.

$$\begin{aligned} L_x &= 4000 \text{ km} \\ L_y &= 2000 \text{ km} \\ g &= 0.01 \text{ m s}^{-2} \\ \beta &= 2 \times 10^{-11} \text{ s}^{-1} \text{ m}^{-1} \\ H &= 400 \text{ m} \\ A_h &= 10^4 \text{ m}^2 \text{ s}^{-1} \\ Y &= -75 \text{ km} \end{aligned}$$

Table B.1: Parameters used in the first verification run. Definitions as in Killworth, 1991.

- 4. The Arakawa grids were first introduced by Arakawa and Lamb, (1977), and are still widely used in geophysical fluid dynamics due to their computational efficiency and conservation properties.

- 5. Kawase (and thus Greatbatch and Lu) uses full spherical coordinates, and the h -equation has been linearized. See also § 4.2.1.

- 6. Otherwise, deeply penetrating cross-equatorial flow becomes impossible.

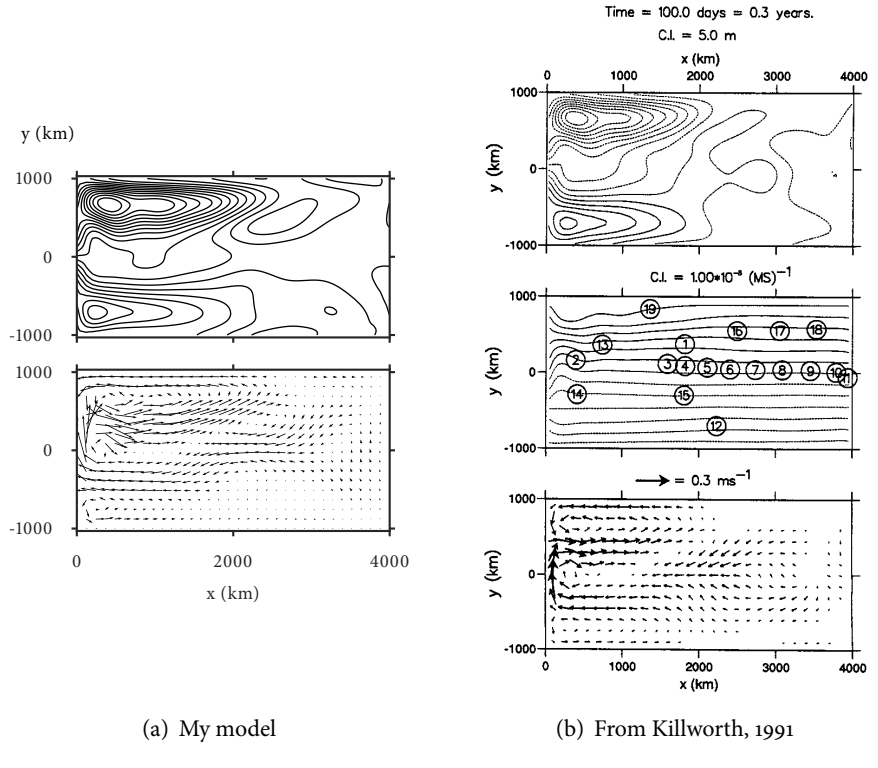


Figure B.1: Comparison between a geostrophic adjustment solution from Killworth, 1991, and one created with my own shallow-water model (identical parameters, as in Table B.1).

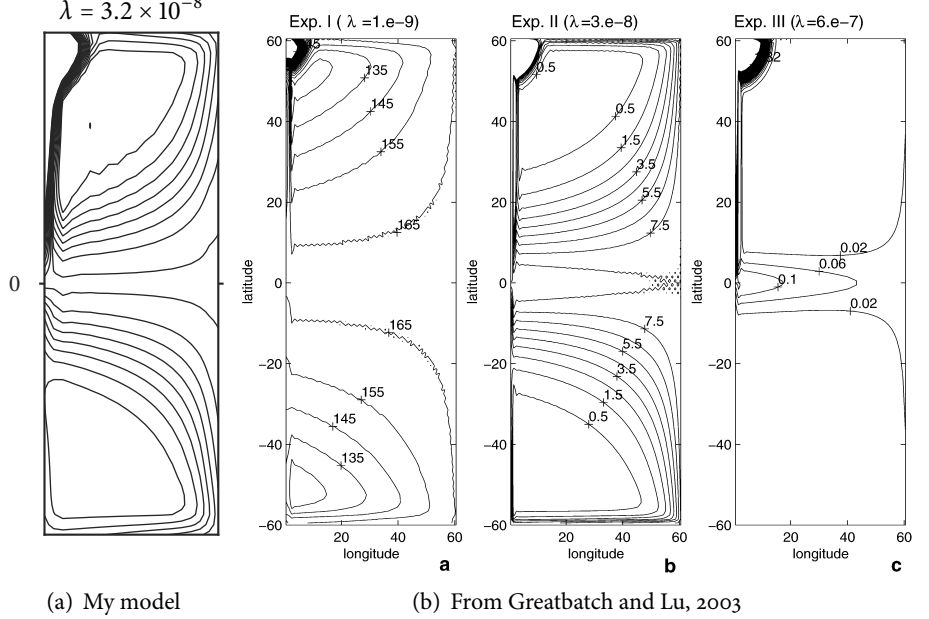


Figure B.2: Comparison between a steady-state solution from Greatbatch and Lu, 2003, and one created with my own shallow-water model.

BIBLIOGRAPHY

- Aken, Hendrik M. van, Irsan S. Brodjonegoro, and Indra Jaya (2009). “The deep-water motion through the Lifamatola Passage and its contribution to the Indonesian throughflow.” In: *Deep Sea Research Part I: Oceanographic Research Papers* 56.8, pp. 1203–1216. ISSN: 0967-0637. DOI: <http://dx.doi.org/10.1016/j.dsr.2009.02.001> (Cited on p. 57).
- Anderson, David LT and Dennis W Moore (1979). “Cross-equatorial inertial jets with special relevance to very remote forcing of the Somali Current.” In: *Deep Sea Research Part A. Oceanographic Research Papers* 26.1, pp. 1–22 (Cited on p. 62).
- Arakawa, Akio and Vivian R Lamb (1977). “Computational design of the basic dynamical processes of the UCLA general circulation model.” In: *Methods in computational physics* 17, pp. 173–265 (Cited on p. 85).
- Bhatia, H. et al. (2013). “The Helmholtz-Hodge Decomposition — A Survey.” In: *IEEE Transactions on Visualization and Computer Graphics* 19.8, pp. 1386–1404. ISSN: 1077-2626. DOI: [10.1109/TVCG.2012.316](https://doi.org/10.1109/TVCG.2012.316) (Cited on p. 13).
- Blandford, Robert R. (1971). “Boundary conditions in homogeneous ocean models.” In: *Deep Sea Research and Oceanographic Abstracts* 18.7, pp. 739–751. ISSN: 0011-7471. DOI: [http://dx.doi.org/10.1016/0011-7471\(71\)90088-X](http://dx.doi.org/10.1016/0011-7471(71)90088-X) (Cited on p. 21).
- Broecker, Wallace S et al. (1991). “The great ocean conveyor.” In: *Oceanography* 4.2, pp. 79–89 (Cited on p. 28).
- Bryan, Kirk (1963). “A numerical investigation of a nonlinear model of a wind-driven ocean.” In: *Journal of the Atmospheric Sciences* 20.6, pp. 594–606 (Cited on p. 62).
- Bryan, Kirk (1987). “Potential vorticity in models of the ocean circulation.” In: *Quarterly Journal of the Royal Meteorological Society* 113.477, pp. 713–734. ISSN: 1477-870X. DOI: [10.1002/qj.49711347703](https://doi.org/10.1002/qj.49711347703) (Cited on p. 18).
- Bryan, Kirk, Syukuro Manabe, and Ronald C Pacanowski (1975). “A global ocean-atmosphere climate model. Part II. The oceanic circulation.” In: *Journal of Physical Oceanography* 5.1, pp. 30–46 (Cited on p. 44).
- Chorin, Alexandre Joel (1968). “Numerical solution of the Navier-Stokes equations.” In: *Mathematics of computation* 22.104, pp. 745–762 (Cited on p. 25).
- Courant, Richard, Kurt Friedrichs, and Hans Lewy (1928). “Über die partiellen Differenzengleichungen der mathematischen Physik.” In: *Mathematische Annalen* 100.1, pp. 32–74 (Cited on p. 26).

- Danabasoglu, Gokhan et al. (2012). "The CCSM4 ocean component." In: *Journal of Climate* 25.5, pp. 1361–1389 (Cited on p. 34).
- Edwards, C.A. and J. Pedlosky (1998). "Dynamics of nonlinear cross-equatorial flow. Part I: potential vorticity transformation." In: *J.Phys.Oceanogr.* 28, pp. 2382–2406 (Cited on pp. 2, 65).
- Godfrey, J. S., J. Wilkin, and A. C. Hirst (1993). "Why Does the Indonesian Throughflow Appear to Originate from the North Pacific?" In: *Journal of Physical Oceanography* 23.6, pp. 1087–1098. DOI: 10.1175 / 1520 - 0485(1993)023<1087:WDTITA>2.0.CO;2 (Cited on pp. 30, 58, 78).
- Godfrey, JS (1989). "A Sverdrup model of the depth-integrated flow for the world ocean allowing for island circulations." In: *Geophysical & Astrophysical Fluid Dynamics* 45.1-2, pp. 89–112 (Cited on pp. 41, 58, 59).
- Gordon, Arnold L. (1986). "Interocean exchange of thermocline water." In: *Journal of Geophysical Research: Oceans* 91.C4, pp. 5037–5046. ISSN: 2156-2202. DOI: 10.1029/JC091iC04p05037 (Cited on pp. 57, 78).
- Greatbatch, R. J. et al. (2012). "On the Width of the Equatorial Deep Jets." In: *Journal of Physical Oceanography* 42.10, pp. 1729–1740. DOI: 10.1175/JPO-D-11-0238.1 (Cited on pp. 50, 76).
- Greatbatch, Richard J and Jian Lu (2003). "Reconciling the Stommel box model with the Stommel-Arons model: A possible role for Southern Hemisphere wind forcing?" In: *Journal of Physical Oceanography* 33.8, pp. 1618–1632 (Cited on pp. 67, 68, 82, 85, 86).
- Guyer, Jonathan E, Daniel Wheeler, and James A Warren (2009). "FiPy: partial differential equations with python." In: *Computing in Science & Engineering* 11.3, pp. 6–15 (Cited on p. 82).
- Jochum, M. et al. (2008). "Ocean viscosity and climate." In: *J. Geophys. Res.* 113, C06017, doi:10.1029/2007JC004515 (Cited on pp. 3, 27, 35, 37, 44).
- Jochum, Markus et al. (2009). "Differences in the Indonesian seaway in a coupled climate model and their relevance to Pliocene climate and El Nino." In: *Paleoceanography* 24.1 (Cited on pp. 30, 53, 58, 59).
- Joseph, Daniel D (2006). "Potential flow of viscous fluids: Historical notes." In: *International Journal of Multiphase Flow* 32.3, pp. 285–310 (Cited on p. 6).
- Kämpf, Jochen (2009). *Ocean Modelling for Beginners*. Springer (Cited on p. 82).
- Kawase, Mitsuhiro (1987). "Establishment of deep ocean circulation driven by deep-water production." In: *Journal of Physical Oceanography* 17.12, pp. 2294–2317 (Cited on pp. 2, 24, 65, 66, 85).
- Killworth, O. (1991). "Cross-equatorial geostrophic adjustment." In: *J.Phys.Oceanogr.* 21, pp. 1581–1601 (Cited on pp. 2, 3, 21, 48, 61, 63–67, 82, 85, 86).

- Kitamura, Yuji and Keiichi Ishioka (2007). "Equatorial Jets in Decaying Shallow-Water Turbulence on a Rotating Sphere." In: *Journal of the Atmospheric Sciences* 64.9, pp. 3340–3353. DOI: 10.1175/JAS4015.1 (Cited on p. 78).
- Kuhlbrodt, T. et al. (2007). "On the driving processes of the Atlantic meridional overturning circulation." In: *Reviews of Geophysics* 45.2. RG2001. ISSN: 1944-9208. DOI: 10.1029/2004RG000166 (Cited on pp. 2, 28, 29).
- Large, William G et al. (2001). "Equatorial circulation of a global ocean climate model with anisotropic horizontal viscosity." In: *Journal of Physical Oceanography* 31.2, pp. 518–536 (Cited on p. 35).
- Large, William George and Stephen G Yeager (2004). *Diurnal to decadal global forcing for ocean and sea-ice models: the data sets and flux climatologies*. National Center for Atmospheric Research Boulder (Cited on p. 35).
- Levitus, S et al. (1998). "World Ocean Database 1998, vol. 1, Introduction, NOAA Atlas NESDIS 18." In: *NOAA, Silver Spring, Md* (Cited on p. 34).
- Liu, Zhiqiang and Jianping Gan (2012). "Variability of the Kuroshio in the East China Sea derived from satellite altimetry data." In: *Deep Sea Research Part I: Oceanographic Research Papers* 59, pp. 25 –36. ISSN: 0967-0637. DOI: <http://dx.doi.org/10.1016/j.dsr.2011.10.008> (Cited on p. 19).
- Lukas, Roger, Toshio Yamagata, and Julian P McCreary (1996). "Pacific low-latitude western boundary currents and the Indonesian throughflow." In: *Journal of Geophysical Research: Oceans* 101.C5, pp. 12209–12216 (Cited on pp. 57, 78).
- Madec, Gurvan and Maurice Imbard (1996). "A global ocean mesh to overcome the North Pole singularity." In: *Climate Dynamics* 12.6, pp. 381–388. ISSN: 1432-0894. DOI: 10.1007/BF00211684 (Cited on p. 33).
- Marshall, John and Kevin Speer (2012). "Closure of the meridional overturning circulation through Southern Ocean upwelling." In: *Nature Geoscience* 5.3, pp. 171–180 (Cited on pp. 2, 28).
- Meehl, Gerald A. et al. (2012). "Monsoon Regimes and Processes in CCSM4. Part I: The Asian–Australian Monsoon." In: *Journal of Climate* 25.8, pp. 2583–2608. DOI: 10.1175/JCLI-D-11-00184.1 (Cited on p. 57).
- Munk, Walter H. (1950). "On the Wind-Driven Ocean Circulation." In: *Journal of Meteorology* 7.2, pp. 80–93. DOI: 10.1175/1520-0469(1950)007<0080:OTWDOC>2.0.CO;2 (Cited on pp. 19, 20, 24).
- Nof, Doron (1990). "Why are some boundary currents blocked by the equator?" In: *Deep Sea Research Part A. Oceanographic Research Papers* 37.5, pp. 853–873 (Cited on p. 77).
- Nof, Doron (1996). "What controls the origin of the Indonesian throughflow?" In: *Journal of Geophysical Research: Oceans* 101.C5, pp. 12301–12314 (Cited on p. 78).

- Nof, Doron and Donald B. Olson (1993). "How do western abyssal currents cross the equator?" In: *Deep Sea Research Part I: Oceanographic Research Papers* 40.2, pp. 235–255. ISSN: 0967-0637. DOI: [http://dx.doi.org/10.1016/0967-0637\(93\)90002-K](http://dx.doi.org/10.1016/0967-0637(93)90002-K) (Cited on pp. 62, 63, 77).
- Pedlosky, J. (1992). *Geophysical Fluid Dynamics*. Springer study edition. Springer New York. ISBN: 9780387963877 (Cited on pp. 5, 10, 12, 22–24).
- Pedlosky, J. (1996). *Ocean Circulation Theory*. 1st ed. Springer-Verlag Berlin Heidelberg. Chap. 2, 3. 456 pp. ISBN: 978-3-540-60489-1. DOI: 10.1007/978-3-662-03204-6 (Cited on pp. 2, 5, 18, 20, 21, 59, 71, 72).
- Pedlosky, Joseph (2013). *Waves in the Ocean and Atmosphere*. Springer Science & Business Media (Cited on p. 8).
- Rahmstorf, Stefan (2002). "Ocean circulation and climate during the past 120,000 years." In: *Nature* 419.6903, pp. 207–214 (Cited on p. 28).
- Shields, Christine A. et al. (2012). "The Low-Resolution CCSM4." In: *Journal of Climate* 25.12, pp. 3993–4014. DOI: 10.1175/JCLI-D-11-00260.1 (Cited on p. 34).
- Smith, R et al. (2010). "The parallel ocean program (POP) reference manual." In: *Los Alamos National Lab Technical Report* 141 (Cited on pp. 26, 35).
- Smith, RD, S Kortas, and B Meltz (1995). "Curvilinear coordinates for global ocean models." In: *Los Alamos preprint LA-UR-95-1146* (Cited on p. 33).
- Smith, Richard D. and Peter R. Gent (2004). "Anisotropic Gent–McWilliams Parameterization for Ocean Models." In: *Journal of Physical Oceanography* 34.11, pp. 2541–2564. DOI: 10.1175/JPO2613.1 (Cited on p. 35).
- Sprintall, Janet et al. (2009). "Direct estimates of the Indonesian Throughflow entering the Indian Ocean: 2004–2006." In: *Journal of Geophysical Research: Oceans* 114.C7. ISSN: 2156-2202. DOI: 10.1029/2008JC005257 (Cited on pp. 30, 57).
- Steele, Michael, Rebecca Morley, and Wendy Ermold (2001). "PHC: A global ocean hydrography with a high-quality Arctic Ocean." In: *Journal of Climate* 14.9, pp. 2079–2087 (Cited on p. 34).
- Stommel, Henry (1948). "The westward intensification of wind-driven ocean currents." In: *Eos, Transactions American Geophysical Union* 29.2, pp. 202–206. ISSN: 2324-9250. DOI: 10.1029/TR029i002p00202 (Cited on p. 24).
- Stommel, Henry (1961). "Thermohaline convection with two stable regimes of flow." In: *Tellus* 13.2, pp. 224–230 (Cited on p. 2).
- Stommel, Henry and AB Arons (1960). "On the abyssal circulation of the world ocean—I. Stationary planetary flow patterns on a sphere." In: *Deep Sea Research* (1953) 6, pp. 140–154 (Cited on p. 2).
- Sverdrup, Harald Ulrich (1947). "Wind-driven currents in a baroclinic ocean; with application to the equatorial currents of the eastern Pacific." In: *Pro-*

ceedings of the National Academy of Sciences 33.11, pp. 318–326 (Cited on p. 18).

Swaters, G.E. (2015). “Midlatitude–Equatorial Dynamics of a Grounded Deep Western Boundary Current. Part I: Midlatitude Flow and the Transition to the Equatorial Region.” In: *J.Phys.Oceanogr.* 45, pp. 2457–2469 (Cited on p. 77).

Vallis, Geoffrey K (2006). *Atmospheric and Oceanic Fluid Dynamics*. Cambridge University Press (Cited on p. 8).

Wajsowicz, Roxana C. (1993a). “A Simple Model of the Indonesian Throughflow and Its Composition.” In: *Journal of Physical Oceanography* 23.12, pp. 2683–2703. DOI: 10.1175/1520-0485(1993)023<2683:ASMOTI>2.0.CO;2 (Cited on p. 54).

Wajsowicz, Roxana C. (1993b). “The Circulation of the Depth-integrated Flow around an Island with Application to the Indonesian Throughflow.” In: *Journal of Physical Oceanography* 23.7, pp. 1470–1484. DOI: 10.1175/1520-0485(1993)023<1470:TCOTDI>2.0.CO;2 (Cited on pp. 41, 57, 59, 77).

Wesseling, Pieter (2009). *Principles of Computational Fluid Dynamics*. Vol. 29. Springer Science & Business Media (Cited on pp. 25, 26).

Wüst, G. (1935). “Schichtung und Zirkulation des Atlantischen Ozeans: Die Stratosphäre.” In: *Wissenschaftliche Ergebnisse der Deutschen Atlantischen Expedition auf dem Forschungs- und Vermessungsschiff “Meteor” 1925–1927* 6, p. 288 (Cited on p. 28).

COLOPHON

This document was typeset using the custom L^AT_EX 2_E document class `dionsthesis`, based on `uiothesis` developed by Eivind Uggedal. It uses Minion Pro, developed at Adobe Systems, and Fira Sans, developed by the Mozilla Foundation, as body fonts. `dionsthesis` is available at:

<https://github.com/dionhaefner/dionsthesis/>

The style of `uiothesis` was inspired by Robert Bringhurst's seminal book on typography *The Elements of Typographic Style*. Typographic, structural and graphical decisions in this document follow the ideas presented in Jean-Luc Doumont's book *Trees, Maps, and Theorems*.

DECLARATION

I declare that this thesis is my own personal effort. I have not already obtained a degree on the basis of this work. Furthermore, I took reasonable care to ensure that the work is original, and, to the best of my knowledge, does not breach copyright law, and has not been taken from other sources except where such work has been cited and acknowledged within the text.

Heidelberg, December 16, 2016

Dion Häfner